Quantum Dots in Gated Nanowires and Nanotubes

A dissertation presented

by

Hugh Olen Hill Churchill

to

The Department of Physics

in partial fulfillment of the requirements

for the degree of

Doctor of Philosophy

in the subject of

Physics

Harvard University

Cambridge, Massachusetts

May 2012

©2012 - Hugh Olen Hill Churchill

All rights reserved.

Thesis advisor: Author:

Charles M. Marcus Hugh O. H. Churchill

Quantum Dots in Gated Nanowires and Nanotubes

Abstract

This thesis describes experiments on quantum dots made by locally gating one-dimensional quantum wires. The first experiment studies a double quantum dot device formed in a Ge/Si core/shell nanowire. In addition to measuring transport through the double dot, we detect changes in the charge occupancy of the double dot by capacitively coupling it to a third quantum dot on a separate nanowire using a floating gate. We demonstrate tunable tunnel coupling of the double dot and quantify the strength of the tunneling using the charge sensor.

The second set of experiments concerns carbon nanotube double quantum dots. In the first nanotube experiment, spin-dependent transport through the double dot is compared in two sets of devices. The first set is made with carbon containing the natural abundance of ^{12}C (99%) and ^{13}C (1%), the second set with the 99% ^{13}C and 1% ^{12}C. In the devices with predominantly ^{13}C, we find evidence in spin-dependent transport of the interaction between the electron spins and the ^{13}C nuclear spins that was much stronger than expected and not present in the ^{12}C devices.

In the second nanotube experiment, pulsed gate experiments are used to measure the timescales of spin relaxation and dephasing in a two-electron double quantum dot. The relaxation time is longest at zero magnetic field and goes through a minimum at higher field, consistent with the spin-orbit-modified electronic spectrum of carbon nanotubes. We

measure a short dephasing time consistent with the anomalously strong electron-nuclear interaction inferred from the first nanotube experiment.

Contents

Title Page i
Abstract iii
Table of Contents v
List of Figures viii
List of Tables x
Acknowledgments xi
Dedication xii

1 Introduction 1

2 Carbon Nanotube Quantum Dots 5
2.1 Electronic structure 5
2.1.1 Bandgap 5
2.1.2 Longitudinal confinement, valley degeneracy, and large orbital moments 9
2.1.3 Spin-orbit, valley, and hyperfine couplings 11
2.2 Quantum dots 19
2.2.1 Fabrication of top-gated devices 19
2.2.2 Electron-electron interactions 21
2.2.3 Few-electron double quantum dots 21

3 A Ge/Si heterostructure nanowire-based double quantum dot with integrated charge sensor 27
3.1 Introduction 28
3.2 Fabrication of devices and demonstration of tunable interdot coupling . . . 30
3.3 Charge sensing 33
3.4 Charging sensing of interdot transitions and measurement of tunnel coupling 34
3.5 Conclusion 36
3.6 Methods 37
3.6.1 Fabrication of Ge/Si NW Devices 37
3.6.2 Measurements 37
3.7 Supplementary Figures 38

4 Electron-nuclear interaction in ^{13}C nanotube double quantum dots 41
4.1 Introduction . . . 42
4.2 Device fabrication and quantum dot formation . . . 43
4.3 Spin blockade and charge sensing . . . 45
4.4 Comparison of ^{12}C and ^{13}C spin blockade . . . 47
4.5 Signatures of hyperfine coupling in ^{13}C nanotubes . . . 49
4.6 Conclusions . . . 52
4.7 Methods . . . 52
4.8 Epilogue . . . 53
4.9 Supplementary Discussion . . . 55

5 Relaxation and dephasing in a two-electron carbon nanotube double quantum dot 57
5.1 Introduction . . . 58
5.2 Device fabrication and demonstration of few-electron double dot . . . 59
5.3 Pauli blockade with spin and isospin . . . 60
5.4 Relaxation of blocked states . . . 62
5.5 Magnetic field dependence of relaxation . . . 63
5.6 Dephasing . . . 66
5.7 Summary . . . 68
5.8 Epilogue . . . 69

6 Conclusions and Outlook 71

A Top-gated carbon nanotube double dot devices 74
A.1 First-generation top-gated devices . . . 75
A.1.1 Wafer selection . . . 75
A.1.2 Prepare blank substrates and write alignment marks . . . 76
A.1.3 Catalyst Pads . . . 77
A.1.4 Nanotube Growth . . . 78
A.1.5 Locate nanotubes with SEM . . . 80
A.1.6 Contacting nanotubes . . . 81
A.1.7 Room temperature characterization . . . 82
A.1.8 ALD gate insulator . . . 82
A.1.9 Top-gates . . . 86
A.2 Devices designed to reduce long-range disorder . . . 87
A.2.1 Smaller devices . . . 88
A.2.2 ALD-covered devices . . . 91
A.2.3 Wet-etch suspended devices . . . 94
A.2.4 Suspended as-grown, ALD insulator coated, top-gated devices . . . 99
A.2.5 ALD upgrade . . . 109

B Bottom-gated, as-grown carbon nanotube single and double quantum dot devices 112
B.1 Single dot devices 113
B.2 Double dot devices 117

C Manipulation and readout circuit elements 126
C.1 Bias tee evolution 127
C.2 Printed circuit board designs 130
C.3 Superconducting spiral inductors 133
C.4 Lumped element kinetic inductance resonators 136
C.5 Miscellany 138
C.5.1 A quantitative benchmark for 60 Hz noise 138
C.5.2 Homemade low-noise cryogenic amplifiers 139
C.5.3 Sapphire coax heat sinks 140
C.5.4 Look-up table DAC calibration 142

D Superconducting spirals for dispersive readout of quantum dots 145
D.1 Introduction 145
D.2 Spiral and quantum dot fabrication 146
D.3 Spiral characterization 148
D.4 Dispersive shift due to quantum dot charging 150
D.5 Effect of resonator capacitance on readout sensitivity 152
D.6 Effect of resonator–dot coupling on readout sensitivity 154
D.7 Measurement of phase and amplitude response 155
D.8 Dispersive readout of spin blockade 159

Bibliography 161

List of Figures

1.1 Periodic table of nuclear spins . . . 2

2.1 Forming a carbon nanotube from graphene . . . 6
2.2 Orbital level structure of carbon nanotubes . . . 7
2.3 Three types of nanotubes: large, small, and negligible band gap . . . 8
2.4 Shell structure of a carbon nanotube quantum dot . . . 10
2.5 Effects of spin-orbit coupling, valley coupling, and misaligned field on one-electron nanotube states . . . 15
2.6 Fabrication steps for a top-gated nanotube double dot device . . . 20
2.7 Effects of spin-orbit coupling, valley coupling, and misaligned field on two-electron nanotube states . . . 24
2.8 States of (1,1) and of a tunnel-coupled two-electron nanotube double dot . 26

3.1 Ge/Si nanowire double dot device and demonstration of tunable interdot coupling . . . 29
3.2 Simultaneous transport and charge sensing measurements of a Ge/Si double dot . . . 30
3.3 Charge sensing of an isolated Ge/Si double dot . . . 32
3.4 Interdot tunneling between two Ge/Si dots measured with charge sensor . . 35
3.5 Extraction of Ge/Si single dot parameters . . . 39
3.6 Characterization of Ge/Si sensor dot and illustration of charge sensing . . . 40

4.1 Nanotube double dot with integrated charge sensor . . . 44
4.2 Spin blockade in a ^{13}C nanotube double dot . . . 46
4.3 Contrasting magnetic field dependence of leakage current for ^{12}C and ^{13}C devices . . . 48
4.4 Hysteresis and fluctuations in leakage current . . . 51

5.1 Few-electron ^{13}C nanotube double quantum dot . . . 60
5.2 Pulsed-gate measurements of Pauli blockade and spin relaxation . . . 61
5.3 Magnetic field dependence of spin relaxation . . . 64
5.4 Pulsed-gate measurement of dephasing . . . 67

A.1 Smaller nanotube double quantum dot device 89
A.2 Comparison of gates patterned with PMMA and ZEP 90
A.3 Data illustrating extra quantum dot due to disorder 91
A.4 ALD-protected device 93
A.5 Wet-etched, suspended device 95
A.6 Rotating/tilting sample stage for electron beam evaporation 97
A.7 n-type contacts to nanotubes with scandium 98
A.8 Isolated-ring device scheme 102
A.9 Effect of ALD Al_2O_3 on room temperature backgate sweeps 104
A.10 Uniform coverage of nanotubes by low-temperature ALD process 105
A.11 Dashed-ring device scheme 105
A.12 Dashed-ring device zoom-in 107
A.13 CVD-*in*compatible metal stacks 108
A.14 Four-valve upgrade for Marcus Lab ALD system 110

B.1 Suspended, as-grown carbon nanotube single quantum dot 114
B.2 Transport data for suspended single dot 116
B.3 Suspended, as-grown carbon nanotube double quantum dot 118
B.4 Optical image of suspended nanotube double dot 121
B.5 Chlorobenzene for photolithography lift-off undercut 122
B.6 Current through as-grown double quantum dots 124

C.1 Bias tee evolution 128
C.2 Comparison of transmission through a 5 kΩ resistor and a 250 nH inductor 129
C.3 Printed circuit boards for reflectometry and pulsed-gate experiments 131
C.4 On-chip lumped element kinetic inductance resonator 137
C.5 Cryogenic amplifier (Weinreb copy) 140
C.6 Sapphire heat sink for coax 141
C.7 Look-up table calibrations for DACs 143

D.1 PCB layout for dispersive readout with superconducting spirals 147
D.2 Dispersive readout circuit schematic 149
D.3 Example of dispersive frequency shift due to dot charging 151
D.4 Comparison of superconducting (small C) and normal (large C) resonators 153
D.5 Comparison of resonator response to a lead versus a gate 154
D.6 Schematic of phase and amplitude measurement circuit 156
D.7 Phase and amplitude measurements of double quantum dot charging 158
D.8 Amplitude readout of spin blockade 160

List of Tables

2.1 Spin-valley multiplets in a nanotube double quantum dot 23

A.1 Original nanotube furnace bakeout recipe. 79
A.2 Nanotube growth recipe. 79
A.3 NO_2 and precursor clearing recipe 84
A.4 NO_2 functionalization recipe 85
A.5 Low-temperature alumina capping layer recipe 85

Acknowledgments

Thank you Amir, Charlie, and Emmanuel! Others forthcoming.

dedicated to my family

Chapter 1

Introduction

As the canonical two-level system, a spin-1/2 particle is a natural candidate for a quantum bit. Because they are generally quite weakly coupled to the environment, spins make relatively long-lived qubits. For this reason ensembles of nuclear spins were among the first realizations of the ideas of quantum information science [1, 2]. The ability to confine and manipulate single electrons in semiconductor quantum dots enabled access to individual spins, now with electrons rather than nuclei [3, 4]. Electronic systems provided a number of advantages including single-spin control and the prospect of coupling together many qubits. The importance of nuclear spins did not diminish, but remained a focus for electron spin qubits in the form of the nuclei at each lattice site of the host material (GaAs in the case of the most advanced spin qubits). In this context, the nuclear spins were an incoherent bath that dominated the relaxation and coherence of electron spin qubits in many circumstances [5, 6]. This finding motivated the work in this thesis.

Because all naturally-occurring isotopes of the elements in groups III and V of the periodic table have non-zero nuclear spin (see Fig. 1.1), the problem is unavoidable in III-V materials. One must look to group IV or II-VI materials to find candidates for

	B 100 ^{10}3, ^{11}3/2	^{12}**C** 1.1 ^{13}1/2	**N** 100 ^{14}1, ^{15}1/2	^{16,18}**O** 0.04 ^{17}5/2
	Al 100 ^{27}5/2	^{28,30}**Si** 4.5 ^{29}1/2	**P** 100 ^{31}1/2	^{32,34,36}**S** 0.8 ^{33}3/2
^{64,66,68,70}**Zn** 4.1 ^{67}5/2	**Ga** 100 ^{69,70}3/2	^{70,72,74,76}**Ge** 7.7 ^{73}9/2	**As** 100 ^{75}3/2	^{74,76,78,80,82}**Se** 7.6 ^{77}1/2
^{106,110,112,114,116}**Cd** 25 ^{111,113}1/2	**In** 100 ^{113,115}9/2	^{116,118,120,122,124}**Sn** 17 ^{115,117,119}1/2	**Sb** 100 ^{121}5/2,^{123}7/2	^{122,124,126,128,130}**Te** 7.9 ^{123,125}1/2
^{196,198,200,202,204}**Hg** 30 ^{199}1/2,^{201}3/2	**Tl** 100 ^{203,205}1/2	^{204,206,208}**Pb** 22 ^{207}1/2	**Bi** 100 ^{209}9/2	

Figure 1.1: Periodic table showing most* stable isotopes of the group II through group VI elements. In each cell, the zero nuclear spin isotopes are listed in the top row, the middle row shows the percentage of non-zero nuclear spin isotopes, the spins of which are listed in the bottom row. The elements considered in this thesis—carbon, silicon, and germanium—are highlighted in green. Data from Ref. [7].

electron spin qubits free from nuclear spin, ignoring oxygen and sulfur which present difficulties for application in solid-state electronics. Most promising are the lightest group-IV elements carbon, silicon, and germanium which have, respectively, 1%, 5%, and 8% natural abundances of non-zero nuclear spin isotopes. Furthermore, by controlling the isotopic composition of the materials during synthesis, as demonstrated in Ch. 4 of this thesis and for a number of other materials [8, 9, 10, 11, 12], the presence of non-zero spin isotopes

* ^{108}Cd, ^{112}Sn, ^{114}Sn, and ^{120}Te are omitted for clarity, all of which have zero spin and abundances less than 1%.

can in principle be made arbitrarily small. In this regard a heavy, enriched II-VI material such as $^{202}Hg^{114}Cd^{130}Te$ would also be appealing for spin qubit applications by combining a nuclear-free system with the strong spin-orbit coupling characteristic of heavy elements that is useful for manipulation [13]. The same may also hold true for holes in isotopically enriched Ge/Si nanowires due to an exceptionally strong predicted spin-orbit coupling [14]. On the other hand, nuclear spins may also be tamed to provide a unique resource, for example as a quantum memory [15, 16, 17, 18] or in the generation of local magnetic field gradients [19].

An enormous effort in many groups has been directed at the development of spin qubits using carbon, silicon, and germanium. The field has become so large in fact that the following references can only be representative. Implementations with carbon include double quantum dots in carbon nanotubes [20, 21, 22, 23, 24, 25, 26, 27] and single-layer [28, 29, 30] and bi-layer graphene [31], and hybrid electron-nuclear systems in endohedral fullerenes [32, 33] and diamond NV centers [34, 35]. The landscape for silicon and germanium includes Si/SiGe two-dimensional electron gases [36], P donors in Si [37], Si MOSFET double dots [38, 39, 40, 41], Ge/Si core/shell nanowires [42], undoped Si/SiGe heterostructures [43], and defect centers in SiC [44]. Over the past few years, the promise of extended qubit coherence in group IV materials has been shown to hold true, particularly in the cases of defect centers in diamond and SiC as well as quantum dots in undoped SiGe.

The experiments described in this thesis concern double quantum dots formed in one-dimensional wires (nanowires) of silicon-germanium and carbon. To make a quantum dot, electrons must be confined in all three dimensions, so the advantage of starting with a one-dimensional material is that two dimensions of confinement come for free. The result is simpler device designs (fewer gates per dot) and generally larger energy scales (charging energy and, more importantly, level spacing). Another advantage of these nanowires is

simpler growth (chemical vapor deposition instead of molecular beam epitaxy, typically) which made possible the isotope control described in Ch. 4. The disadvantages of one-dimensional materials are random locations after growth and more restricted possibilities for coupling dots, though this is not a fundamental obstacle [45, 46, 47]

Following this introduction is a more detailed description of carbon nanotube quantum dots in Ch. 2. No such introduction to Ge/Si nanowires is provided because the particular material properties of Ge/Si are not required to understand the work in Ch. 3 other than the facts that the carriers are holes and that double dots had not previously been demonstrated in that material. After the introduction to carbon nanotubes, this thesis may be divided into three parts, which describe different aspects of the effort to create a spin qubit using one-dimensional wires:

- Chapter 3 describes transport and charge sensing measurements of a Ge/Si core/shell nanowire double quantum dot, which demonstrated the potential of that material system for spin qubit applications.
- Chapters 4 and 5 describessimilar work on carbon nanotube double quantum dots made with either 99% ^{12}C or 99% ^{13}C, including spin-dependent and few-electron measurements.
- Appendices A, B, C, and D describe techniques of fabrication and high-frequency measurement developed for these experiments that may be of interest to others working in this field.

Chapter 2

Carbon Nanotube Quantum Dots

This chapter describes some of the characteristics of quantum dots formed in carbon nanotubes with an emphasis on details relevant to the experiments described in Chapters 4 and 5.[1]

2.1 Electronic structure

2.1.1 Bandgap

Tight-binding models conclude that depending on chirality, nanotubes may be broadly categorized in two types: either semiconducting, with a band gap inversely proportional to diameter ($E_{\mathrm{gap}} \sim 0.7$ eV·nm/d), or metallic, with a linear dispersion, $E = \hbar v_F k$, where d is the diameter of the nanotube, $v_F \sim 8 \times 10^5$ m/s is the Fermi velocity [49] and k is the wave vector [50, 51, 52]. This result is illustrated in Fig. 2.1. The electronic structure of nanotubes may be understood in terms of the linear dispersion of graphene near the K and K' points in momentum space (Dirac cones), constrained by the quantization

[1] Some of the ideas and figures are adapted from Ref. [48].

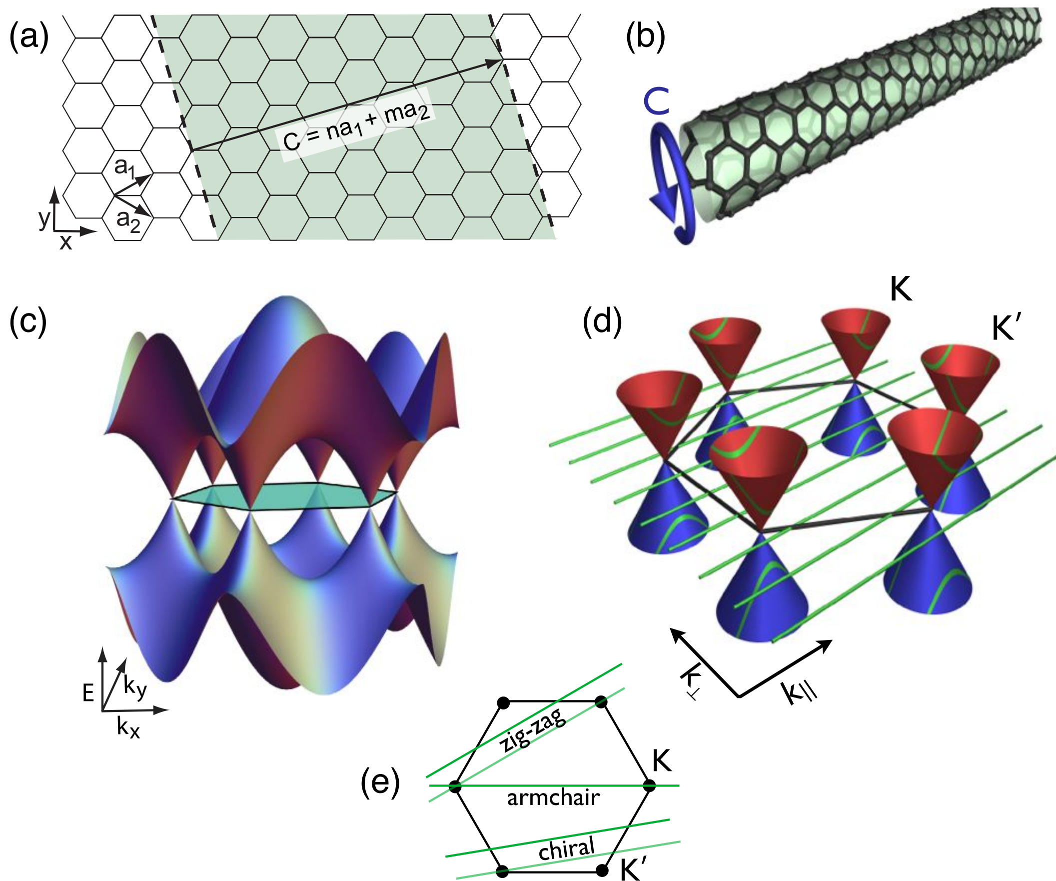

Figure 2.1: (a) and (b) A carbon nanotube is formed by rolling up a sheet of graphene such that the chiral vector C forms the circumference of the nanotube. In this case the chiral indices (n, m) are (6,2). (c) and (d) The low-energy band structure of a nanotube is formed by taking the π-bands of graphene and quantizing the momentum along the circumferential direction, $k_\perp$. Hyperbolic bands are formed where the lines of allowed $k_\perp$ intersect the Dirac cones. (e) Depending on the chiral vector, the resulting hyperbolic bands either intersect the K points, which creates a metallic nanotube, or do not, which creates a semiconducting nanotube.

condition of fitting an integer number of Fermi wavelengths around the circumference of the nanotube [Fig. 2.1(d)]. When the closest quantization line (green) misses the K point, a band gap appears along with hyperbolic electron-like and hole-like dispersions near the K point. When the quantization line goes through the K point, the nanotube is metallic.

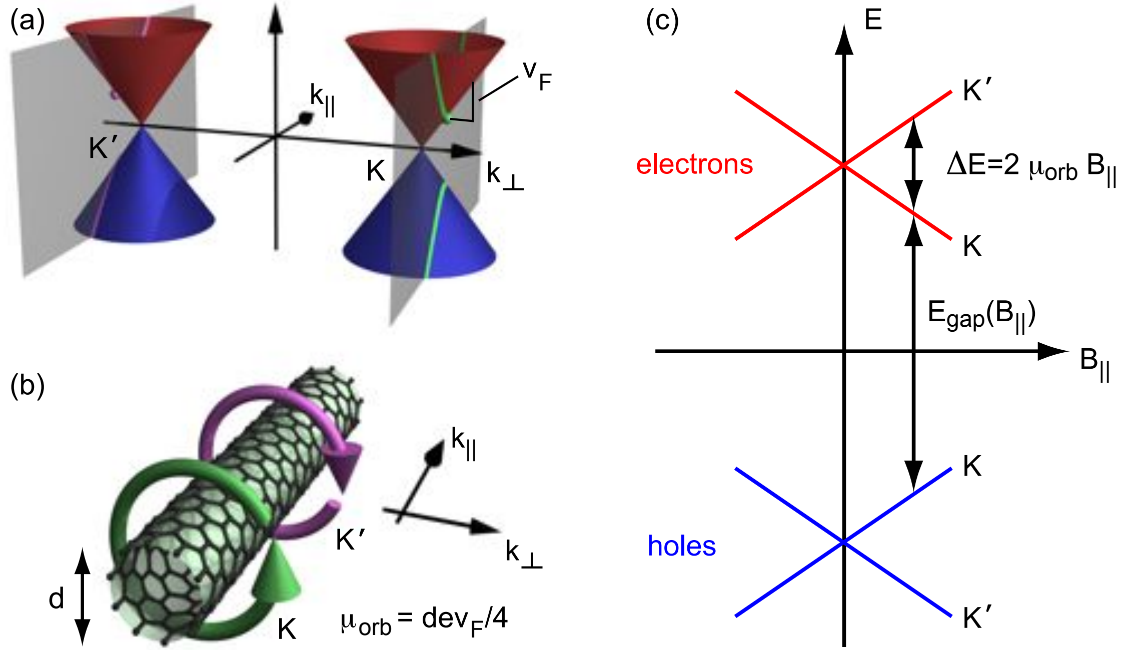

Figure 2.2: (a) The quantization condition on $k_\perp$ (gray planes) results in four hyperbolic bands (green and purple curves, two each for electrons and holes) near the two Dirac points (K,K') of graphene. (b) The lowest electron-like states in the K and K' valleys are equal in energy (green and purple dots in panel (a), and constitute a clockwise and counterclockwise ring current around the nanotube circumference. (c) The resulting large orbital magnetic moments ($\mu_{\rm orb} = dev_F/4$ near the bandgap) can be employed to lift the valley degeneracy and tune the band gap $E_{\rm gap}$ with an external magnetic field $B_{||}$. These energy level shifts can be visualized in panel (a) as shifting the gray planes to the left for increasing $B_{||}$.

At this stage of the development, the energy bands have the form

$$E = \pm\hbar v_F \sqrt{k_{||}^2 + k_\perp^2}, \tag{2.1}$$
$$k_\perp = E_{\rm gap}/2\hbar v_F.$$

Experiments have found that a third type commonly occurs: nominally metallic nanotubes have small band gaps [53, 54, 55] of tens of meV, most likely due to curvature [56], strain [57, 58], and electron-electron interactions [59].[2] Representative conductance

[2]We have measured current as a function of back-gate voltage for $\sim$ 1000 different nanotubes and very few ($<$ 1%) appear to be truly metallic with a flat gate response at room temperature. They cannot be confirmed metallic without further study at low temperature because the position in gate voltage of the

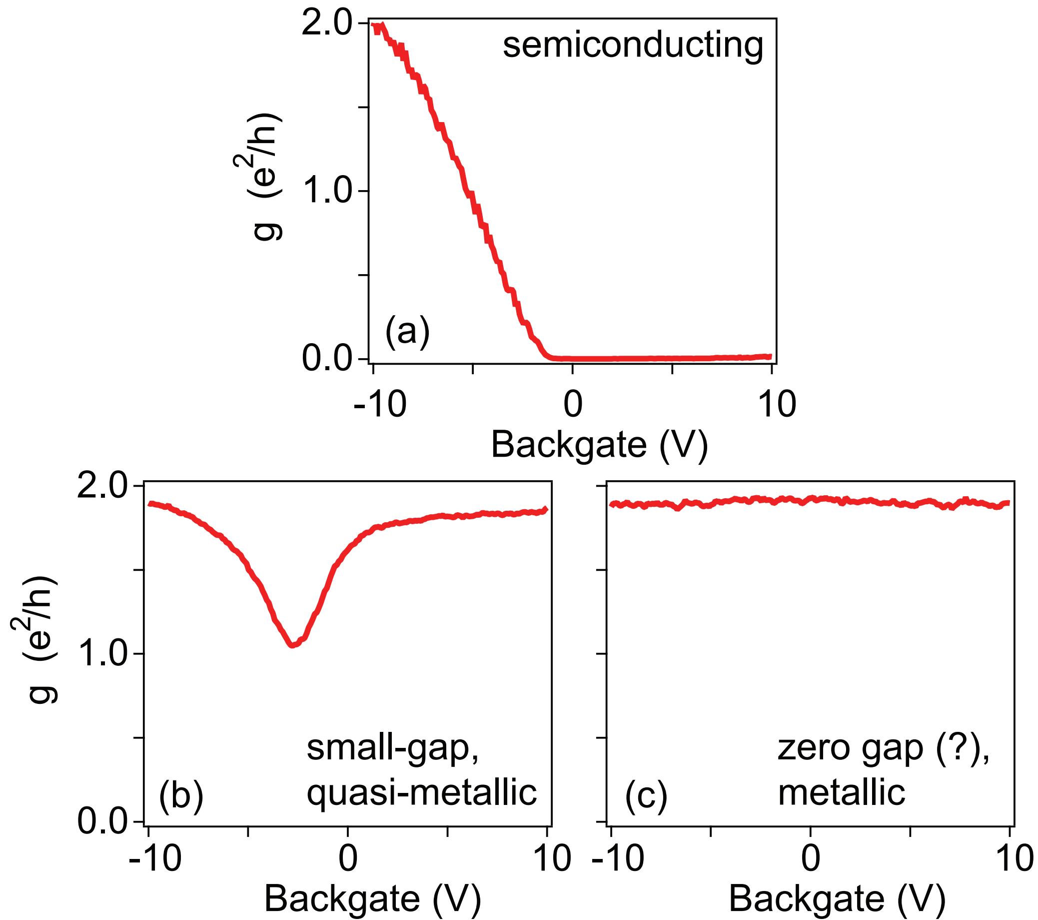

Figure 2.3: Conductance as a function of back-gate (doped Si with 500 nm thermal oxide) voltage for three Pd contacted nanotubes: (a) semiconducting (b) small band gap or quasi-metallic and (c) metallic, presumably.[4] The fact that all the maximum conductances are approximately $2e^2/h$ reflects the size of the library of conductance traces from which these were selected rather than a special property of our nanotubes or the Pd contact metal.

versus backgate traces measured at room temperature for these three types of nanotubes are shown in Fig. 2.3. When contacted by Pd which has a large work function and a favorable interaction with nanotubes,[3] semiconducting nanotubes have large p-type conductance

---

middle of the gap could in principle be outside the range measured due to doping, though in practice the doping of freshly contacted nanotubes is sufficiently consistent (for small and large gap nanotubes) that this is unlikely. Another possibility is that the nanotube measured is inside a bundle that screens the backgate.

[3]Unlike Pt, which has a higher work function but must be used in a high temperature process to achieve good contact, as occurs for as-grown devices (see Appendix B).

[Fig. 2.3(a)] and very small n-type conductance [60]. Nanotubes with a small band gap comparable to kT at room temperature show strong ambipolar conductance with only a dip in conductance in the middle of the gap [Fig. 2.3(b)], and nanotubes with no conductance variation with gate voltage are assumed to be metallic [Fig. 2.3(c)].

Small band gap nanotubes (with correspondingly small effective mass) are ideal for many quantum dot experiments in which tunnel couplings depend on both the barrier potential and the effective mass. Light mass also mitigates the effects of disorder, which is present in all devices. Both of these considerations conveniently allow gate patterns for quantum dot devices to have larger dimensions. However, since the barrier potential itself cannot exceed the band gap due to Klein tunneling [27], the band gap should be sufficiently large to prevent unwanted barrier transparency.

2.1.2 Longitudinal confinement, valley degeneracy, and large orbital moments

In quantizing the Dirac cones of graphene, [Fig. 2.2(a)], hyperbolic electron-like and hole-like dispersions appear near the K point, and time-reversal symmetry guarantees a second set of energy bands with exactly the same energy at the K' point. Quantum dots may be formed in a nanotube by introducing a confining potential in the longitudinal (down-the-long-axis) direction. The confinement adds an additional constraint to eq. 2.1 that restricts the longitudinal momentum to quantized values $k_{||} = n\pi/L,\ n \geq 1$. These longitudinal orbital levels (illustrated in Fig. 2.4) produce the shell structure that is observed in many experiments on carbon nanotube quantum dots [61, 62, 63, 64, 25]. In this simplest model of hard-wall confinement, the shells are spaced (evenly, because of the linear dispersion)

by $hv_F/2L \approx 1.7$ meV$\cdot\mu$m$/L$ [65].[4] Experimentally, this spacing is usually found to be reasonably accurate based on the expected length of the quantum dot [66].

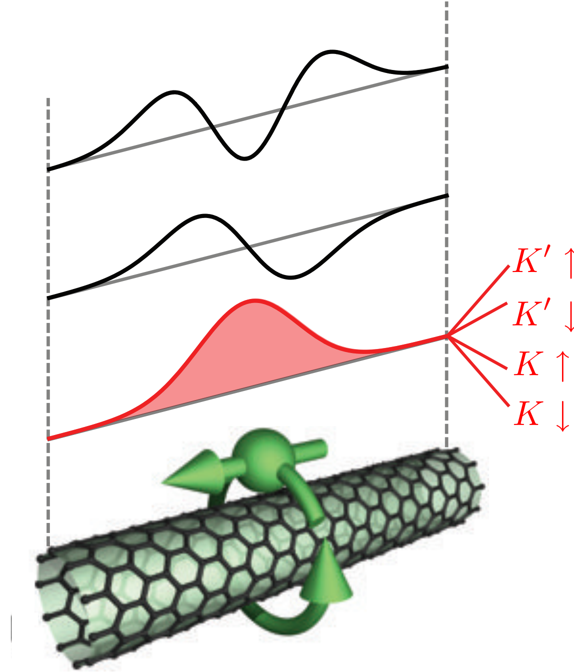

Figure 2.4: Confining electrons in a nanotube along its length creates a quantum dot with a series of longitudinal levels or shells, each of which can accommodate four electrons, corresponding to combinations of the spin and valley quantum numbers. In the simplest model, the levels are spaced by $hv_F/2L \approx 1.7$ meV$\cdot\mu$m$/L$.

For a confining potential that is smooth on the atomic scale[5], discrete quantum states can be formed from either the K or K' valleys, yielding a two-fold degenerate energy spectrum (ignoring spin for the moment). The valley degeneracy constitutes a discrete, two-state quantum degree of freedom (called isospin) that is insensitive to long-wavelength electrical noise and so is potentially useful as a long-lived qubit. It is not, however, expected to be immune to hyperfine-induced relaxation [67] (see §2.1.3). Isospin, combined with

[4] This estimate is a factor of two larger than in Ref. [65] and a factor of four larger than other references which attempt to calculate an average level spacing taking into account nondegeneracies in spin and/or isospin, rather than the intrinsic longitudinal level spacing.

[5] One that is rough on the atomic scale will couple the valleys and break the degeneracy.

spin, gives a four-fold degeneracy in the electronic spectrum. One consequence of this picture is that stationary states formed from one valley [green dot in Fig. 2.2(a)] carry a persistent current around the nanotube circumference, while the opposite valley (purple dot) carries the opposite current. Magnetic moments associated with these clockwise and counterclockwise currents are quite large, equivalent to several Bohr magnetons for typical nanotube diameters ($\mu_{\rm orb} = dev_F/4 \approx 3.4\mu_{\rm B} \cdot d/{\rm nm}$). This expression is an approximation appropriate only near the band gap; at higher occupancy, much of the electron's constant v_F is expended in $k_{||}$ at the expense of $k_\perp$, an effect that reduces the orbital moment as more electrons fill the quantum dot [68]. Because valleys couple strongly to magnetic fields applied parallel to the nanotube axis [69] [Fig. 2.2(b)], external fields can be used to tune both the band gap and the energy separation of opposite valley states [Fig. 2.2(c)]. These energy level shifts with a parallel magnetic field, $B_{||}$, may be understood as a modification of the quantization condition on $k_\perp$ by the Aharonov-Bohm flux, $\Phi_{\rm AB} = B\pi r^2$, produced by the field so that eq. 2.1 becomes (also including the Zeeman effect due to $B_{||}$)

$$\begin{aligned} E &= \pm\hbar v_F\sqrt{k_{||}^2 + k_\perp^2} - g\mu_B S_{||}B_{||}, \\ k_\perp &= E_{\rm gap}/2\hbar v_F + \frac{1}{r}\frac{\Phi_{\rm AB}}{\Phi_0}, \\ k_{||} &= n\pi/L,\ n \geq 1, \end{aligned} \tag{2.2}$$

where g is the electron spin g-factor ≈ 2, $S_{||} = \pm 1/2$ is the projection of the spin along the nanotube axis, r is the nanotube radius, and Φ_0 is the magnetic flux quantum [70].

2.1.3 Spin-orbit, valley, and hyperfine couplings

Spin-orbit coupling

As described above, in the absence of disorder, electron-electron interactions, and spin-orbit coupling, the ground state of a one-electron nanotube quantum dot is four-fold

degenerate, reflecting both spin ($\uparrow$ / $\downarrow$) and valley (K/K') degeneracies (Fig. 2.4). This situation is illustrated in Fig. 2.5(a) which shows the evolution of the four states $K\downarrow$, $K\uparrow$, $K'\downarrow$, and $K'\uparrow$ as a function of magnetic field parallel and perpendicular to the nanotube axis calculated from eq. 2.1. That these degeneracies were broken in some cases had been observed for some time [66] and modeled as a sub-band mismatch[6] [71], but the situation was clarified immensely when Kuemmeth, Ilani, *et al.* observed clear evidence of spin-orbit coupling in very clean carbon nanotube quantum dots [70]. In an as-grown device with extremely low disorder (short- and long-range), they found that not all four states become degenerate at $B = 0$. Instead, the electron states with parallel orbital- and spin-magnetic moments ($K\downarrow$ and $K'\uparrow$) appear slightly lower in energy than the states with anti-parallel alignment ($K\uparrow$ and $K'\downarrow$), while the opposite is observed for a one-hole quantum dot. The four-fold degenerate manifold of states was split as a consequence of spin-orbit coupling into two Kramers doublets opposite in both spin and isospin quantum numbers.

The spectrum in the presence of spin-orbit coupling is shown in Fig. 2.5(b), the right side of which (parallel field) is similar to that observed in Ref. [70]. Spin-orbit coupling in carbon nanotubes was first predicted by Ando in 2000 [72] and rapidly became a popular topic of theoretical study [73, 74, 75, 76, 77, 78, 79, 80, 81, 82, 83]. In addition to its fundamental interest, spin-orbit coupling in carbon nanotubes may allow electrical manipulation of spins [84] in addition to optical control of quantum information [85, 86, 87]. A detailed and clear theoretical description of the spin-orbit-modified spectrum of carbon nanotubes is provided in §II of Ref. [88]. Another excellent summary is provided in the supplement to Ref. [89].

Spin-orbit coupling in nanotubes may be understood in terms of the intra-atomic

[6]This subband mismatch can most likely now be reinterpreted as a combination of spin-orbit and valley coupling.

spin-orbit coupling Δ intrinsic to carbon atoms, which couples p_z orbitals of one spin with p_x orbitals of the opposite spin,[7] combined with the curved graphene sheet of the nanotube surface [74]. In flat graphene, the first non-zero term of intrinsic spin-orbit coupling is second order in Δ by symmetry: once an electron has hopped, for example, from $p_z \downarrow$ to $p_x \uparrow$ (order Δ), it must hop to $p_x \uparrow$ on the next site, then from $p_x \uparrow$ to $p_z \downarrow$ on that site (order Δ again). The crucial point for carbon nanotube spin-orbit coupling is that nanotubes are *curved* graphene sheets, which in a tight-binding model turns on a hopping term between a p_x orbital at one site with a p_z orbital on the next site. The reason is that on a curved surface, the p_z orbital of the nearest neighbor is tilted with respect to the initial site, so that the nearest neighbor p_z looks like a linear combination of p_z and p_x (assuming $\hat{y}$ is the axial direction). Now the sequence for spin-orbit mediated hopping is simply $p_z \downarrow$ to $p_x \uparrow$ (order Δ), then $p_x \uparrow$ directly to $p_z \uparrow$ on the next site. The result is a spin-dependent coupling between adjacent atoms.

As the electron completes a closed trajectory around the circumference of the nanotube, spin-orbit coupling produces a change in the momentum $k_\perp$ in the circumferential direction, the sign of which depends on the relative orientation of the spin and the direction of the trajectory (clockwise or counter-clockwise, K or K'). In this way, spin-orbit coupling in nanotubes arises from a geometric phase, equivalent to an Aharonov-Bohm flux applied parallel to the nanotube [72]. This interpretation motivates a modification of eq. 2.2 for the energy levels of a nanotube quantum dot to reflect the quantization condition for $k_\perp$ in the presence of spin-orbit coupling:

[7] Recall that the $\mathbf{L} \cdot \mathbf{s}$ that appears in an atomic spin-orbit Hamiltonian may be recast as $(L_+ s_- + L_- s_+)/2 + L_z s_z$.

$$\begin{aligned} E &= \pm\hbar v_F\sqrt{k_{||}^2+k_\perp^2}-g\mu_B S_{||}B_{||}, \\ k_\perp &= E_{\text{gap}}/2\hbar v_F+\frac{1}{r}\frac{\Phi_{\text{AB}}}{\Phi_0}+S_{||}\frac{2}{r}\frac{\Phi_{\text{SO}}}{\Phi_0}, \\ k_{||} &= n\pi/L,\ n\geq 1. \end{aligned} \tag{2.3}$$

In addition to the spin-orbit coupling produced by the geometric phase, Δ_1, an additional term, Δ_0, was subsequently identified [77, 82, 83] that is also created by the curvature of the graphene sheet and can be understood as an effective valley-dependent Zeeman term [89]. For the same reason that the orbital magnetic moment depends on occupancy, so does the term Δ_1, as measured by Jespersen, Grove-Rasmussen, *et al.* in Ref. [89]. The combination of these two terms explains the electron-hole anisotropy of spin-orbit coupling strength observed in experiment [70] because the total spin-orbit coupling for electrons and holes is $\Delta^e_{SO}=2(\Delta_0-\Delta_1)$ and $\Delta^h_{SO}=-2(\Delta_0+\Delta_1)$, assuming the sign conventions in Ref. [88]. Another consequence of the term Δ_0 is that like many electronic properties of nanotubes, Δ_0 is proportional to the chiral angle θ determined by the formation of the nanotube from a graphene sheet (cf. Fig. 2.1). Therefore the spin-orbit coupling strength in carbon nanotubes follows chiral family patterns and varies much more widely than would be expected on the basis of changes in radius alone [77]. Curiously, despite the four possibilities for the signs and relative magnitudes of Δ_0 and Δ_1, only one combination ($|\Delta_1|>|\Delta_0|$, $\Delta_1<0$, $\Delta_0>0$) has been observed in the three nanotubes for which data are available [70, 89].

Valley coupling

Another interaction that was isolated for the first time in Ref. [70] is the coupling between states with the same spin orientation but different valleys, $\Delta_{KK'}$. Though its

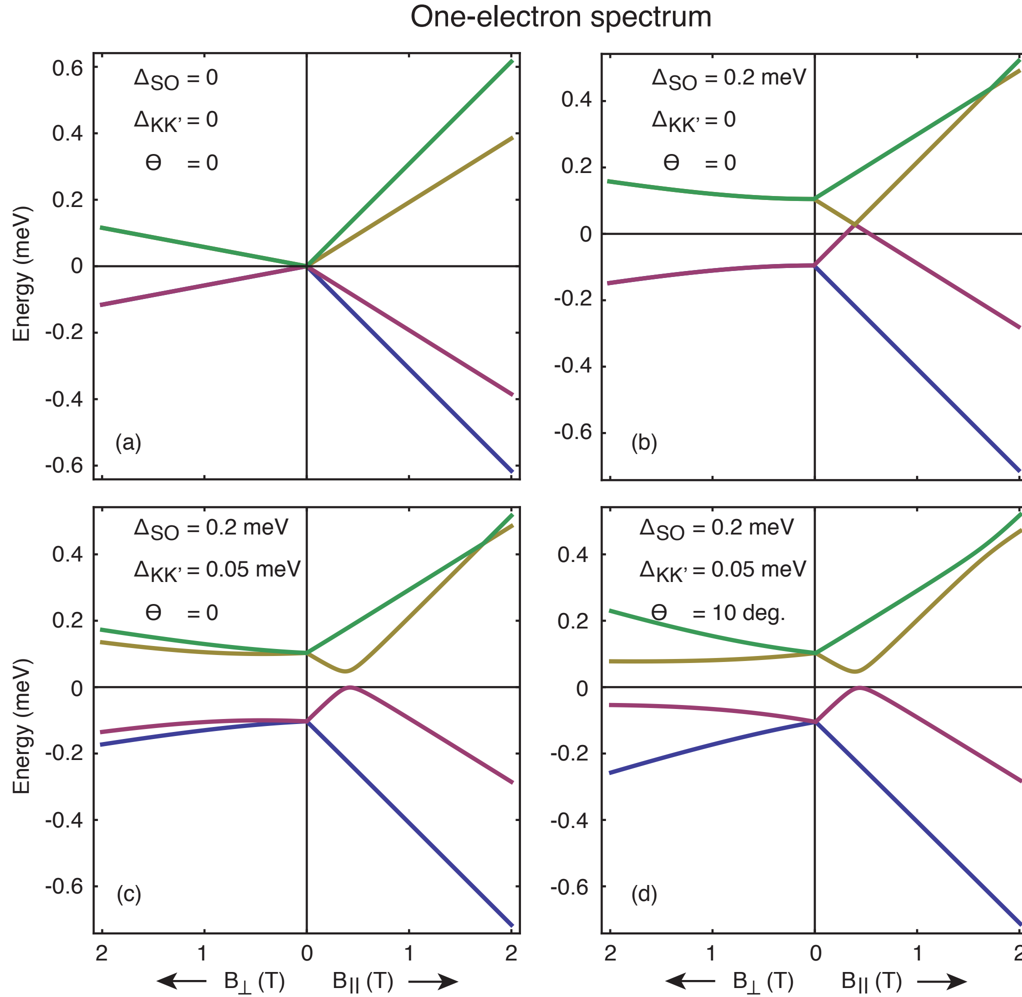

Figure 2.5: Spectrum of levels as a function of perpendicular (left side in each) and parallel (right side) magnetic field for one electron in a nanotube quantum dot including Zeeman (μ_B=0.058 meV/T) and orbital shifts, spin-orbit coupling (Δ_{SO}), valley coupling ($\Delta_{KK'}$), and magnetic field misaligned from the nanotube axis by an angle θ. The effects are added together from (a) to (d) for typical experimental parameters. The bottom-right is the most realistic experimental case in which $\Delta_{SO} = 0.2$ meV, $\Delta_{KK'} = 0.05$ meV and $\theta = 10$ degrees. At 2 T in all cases shown, the states are $K\downarrow$ (blue), $K\uparrow$ (red), $K'\downarrow$ (brown), and $K'\uparrow$ (green). The orbital moment (μ_{orb}=0.25 meV/T) was chosen to be on the smaller side to accentuate the different slopes for states with spin up and spin down.

microscopic origin is not well-studied experimentally, certainly not in transport measurements, this valley coupling arises from short-range impurities such as adatoms, substitutional atoms, or structural defects, the only requirement being for the potential to have a

component that varies on the length-scale of the lattice spacing, since momentum equal to the K point must be transferred to change valleys ($|K - K'| = |K|$) [90, 84, 91]. Intervalley scattering due to defects is a common feature in Raman spectra of graphene and carbon nanotubes, appearing as the D- and G'-bands [92]. Valley coupling plays a crucial role in efforts to create a spin qubit in carbon nanotubes, because some degree of valley mixing is required to drive spin transitions at low frequencies [93, 91]. In the presence of valley coupling, an anti-crossing proportional to $\Delta_{KK'}$ opens up in the spectrum for a nanotube shell, as shown in Fig. 2.5(c).

Simulating spin-orbit and valley coupled spectra

Because the size of orbital magnetic moments, spin-orbit coupling, and valley coupling can vary widely from nanotube to nanotube, it is convenient for an experimentalist to be able to quickly simulate spectra and tune parameters to characterize a particular nanotube with one electron (either the first above the gap or the first above a full shell; see Appendix B for an example). For the four spin and valley states for one electron in a nanotube, this can be done by plotting the eigenvalues of the Hamiltonian

$$H_{1e} = \begin{pmatrix} \Delta_{SO}/2+(\mu_{\mathrm{orb}}-\mu_B)B\cos\theta & 0 & \mu_B B\sin\theta & \Delta_{KK'} \\ 0 & \Delta_{SO}/2+(-\mu_{\mathrm{orb}}+\mu_B)B\cos\theta & \Delta_{KK'} & \mu_B B\sin\theta \\ \mu_B B\sin\theta & \Delta_{KK'} & -\Delta_{SO}/2+(\mu_{\mathrm{orb}}+\mu_B)B\cos\theta & 0 \\ \Delta_{KK'} & \mu_B B\sin\theta & 0 & -\Delta_{SO}/2+(-\mu_{\mathrm{orb}}-\mu_B)B\cos\theta \end{pmatrix}, \tag{2.4}$$

where the parameters are as described above except for the field misalignment angle, θ ($\theta = 0$ corresponds to perfect $B_{||}$) and the g-factor is assumed to be $g = 2$. This is done for example in Fig. 2.5 to illustrate the effect on the spectrum of Δ_{SO}, $\Delta_{KK'}$, and field misalignment as a function of $B_{||}$ (at an angle θ) and $B_{\perp}$ (at an angle $\theta + \pi/2$) using Mathematica code written by Ferdinand Kuemmeth and Menyoung Lee. Each of these effects have been described above except field misalignment, which, in addition to providing orbital shifts due

to misaligned $B_\perp$, also opens up an anti-crossing of states formed from the same valley with opposite spins at high field. For $\Delta_{KK'} = 0$, the splitting induced by misalignment by an angle θ is $\Delta_\theta = g\mu_B\sqrt{(B\cos\theta + \Delta_{SO}/g\mu_B)^2 + (B\sin\theta)^2}$, which figures prominently in the spin relaxation rate at that location as described in Ch. 5 [94, 84, 95]. This details of the spin-orbit-modified spectrum for carbon nanotubes was considered experimentally in great detail in Ref. [89].

Hyperfine coupling

Composed of light atoms with electrons occupying p-orbitals (mostly), the interaction between electron and nuclear spins (hyperfine coupling) in carbon nanotubes is expected to be weak. This expectation is confirmed by theoretical calculations in stark contrast with the experimental findings suggested by Ch. 4 [96], the interpretation of which remains confounding even a few years after their observation.

Prior to our work on ^{13}C nanotube quantum dots, no experimental or direct theoretical estimates of the hyperfine coupling strength in carbon nanotubes existed. Instead we were guided by calculations for similar systems such as fullerenes [97] and small graphene flakes [98] which estimated a value of the hyperfine coupling constant $A \sim 1$ μeV. Since then theoretical studies focused precisely on hyperfine interactions in carbon nanotube quantum dots have been carried out [99, 67]. In GaAs quantum dots, the contact hyperfine interaction dominates because the electrons occupy s-orbitals with significant weight at the location of the nucleus. Consistent with the expectation stated above, Fischer *et al.* find that the contact term is negligible in all but the smallest diameter nanotubes which have significant s-p hybridization due to curvature. In the larger (few-nanometer) diameter nanotubes that most commonly used in experiments, the dipolar hyperfine interaction is dominant. The dipolar term is highly ansisotropic and even changes sign among the hyperfine components

in the circumferential, radial, and longitudinal directions. The magnitude of the hyperfine interaction in nanotubes was found to be a large fraction of a μeV, similar to the values for graphene and fullerenes because the curvature associated with diameters as small as 1 nm does not produce much s-p hybridization [99].

Because the hyperfine interaction acts locally at each lattice site, one interesting consequence of hyperfine coupling in carbon nanotubes is that it can mediate transitions between states that differ in both spin *and* valley [67]. Pályi and Burkard estimate in Ref. [67] that the valley-conserving and valley-mixing components of the hyperfine interaction are similar in magnitude. One expected manifestation of this effect that has not been experimentally verified is that splitting spin or valley states separately (by applying a perfectly perpendicular magnetic field to the nanotube, for example) is insufficient to prevent hyperfine-mediated transitions; to do so requires splitting both simultaneously.

Fischer *et al.* point out a possible additional contribution to the hyperfine coupling in nanotubes that arises from the coupling to the angular momentum of the circumferential orbital motion of the electrons [99], and while they do not comment on its magnitude, the analysis of Latil *et al.* seems to indicate that the effect becomes very small when the orbiting electron is delocalized over the length of a typical quantum dot [100]. Another potential modification to the hyperfine coupling strength in nanotubes examined by Braunecker *et al.* originates from a phase in which the nuclear spins are locked into helical order [101, 102]. The ordered phase is predicted to be extremely fragile but is stabilized by a simultaneous ordered phase of electron density which is estimated to bring the critical temperature of the phase up to about 10 mK for a hyperfine coupling constant of 1 μeV. Given that this effect relies on electron correlations, the temperature scale likely would be reduced out of consideration in our dielectric-coated nanotubes without an otherwise significantly enhanced hyperfine coupling.

2.2 Quantum dots

2.2.1 Fabrication of top-gated devices

Device fabrication using electron-beam lithography and atomic layer deposition of gate oxides yields highly-tunable double quantum dots with integrated charge sensors. These devices allow independent control of charge states and tunnel barriers. This section describes fabrication of the carbon nanotube double quantum dots studied in Ch. 4 and 5, but the techniques are quite similar to those used for the Ge/Si core/shell nanowires that are the focus of Ch. 3.

Fabrication proceeded in the following way (see Appendix A for more details): Ti/Pt/Au alignment marks were patterned by electron-beam lithography and evaporation, followed by patterning of an array of 5 nm thick Fe catalyst pads on a small chip (~ 5 mm on a side) of degenerately doped thermally oxidized silicon. The chip was then loaded into a chemical vapor deposition furnace [Fig. 2.6(b)] that used either ^{12}C or ^{13}C methane feedstock. After identifying straight nanotube segments using a scanning electron microscope [Fig. 2.6(a)], devices were contacted with Pd patterned using electron beam lithography and metal lift-off. Devices were then coated with a 30 nm Al_2O_3 top-gate insulator using atomic layer deposition (ALD). To preserve the electronic properties of the nanotubes, a non-covalent functionalization layer using iterated exposure to NO_2 and trimethylaluminum [103] was applied before the Al_2O_3 ALD process. The high dielectric constant of Al_2O_3 enhanced the capacitive coupling of the nanotube to aluminum electrodes (top-gates) [Fig. 2.6(f)], and as described below in §2.2.2, the high dielectric constant presumably also suppressed long-range electron interactions which may otherwise have extinguished the level spacing required for spin read-out.

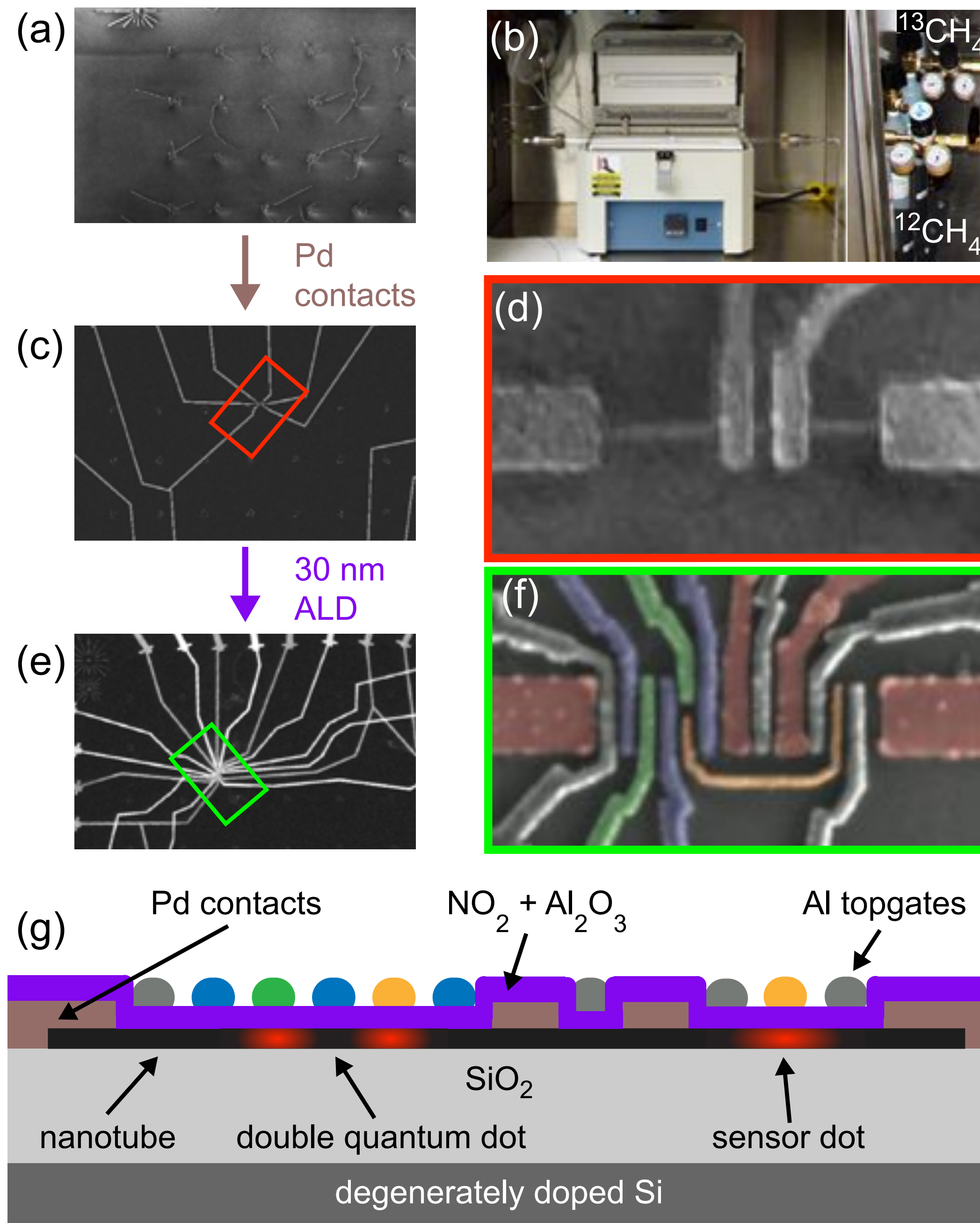

Figure 2.6: (a) Single-walled carbon nanotubes of controlled ^{12}C and ^{13}C composition were grown in a tabletop furnace from isotopically purified methane. (b) Individual nanotubes were located relative to alignment marks, contacted with Pd (c,d), and top-gated (e) after atomic layer deposition (ALD) of a thin Al_2O_3 or HfO_2 dielectric insulator. (f) The barrier gates (blue) and coupling wire (orange) allowed the formation of a double quantum dot with integrated charge sensor on the same nanotube. (g) Schematic cross-section of a finished device. Figure adapted from Ref. [48].

2.2.2 Electron-electron interactions

An important effect which we took advantage of (unknowingly at the time) was the screening of long-range electron-electron interactions by metal gates and the high-dielectric environment provided by the ALD gate insulator described above. The importance of interactions for the work in this thesis is that they reduce the energy separation of states in different longitudinal orbital levels. If the Coulomb interaction is too strong, the reduction in level spacing would be catastrophic because it is not practically possible to observe Pauli blockade and use it to read out spin states. The strength of the long-range Coulomb interaction is set by the effective fine-structure constant in carbon nanotubes, $e^2/\kappa\hbar v_F \approx 2.7/\kappa$, where κ is the dielectric constant of the environment surrounding the nanotube. It is generally assumed that the effects of Coulomb interactions are responsible for the ubiquity of Pauli blockade in our alumina-coated nanotube double dots, and its absence in long, uncoated devices [27].

Several theoretical studies of Coulomb interactions in carbon nanotube quantum dots have been carried out in recent years. Secchi and Rontani [79] and Wunsch [78] studied interactions in carbon nanotube dots with spin-orbit coupling with varying length and dielectric environment. Stecher *et al.* [104] and Weiss *et al.* [88] considered Coulomb interactions in nanotube double quantum dots, including the influence of interactions on Pauli blockade in those devices. The conclusion is that Coulomb repulsion profoundly modifies the spectrum of bare, suspended nanotubes, but the effects are suppressed by a factor of κ in coated nanotubes.

2.2.3 Few-electron double quantum dots

Ignoring the exchange interaction, the ground states for two (or more) electrons in a carbon nanotube single quantum dot are found by climbing up the one-electron excitation

spectrum [70, 89], and the excitation spectrum for a double dot is built from symmetric and antisymmetric combinations of those same one-electron states [104, 88]. For a doubly occupied single dot, the $(0,2)$ configuration of a double dot, there are six[8] anti-symmetric states that can be formed. For one electron in each dot, $(1,1)$, an additional 10 symmetric combinations are allowed for a total of 16 $(1,1)$ states[9]. This counting is the basis for the classification of blocked and unblocked states in Ch. 5 assuming conserved spin and valley within the double dot.

The spin-valley multiplets that result from this procedure are summarized in Table 2.1, where the compact notation of Stecher *et al.* has been adopted [104]. The states are grouped naturally into three multiplets, each separated by the spin-orbit splitting Δ which is a reflection of their construction from the single-electron Kramers doublets The same states appear in Weiss *et al.* in more explicit form [88]. For example, the symmetric spin-valley state $|K\uparrow, K\uparrow\rangle$ in Table 2.1 corresponds to the state $|\Phi_{13}^{11}\rangle = (|LK_{\uparrow}^{+}\uparrow\rangle_1 |RK_{\uparrow}^{+}\uparrow\rangle_2 - 1 \leftrightharpoons 2)/\sqrt{2}$ in Ref. [88]. The magnetic field dependence of these states is shown in Fig. 2.7 for the same parameters as Fig. 2.5.

We note that the structure of the lowest (0,2) states is similar to the spin and orbital states of the O_2 molecule which also has two electrons to distribute in two orbitals [105]. However, in O_2 all of the six basis states are written as either spin singlet or spin triplet states, which is accomplished by taking the sum and difference of states 5 and 6 in Table 2.1. In a spin-orbit dominated carbon nanotube, however, these two states have different energy, and hence remain maximally entangled states of spin and isospin. Therefore this $(0,2)/O_2$ correspondence only holds for nanotubes without spin-orbit coupling.

[8] This is $\binom{4}{2} = 6$ combinations because there are four one-electron states from which we select two different ones to satisfy the Pauli exclusion principle.

[9] In $(1,1)$ the number is increased to 4×4 because the same one-electron state may be selected twice; that is, spin- and valley-polarized states are allowed with anti-symmetry imposed in L/R space.

Table 2.1: Spin and valley (isospin) multiplets of two electrons occupying the lowest longitudinal shell of one $(0,2)$ or both $(1,1)$ dots of a double dot, ignoring valley coupling. In the limit of small interdot tunneling, $B = 0$ and zero exchange, states within each multiplet shown become degenerate. The states are grouped in columns according to their separation by the spin-orbit coupling Δ_{SO}. Adapted from Ref. [104], where $|\tau_1 s_1, \tau_2 s_2\rangle^{\pm} = (|\tau_1 s_1, \tau_2 s_2\rangle \pm |\tau_2 s_2, \tau_1 s_1\rangle)/\sqrt{2}$. The L/R indices have been suppressed for concision: for $(0,2)$ both electrons occupy the $|RK^{\tau}\rangle$ orbital, for $(1,1)$ the states that are anti-symmetric in spin-valley are symmetric in L/R while the symmetric spin-valley states are anti-symmetric in L/R. States of $(0,2)$ are numbered according to the convention in Weiss *et al.*: $n \to |\Phi_n^{02}\rangle$. Construction of the (1,1) states is more complicated to create the proper (anti-)symmetry in L/R space, but the anti-symmetric states labeled n below are used in the states $n+$ of Weiss *et al.*, and the symmetric states labeled $n(-)$ go with their states $n(-)$. See Ref. [88] for details.

$-\Delta_{SO}$	0	Δ_{SO}
	anti-symmetric states, $(0,2)$ and $(1,1)$	
$\|K\downarrow, K'\uparrow\rangle^-,\ 6$	$\|K\downarrow, K\uparrow\rangle^-,\ 3$	$\|K\uparrow, K'\downarrow\rangle^-,\ 5$
	$\|K\downarrow, K'\downarrow\rangle^-,\ 2$	
	$\|K\uparrow, K'\uparrow\rangle^-,\ 1$	
	$\|K'\uparrow, K'\downarrow\rangle^-,\ 4$	
	symmetric states, $(1,1)$ only	
$\|K\downarrow, K\downarrow\rangle,\ 14$	$\|K\downarrow, K\uparrow\rangle^+,\ 3-$	$\|K\uparrow, K\uparrow\rangle,\ 13$
$\|K\downarrow, K'\uparrow\rangle^+,\ 6-$	$\|K\downarrow, K'\downarrow\rangle^+,\ 2-$	$\|K\uparrow, K'\downarrow\rangle^+,\ 5-$
$\|K'\uparrow, K'\uparrow\rangle,\ 15$	$\|K\uparrow, K'\uparrow\rangle^+,\ 1-$	$\|K'\downarrow, K'\downarrow\rangle,\ 16$
	$\|K'\uparrow, K'\downarrow\rangle^+\ 4-$	

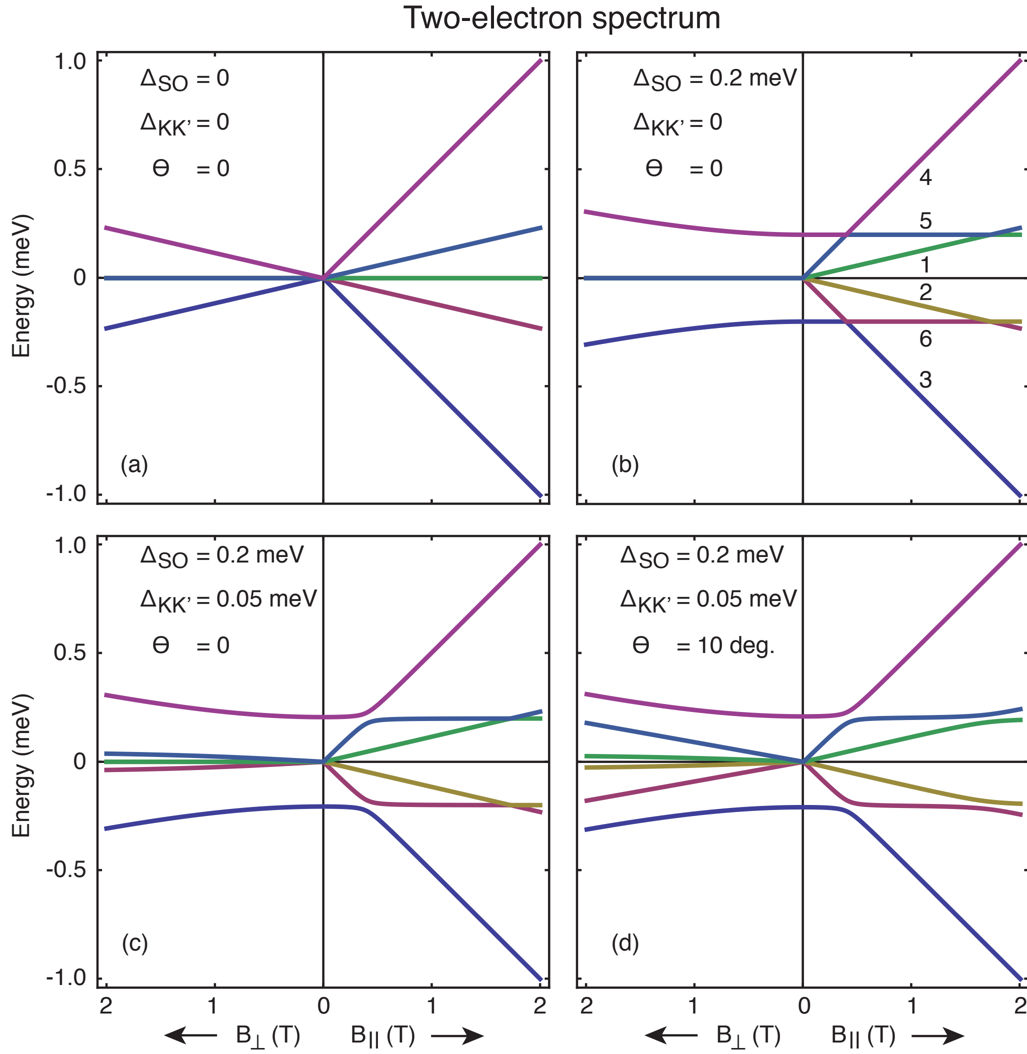

Figure 2.7: Spectrum of levels as a function of perpendicular (left side in each) and parallel (right side) magnetic field for two electrons in a nanotube quantum dot including Zeeman (μ_{B}=0.058 meV/T) and orbital (μ_{orb}=0.25 meV/T) shifts, spin-orbit coupling (Δ_{SO}), valley coupling ($\Delta_{KK'}$, and magnetic field misaligned from the nanotube axis by an angle θ. The effects are added together from (a) to (d) for typical experimental parameters. States are labeled in (b) to correspond to Ref. [88]. The bottom-right is the most realistic experimental case in which $\Delta_{\mathrm{SO}} = 0.2$ meV, $\Delta_{KK'} = 0.05$ meV and $\theta = 10$ degrees. At 2 T in all cases shown, the states are $K\downarrow$ (blue), $K\uparrow$ (red), $K'\downarrow$ (brown), and $K'\uparrow$ (green). The orbital moment was chosen to be on the smaller side to accentuate the different slopes for states with spin up and spin down.

A common procedure in double dot pulsed-gate experiments such as those in Ch. 5 is to initialize the system in $(0, 2)$, separate the electrons by pulsing to $(1, 1)$, and pulse back to $(0, 2)$, taking advantage of Pauli blockade to measure the final spin state of the two electrons. For this procedure to work, the two dots must be tunnel coupled, which provides a further modification to the electronic structure. With 16 states of $(1, 1)$, six of which are tunnel coupled to $(0, 2)$, a complete description would be too lengthy for this experimentalist's summary. Instead, the results of Ref. [88] are summarized in Fig. 2.8.

Fig. 2.8(a) shows the magnetic field dependence of the states of $(1, 1)$, including tunneling, spin-orbit coupling, and Coulomb interactions but neglecting valley coupling. The levels are grouped into three multiplets separated by the spin-orbit energy, with degeneracies of 4-8-4 (top to bottom) that are broken by a combination of tunneling and Coulomb interaction. A remarkable feature of Fig. 2.8(a) is that even for $\kappa = 10$, Coulomb interaction dominates tunneling deep in $(1, 1)$ so that the ground state of $(1, 1)$ is anti-symmetric in L/R space and therefore not tunnel-coupled to the ground state of $(0, 2)$. How these states are linked to those of $(0, 2)$ by the tunnel coupling is shown in Fig. 2.8(b) and (c) for zero and finite field ($B_{||} = 1$ T), respectively, as a function of the detuning ϵ that tilts the double dot potential to the right for increasing ϵ. At $B_{||} = 1$ T in Fig. 2.8(c), all degeneracies are broken, and the separation of 6 allowed $(0, 2)$ states from the 16 total states of $(1, 1)$ may be observed by counting the downward-moving $(0, 2)$ states and the upward-moving states that are stuck in $(1, 1)$ at large ϵ.

At various intersections of these states, they can be coupled by the hyperfine interaction and valley coupling [91]. This effect and its influence on the T_2^* pulsed-gate experiment or "return probability experiment" is the subject of two detailed papers by Reynoso and Flensberg with [106] and without [107] valley coupling, the findings of which are discussed at the end of Ch. 5.

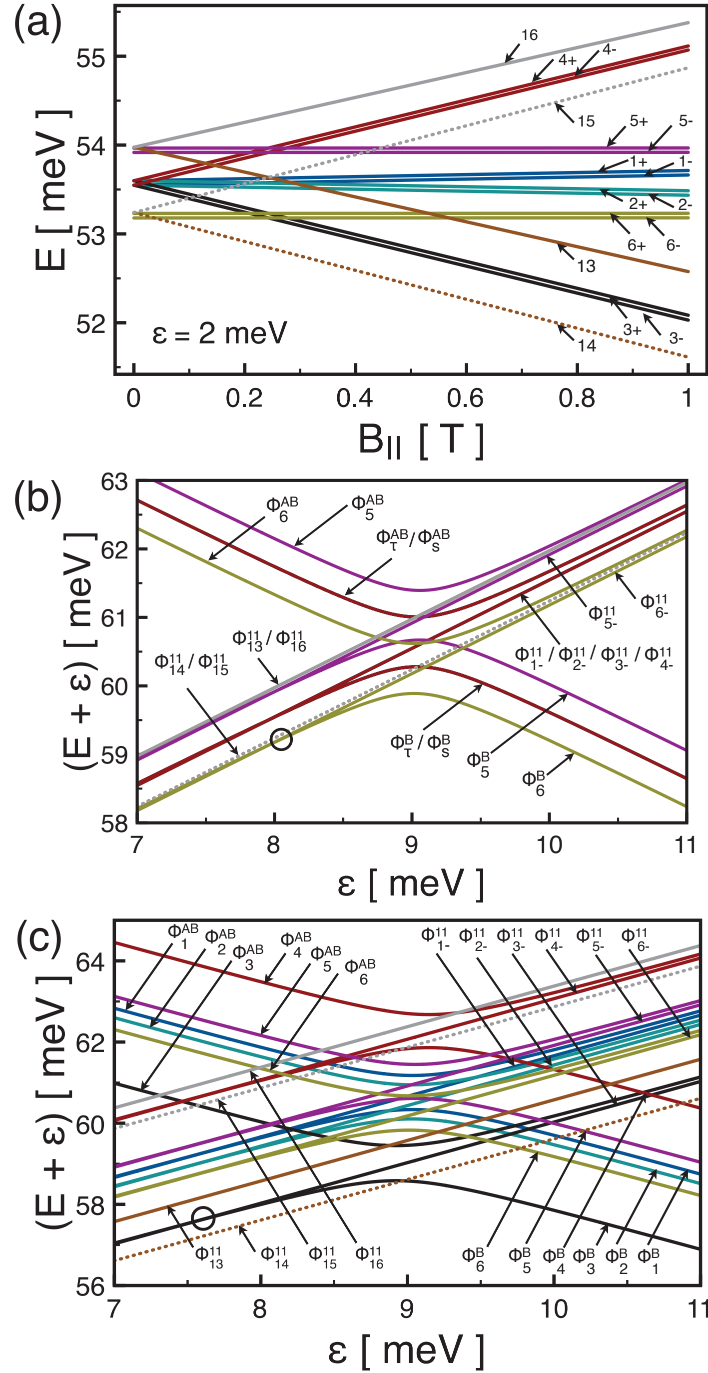

Figure 2.8: (a) Energy spectrum as a function of parallel magnetic field for the sixteen states of (1,1) when the lowest longitudinal mode of each dot is occupied. Spin-orbit coupling (0.37 meV here), strong tunnel coupling (≈ 1 meV), and Coulomb interactions ($\kappa = 10$) are included, but no valley coupling. Due to Coulomb interaction, the ground state at $B = 0$ is anti-symmetric in L/R space and is not tunnel coupled to the groundstate of $(0, 2)$. (b) Connection of $(1, 1)$ and $(0, 2)$ charge states by tunnel coupling at $B_{||} = 0$. (c) Same as (b) at $B_{||} = 1$ T. All parts adapted from Ref. [88].

Chapter 3

A Ge/Si heterostructure nanowire-based double quantum dot with integrated charge sensor

Yongjie Hu[1†], Hugh O. H. Churchill[2†], David J. Reilly[2], Jie Xiang[1], Charles M. Lieber[1], 3, and Charles M. Marcus[2]

[1]Department of Chemistry and Chemical Biology, Harvard University, Cambridge, Massachusetts 02138

[2]Department of Physics, Harvard University, Cambridge, Massachusetts 02138

[3]School of Engineering and Applied Sciences, Harvard University, Cambridge, Massachusetts 02138

[†]Equal contribution.

This chapter is adapted from Ref. [108].

Abstract

Coupled electron spins in semiconductor double quantum dots hold promise as the basis for solid-state qubits [3, 109]. To date, most experiments have used III-V materials, in which coherence is limited by hyperfine interactions [6, 110, 111, 112]. Ge/Si heterostructure nanowires seem ideally suited to overcome this limitation: the predominance of spin-zero nuclei suppresses the hyperfine interaction and chemical synthesis creates a clean, defect-free system with highly controllable properties [113]. Here we present a top gate-defined double quantum dot based on Ge/Si heterostructure nanowires with fully tunable coupling between the dots and to the leads. We also demonstrate a novel approach to charge sensing in a one-dimensional nanostructure by capacitively coupling the double dot to a single dot on an adjacent nanowire. The double quantum dot and integrated charge sensor serve as an essential building block required to form a solid-state spin qubit free of nuclear spin.

3.1 Introduction

The potential of solid state spin qubits is underscored by the recent demonstration of coherent spin control in gate-defined double quantum dots (DQDs) with integrated charge sensors in GaAs two-dimensional electron gases (2DEGs) [6, 110]. Additionally, few-electron InAs nanowire single and DQD devices possess strong spin-orbit interactions, which may prove useful for spin control [114, 115, 116]. In III-V materials, however, hyperfine coupling limits electron spin coherence. As a result, the prospect of long coherence times in group-IV materials due to the predominance of spin-zero nuclei [117] has stimulated several proposals [118, 119, 120, 121] and significant experimental effort. Experimental progress includes realizations of DQDs in carbon nanotubes [21, 22, 23] and Si:P [122], as well as single dots in Si and Ge/Si nanowires [123, 113] and Si/Ge 2DEGs [124, 125, 126].

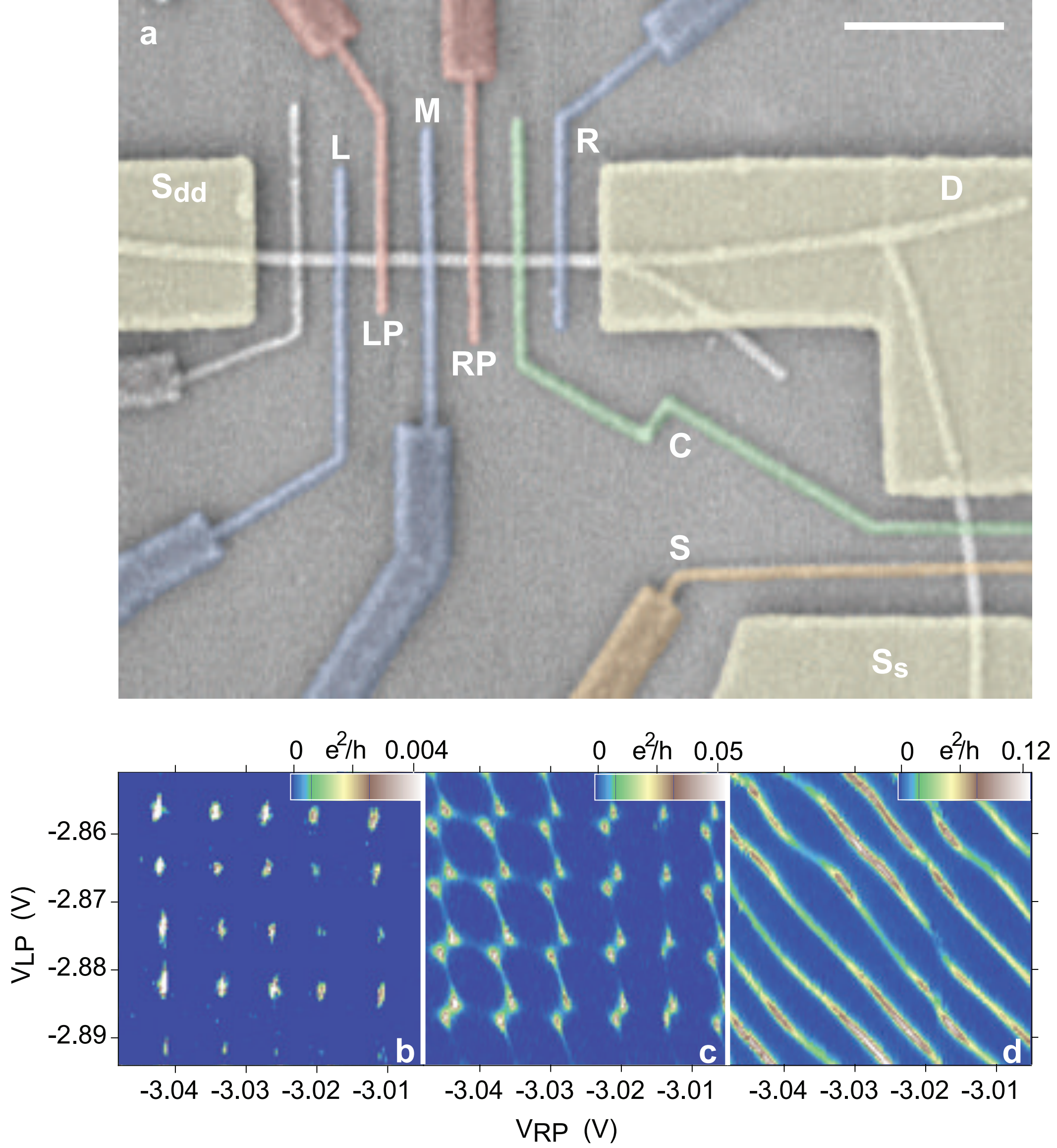

Figure 3.1: Ge/Si nanowire double dot device and demonstration of tunable interdot coupling. **a** SEM image of the actual device used for all measurements. The double dot is formed with gates L, M, and R shown in blue, and the plunger gates LP and RP (red) tune the energy levels of each dot. On an adjacent nanowire, the charge sensor is a contact-defined single dot capacitively coupled to the double dot with the coupler C (green). The sensor is biased to the side of a Coulomb blockade peak using gate S (orange). The gate shown in gray was not used. $S_{\rm dd}$, $S_{\rm s}$, and and D label double dot source, sensor source and shared drain contacts, respectively. Scale bar, 500 nm. **b**-**d** Differential conductance (color scale) is measured as a function of plunger voltages $V_{\rm LP}$ and $V_{\rm RP}$. With the side barriers fixed at $V_{\rm L} = -0.55$ V and $V_{\rm R} = 0$ V, changing the middle barrier voltage $V_{\rm M}$ shows three regimes of interdot coupling. **b** For weak interdot coupling ($V_{\rm M} = -0.72$ V), transport is allowed on an array of triple points corresponding to resonant alignment of energy levels in the two dots with the chemical potential of the leads. **c** At intermediate coupling ($V_{\rm M} = -0.85$ V), cross-capacitance and tunneling between dots split the triple points to create the honeycomb charging pattern. **d** For strong coupling ($V_{\rm M} = -2.15$ V), an effective single dot is formed, producing diagonal Coulomb blockade peaks.

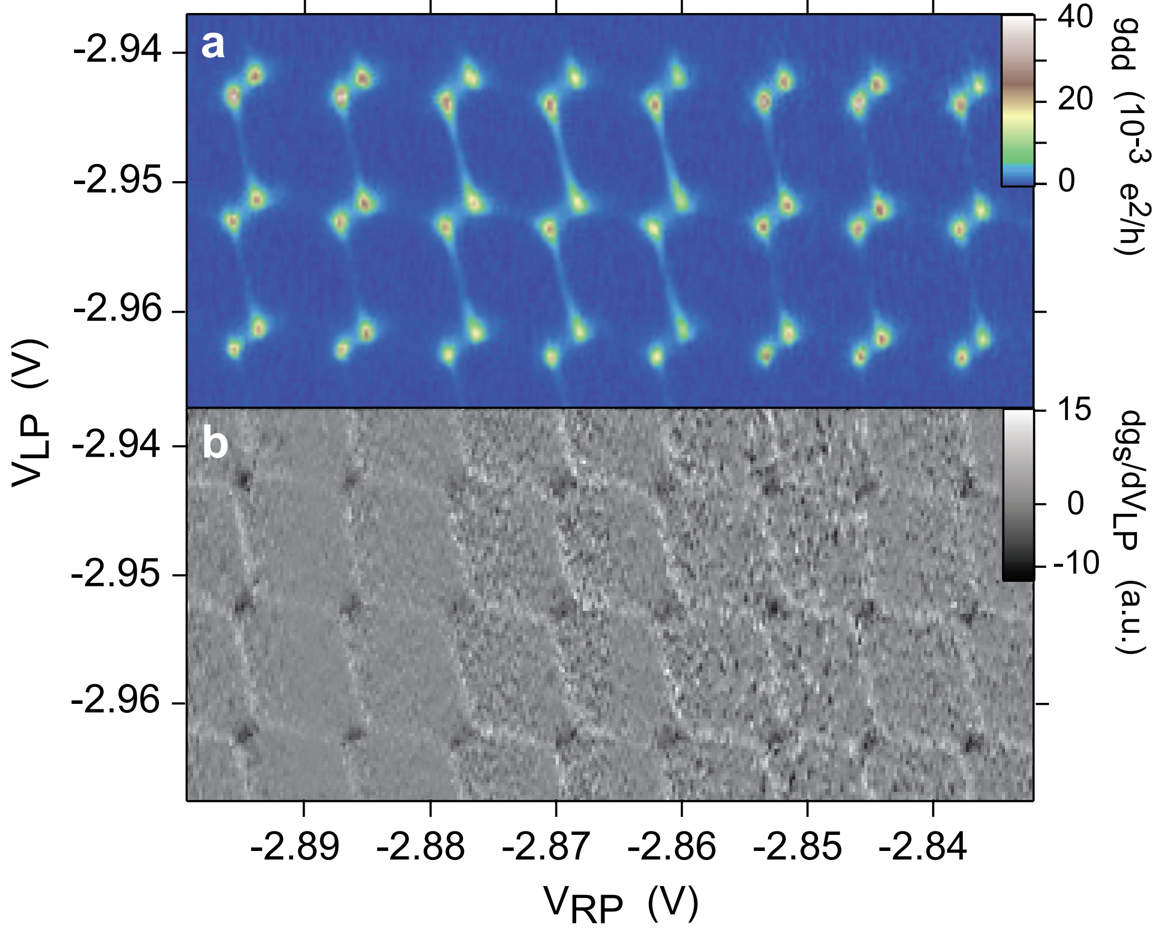

Figure 3.2: Simultaneous transport and charge sensing measurements. **a** Double dot conductance g_{dd} as a function of gate voltages V_{LP} and V_{RP}. **b** Simultaneously measured sensor dot conductance g_s, differentiated with respect to gate voltage V_{LP}.

3.2 Fabrication of devices and demonstration of tunable interdot coupling

The chemically synthesized Ge/Si core/shell heterostructure nanowires (NWs) used here provide a high mobility one-dimensional hole gas with a mean free path on the order of hundreds of nanometers at room temperature [113]. The $\sim$ 500 meV valence band offset between Ge and Si leads to a natural accumulation of holes in the Ge core, avoiding intentional impurity doping.

The DQD is formed by depleting a Ge/Si NW hole gas using metal gate electrodes. Three top gates, denoted L, M, and R in Fig. 3.1a, create barriers to define the dots, with the coupling between dots controlled by the middle barrier. Plunger gates LP and RP tune the energy levels of each dot. The device was measured in a dilution refrigerator with a base hole temperature, T_h, of 150 mK (see Methods).

Figures 3.1b–d show the differential conductance of the DQD, g_{dd}, as a function of plunger voltages V_{LP} and V_{RP}. With the side barrier voltages fixed at $V_{\mathrm{L}} = -0.55$ V and $V_{\mathrm{R}} = 0$ V, changing the middle barrier voltage V_{M} shows three regimes of interdot coupling. For weak coupling ($V_{\mathrm{M}} = -0.72$ V), transport occurs at triple points where the energy levels of the two dots align with the chemical potential of the leads, resulting in a rectangular array of high conductance points. Setting V_{M} to -0.85 V increases the coupling so that cross capacitance and tunneling between dots split the triple points, creating the honeycomb charging pattern characteristic of DQDs (Fig. 3.1c) [127]. For strong coupling ($V_{\mathrm{M}} = -2.15$ V), a single dot is effectively formed (Fig. 3.1d). These data demonstrate fully tunable interdot coupling of the Ge/Si NW DQD.

Measuring the differential conductance of each single dot as a function of source-drain bias yields Coulomb diamonds (see Supplementary Information, Fig. 3.5), from which we extract charging energies $E_C = e^2/C_\Sigma$ of 3.1 (2.6) meV for the left (right) dot. Single-particle level spacing ~ 250 μeV was also measured from Coulomb diamonds. Counting the charge transitions before tunnel rates inhibited further measurement, we place a lower bound of several hundred holes in each dot.

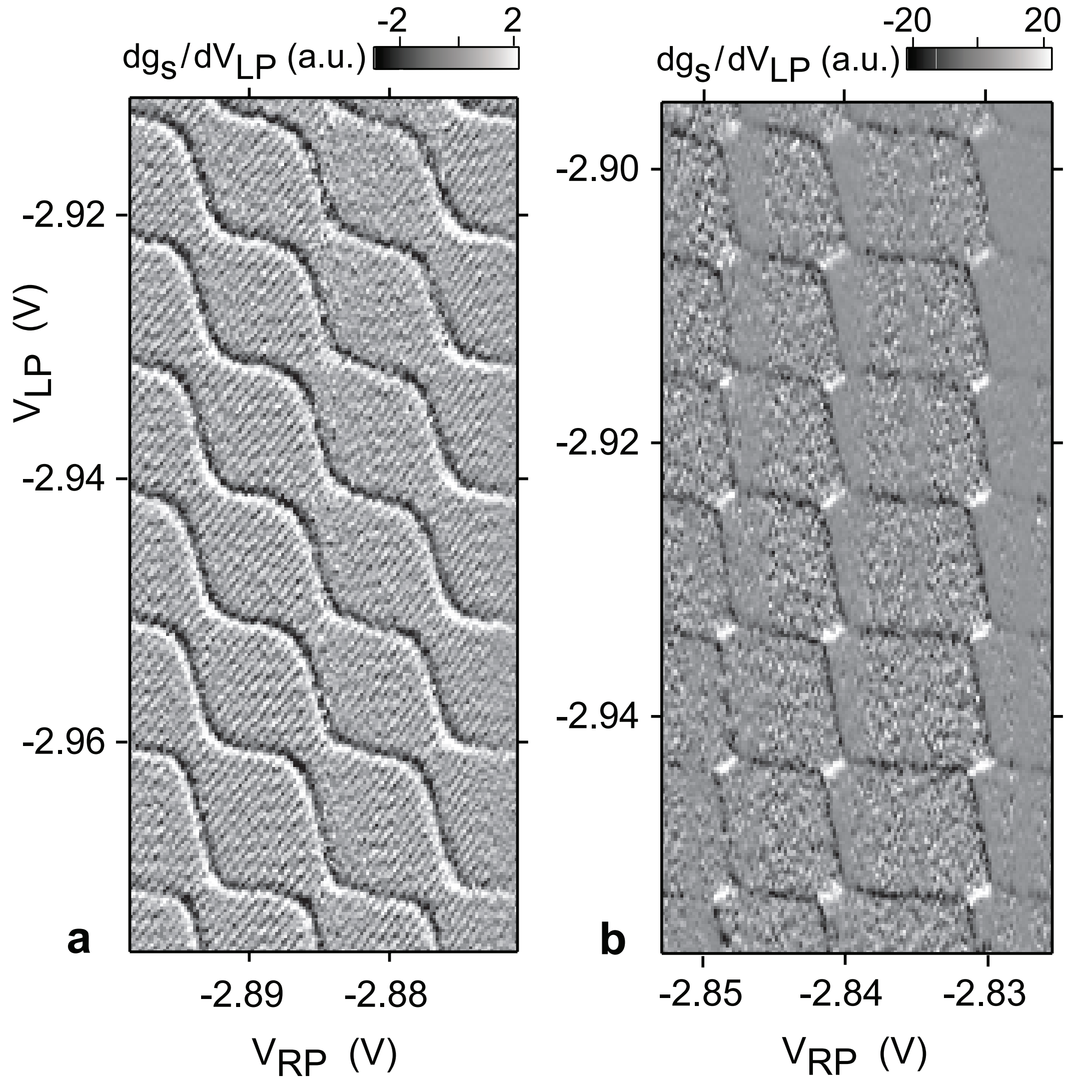

Figure 3.3: Charge sensing of an isolated double dot. Differentiated sensor conductance $\mathrm{dg_s/dV_{LP}}$ measured with the double dot weakly coupled to the leads ($\mathrm{g_{dd}} < 10^{-5}\ e^2/h$) for **a** strong ($V_\mathrm{M} = -859$ mV) and **b** weak interdot coupling ($V_\mathrm{M} = -845$ mV).

3.3 Charge sensing

Key to realizing few-electron devices in 2DEGs is the ability to noninvasively read out the charge state of the DQD, even when the tunnel coupling to the leads makes the current immeasurably small [128]. Among one-dimensional systems, charge sensing was demonstrated in a carbon nanotube single dot using a radio-frequency single electron transistor [129]. Here, we have developed a novel approach to charge sensing by capacitively coupling the DQD to a single dot on an adjacent nanowire. This method provides a simpler alternative in terms of fabrication. The charge sensor is a contact-defined dot capacitively coupled to the DQD with the coupler C (green, Fig. 3.1a). Gate S biases the sensor dot to the side of a Coulomb blockade peak for maximum sensitivity to changes in the number of holes on the DQD (see Supplementary Information, Fig. 3.6).

To test the sensor, we made simultaneous transport and charge sensing measurements in the intermediate coupling regime ($V_{\mathrm{M}} = -0.86$ V). Figure 3.2a shows the honeycomb pattern of g_{dd} as a function of V_{LP} and V_{RP}. Figure 3.2b shows the sensor conductance, g_{s}, measured simultaneously with g_{dd} and numerically differentiated with respect to V_{LP}. With the sensor biased on the negative slope of a Coulomb blockade peak, transfer of a hole from one dot to the leads produces a step up in conductance while transfer of a hole from the left dot to the right dot results in a step down (see Supplementary Information, Fig. 3.6). These steps up and down are observed in Fig. 3.2b as bright and dark features, respectively.

To demonstrate the advantage of the sensor to probe regimes inaccessible to transport, we next decouple the DQD from the leads by setting $V_{\mathrm{L}} = 0$ mV and $V_{\mathrm{R}} = 250$ mV so that $g_{\mathrm{dd}} < 10^{-5} e^2/h$. Figures 3.3a, b show dg_s/dV_{LP} for both (a) strong and (b) weak interdot coupling. Clear honeycomb charging patterns are seen. In Fig. 3.3a the sensor dot

is biased near the top of a Coulomb blockade peak where g_s responds nonlinearly both to the charge transitions on the DQD and to the compensation (see Methods) applied to gate S, resulting in a peak in g_s rather than a step. We also note that the sign of dg_s/dV_{LP} in Fig. 3.3b is reversed relative to that in Fig. 3.2b because the sensor dot is biased in a positive slope position.

3.4 Charging sensing of interdot transitions and measurement of tunnel coupling

Significantly, the sensor also responds to interdot transitions at fixed total charge which are difficult to study in transport [130]. Following the "detuning" diagonal ϵ (dotted line, inset to Fig. 3.4) from negative to positive transfers charge from the right dot to the left dot, resulting in a sensor conductance step. Denoting by (M, N) the charge state with M (N) holes on the left (right) dot, we model the sensor conductance across the transition from $(M+1, N)$ to $(M, N+1)$ as an isolated two-level system in thermal equilibrium [130]. When the tunnel coupling t is small relative to the individual dot single-particle level spacings, sensor conductance depends on detuning ϵ as

$$\mathrm{g_s} = \mathrm{g_0} + \delta\mathrm{g}\,\frac{\epsilon}{\Omega}\,\tanh\left(\frac{\Omega}{2k_B T_h}\right), \tag{3.1}$$

where $\Omega = \sqrt{\epsilon^2 + 4t^2}$ is the ground and excited state energy splitting. Rescaling the sensor conductance so that $\mathrm{g_0} = \delta\mathrm{g} = 1/2$ yields the excess charge on the left dot, $\langle m \rangle - M$. Measurements of excess charge versus detuning are plotted in Figs. 3.4a, b, and good agreement is achieved by fits to the model of eq. 3.1 (solid lines).

Because the transition width depends on both temperature and tunneling, we first calibrate the hole temperature (which may be higher than thermometry readings) by measuring the transition at elevated temperatures where the holes are well thermalized

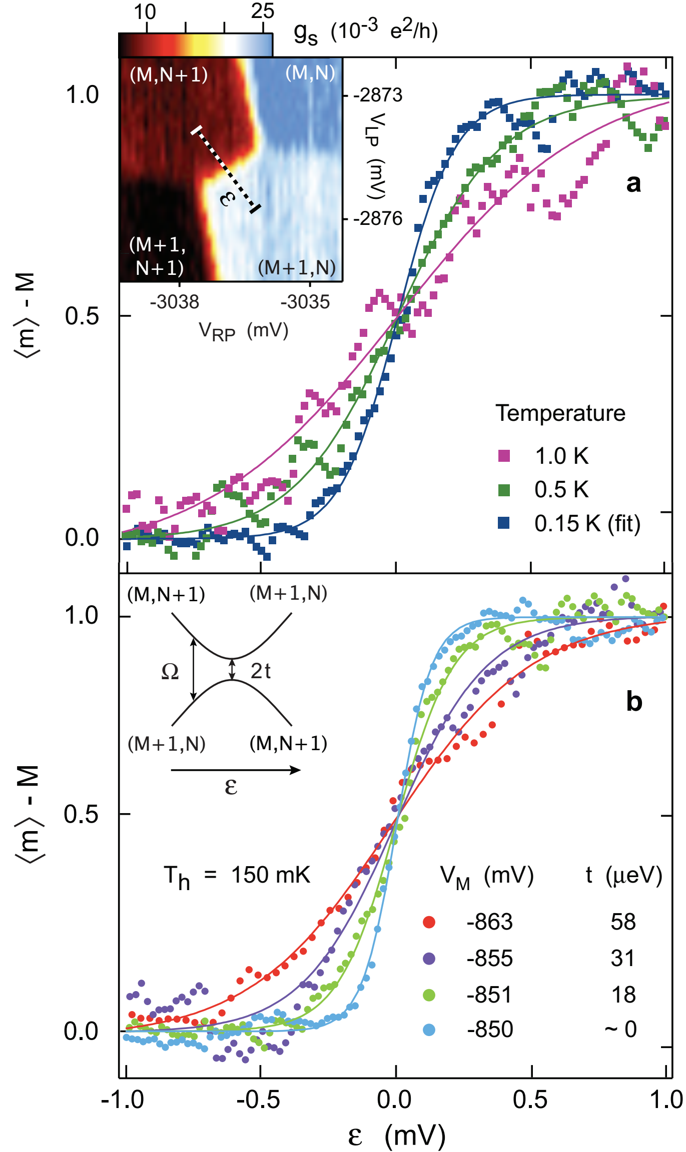

Figure 3.4: Interdot tunneling measured with charge sensor. **a** Sensor conductance g_s rescaled to reflect excess charge (in units of e) on the left dot along the detuning diagonal ϵ (dotted line in inset shows $\epsilon = -1$ to 1 mV) at $T_h = 0.15$ K (dark blue), 0.5 K (dark green), and 1.0 K (pink) for $V_{\rm M} = -851$ mV. The solid lines are fits to equation (3.1). Inset: sensor conductance g_s showing the charge stability diagram in the region used for **a** and **b**. The charge state with M (N) holes on the left (right) dot is denoted (M,N). Average values of g_s are 6.5, 8.4, 23, and 26 $\times$ 10^{-3} e^2/h on the black, red, white, and blue plateaus, respectively. **b** Excess charge on the left dot (g_s, rescaled) at base temperature for several values of $V_{\rm M}$. The temperature-broadened curve (blue) widens as $V_{\rm M}$ is made more negative, increasing the tunnel coupling t which is extracted from fits to Eq. (3.1) (solid lines). The fit to the temperature-broadened curve gives a base hole temperature of 150 mK, in agreement with Coulomb blockade peak widths. Inset: schematic energy diagram of the two-level system model, showing the splitting between ground and excited states as a function of detuning ϵ with an anticrossing of $2t$ at $\epsilon = 0$. Each of the curves in **a** and **b** is an average of 100 sweeps, and the inset to **a** is an average of 35 two-dimensional scans.

(Fig. 3.4a). Data at the highest temperatures (0.75 and 1.0 K) provide the lever arm used to estimate a base hole temperature of 150 mK for the blue curve in Fig. 3.4a, in agreement with Coulomb blockade peak widths. We now examine the sensing transition as a function of interdot tunneling in the regime $t \gtrsim k_B T_h$. Figure 3.4b shows excess charge along the detuning diagonal for several values of V_{M} at base temperature. For $V_{\mathrm{M}} = -850$ mV the transition did not narrow for less negative V_{M}, indicating a thermally broadened transition with $t \sim 0$. For the more negative values of V_M, fixing $T_h = 150$ mK allows extraction of the tunnel couplings t as the only free parameter in fits to equation (3.1).

3.5 Conclusion

In conclusion, we have demonstrated a fully tunable DQD in a Ge/Si heterostructure NW using local gate electrodes. We also presented a novel approach to charge sensing by capacitively coupling the DQD to a single dot on an adjacent NW. Having integrated these two components, future devices may address the challenge of accessing the few-charge regime and carrying out coherent spin manipulation experiments. The prospects of forming spin qubits with Ge/Si NW DQDs are bright. Long spin coherence times are expected to result from suppressed hyperfine interactions due to the absence of nuclear spin. Because of strong spin-orbit interactions in the valence band, hole spin lifetimes generally are shorter than those of electrons, but appropriate conditions enhance hole spin lifetimes [131, 132]. In our system quantum confinement and strain-induced splitting of the heavy-hole and light-hole subbands may reduce spin-orbit interactions [117, 133]. Furthermore, the observed ambipolar behavior in these NWs [113] ensures electron and hole conduction and suggests the possibility of studying electron and hole spins in the same device. This clean, highly controllable system offers a promising route to studies of coherent electronic devices free of

nuclear spin.

3.6 Methods

3.6.1 Fabrication of Ge/Si NW Devices

The undoped Ge/Si core/shell NWs were grown via a two-step chemical vapor deposition process [113]. The nanowires have an average core diameter of 14.6 nm and Si shell thickness of 1.7 nm, and normally exhibit $\langle 110 \rangle$ growth direction. AFM measurements of the nanowires forming the actual device presented here indicate $\sim$15 nm diameter for the DQD NW and $\sim$10 nm diameter for the sensor NW. The degenerately doped Si substrate with 600 μm thermal oxide served as a global backgate and was set to -2 V for all measurements. All source-drain contact electrodes (50 nm Ni) were defined by electron-beam lithography and deposited by thermal evaporation. Transparent contacts were obtained for the DQD NW, while contact barriers for the sensor nanowire formed a dot at low temperature, possibly due to its smaller diameter or to a thicker native oxide layer on the shell. The NWs and source-drain electrodes were then covered with a 12 nm HfO_2 high dielectric constant layer ($\kappa \sim 23$) using atomic layer deposition. HfO_2 was deposited at 110 °C in 100 cycles of 1 s water vapor pulse, 5 s N_2 purge, 3 s precursor, and 5 s N_2 purge. Tetrakis (dimethylamino) hafnium [$Hf(N(CH_3)_2)_4$] was used as precursor. Electron-beam lithography was used to define the top gates, followed by thermal evaporation of Al (50 nm). Top gates were approximately 30 nm wide with 110 nm spacing.

3.6.2 Measurements

An ac excitation of 10 μV was applied to the source contacts of the DQD and sensor at 149 and 109 Hz, respectively. The shared drain contact was connected to a current

preamplifier, followed by separate lock-in amplifiers to measure the DQD conductance g_{dd} and the sensor conductance g_{s}. To cancel the cross-coupling between gates and maintain the sensor in a high-sensitivity position, the sensor plunger voltage V_{S} was adjusted during sweeps of V_{LP} and V_{RP}.

Acknowledgments

We thank L. DiCarlo and E. A. Laird for experimental assistance and helpful discussions. CML acknowledges support from DARPA and Samsung Electronics. CMM acknowledges support from DTO. HOHC acknowledges support from the NSF.

3.7 Supplementary Figures

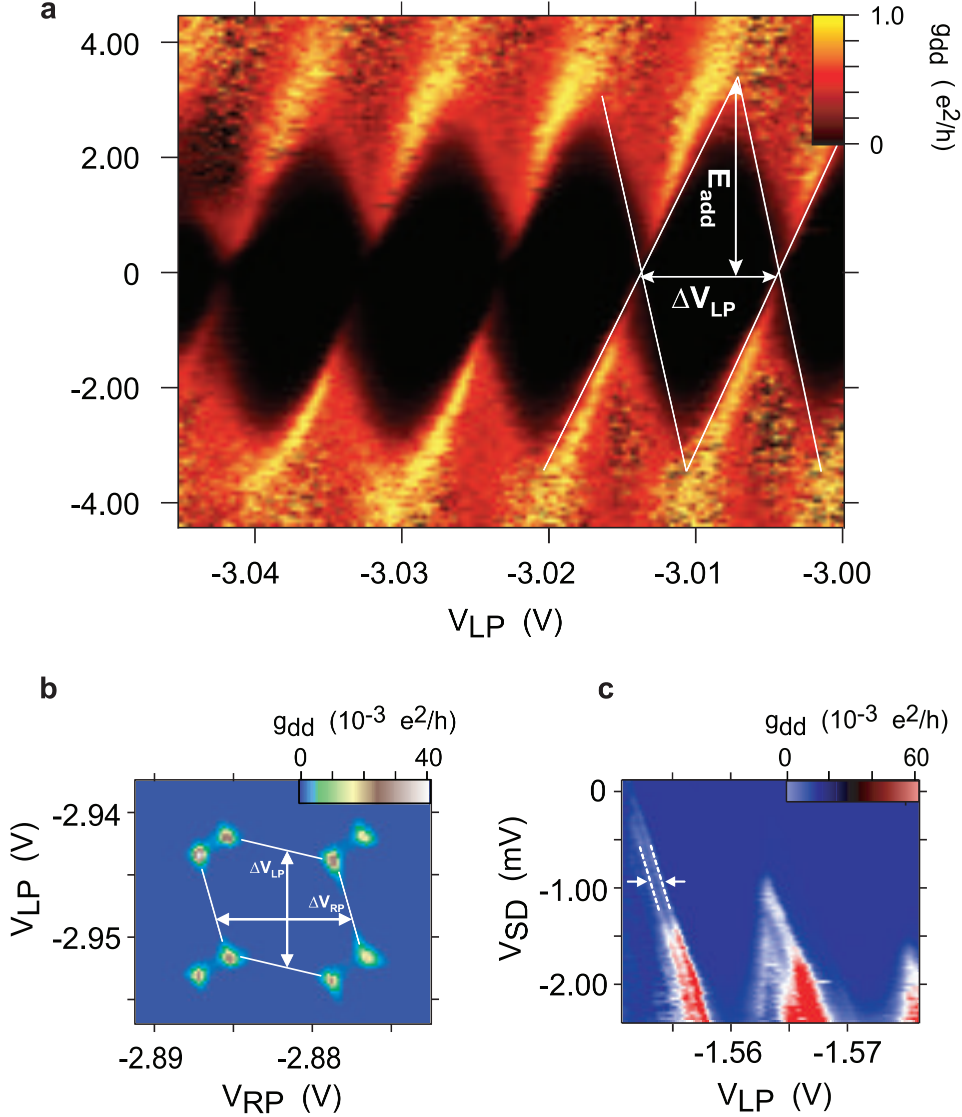

Figure 3.5: Extraction of single dot parameters. **a** With only the left dot of the DQD formed using gates L and M, differential conductance as a function of $V_{\rm SD}$ and $V_{\rm LP}$ shows Coulomb diamonds. Assuming the addition energy $E_{\rm add,L}$ and charging energy $E_{\rm C,L}$ are approximately equal, we extract from the diamonds a left dot charging energy $E_{\rm C,L} = e^2/C_{\Sigma,\rm L} \sim E_{\rm add,L} = 3.1$ meV, where the total capacitance for the left dot $C_{\Sigma,\rm L} = e^2/E_{\rm C,L} \sim 52$ aF. The plunger gate lever-arm $\eta = E_{\rm add}/e\Delta V_{\rm LP} \sim 0.32$, where $\Delta V_{\rm LP} \sim 9.6$ mV is the average peak spacing. We assume η to be approximately equal for both plunger gates LP and RP which have nearly identical widths. The left plunger gate capacitance $C_{\rm LP} = e/\Delta V_{\rm LP} \sim 17$ aF. **b** From the stability diagram (taken from Fig. 3.2a), we find the average peak spacing for the right dot $\Delta V_{\rm RP} \sim 8.2$ mV, total capacitance $C_{\Sigma,\rm R} = C_{\Sigma,\rm L}\,(\Delta V_{\rm LP}/\Delta V_{\rm RP}) \sim 61$ aF, right plunger gate capacitance $C_{\rm RP} \sim 20$ aF, and charging energy $E_{\rm C,R} \sim 2.6$ meV. The interdot capacitance is calculated to be ~ 15 aF. **c** Higher-resolution plot of left dot diamonds for less negative $V_{\rm LP}$ compared to **a**, showing excited states (indicated with arrows) from which a single-particle level spacing ~ 250 μeV is extracted. The relation of capacitances to stability diagram dimensions follows Ref. [127].

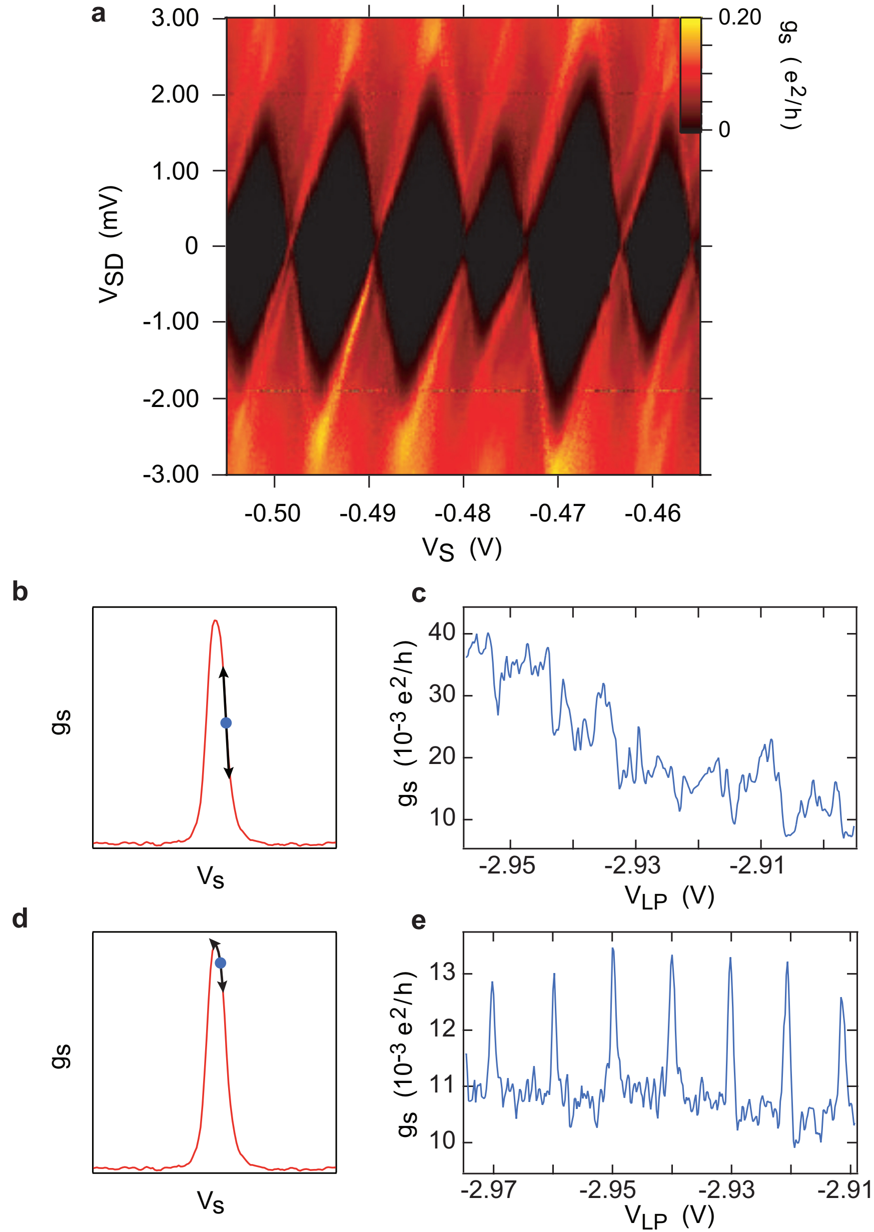

Figure 3.6: Characterization of sensor dot and illustration of charge sensing. **a** Coulomb diamonds for sensor dot. **b** and **c** Schematic sensor dot bias position and sensor response to charge transitions for the conditions of Fig. 3.3b. The sensor operates by gating the sensor dot with the changes in electrostatic potential associated with charge transitions in the DQD. With the sensor dot biased on the negative slope of a Coulomb blockade peak, transfer of a hole from one dot to the leads results in a step up in conductance due to the decreased electrostatic potential in the sensor dot. On the other hand, transfer of a hole from the left dot to the right dot results in a step down in conductance because the sensor coupler is closer to the right dot. When the sensor dot is biased in the linear regime of the Coulomb blockade peak (as shown in **b**), a sawtooth-like sensor signal is observed as in **c** (one-dimensional slice taken from Fig. 3.3b). In contrast, when the sensor dot is biased near the top of the peak (as shown in **d**), the response is nonlinear, and a sharp peak may be observed at the charge transitions as in **e** (one-dimensional slice taken from Fig. 3.3a).

Chapter 4

Electron-nuclear interaction in ^{13}C nanotube double quantum dots

H. O. H. Churchill, A. J. Bestwick, J. W. Harlow, F. Kuemmeth, D. Marcos,

C. H. Stwertka, S. K. Watson[†], and C. M. Marcus

Department of Physics, Harvard University, Cambridge, Massachusetts 02138

This chapter is adapted from Ref. [96].

[†]Permanent address: Department of Physics, Middlebury College, Middlebury, Vermont 05753, USA.

Abstract

For coherent electron spins, hyperfine coupling to nuclei in the host material can either be a dominant source of unwanted spin decoherence [112, 6, 110] or, if controlled effectively, a resource allowing storage and retrieval of quantum information [118, 15, 16, 134]. To investigate the effect of a controllable nuclear environment on the evolution of confined electron spins, we have fabricated and measured gate-defined double quantum dots with integrated charge sensors made from single-walled carbon nanotubes with a variable concentration of ^{13}C (nuclear spin $I = 1/2$) among the majority zero-nuclear-spin ^{12}C atoms. We observe strong isotope effects in spin-blockaded transport, and from the magnetic field dependence estimate the hyperfine coupling in ^{13}C nanotubes to be on the order of 100 μeV, two orders of magnitude larger than anticipated [98, 97]. ^{13}C-enhanced nanotubes are an interesting system for spin-based quantum information processing and memory: the ^{13}C nuclei differ from those in the substrate, are naturally confined to one dimension, lack quadrupolar coupling, and have a readily controllable concentration from less than one to 10^5 per electron.

4.1 Introduction

Techniques to prepare, manipulate, and measure few-electron spin states in quantum dots have advanced considerably in recent years, with the leading progress in III-V semiconductor systems [135, 6, 110, 4]. All stable isotopes of III-V semiconductors, such as GaAs, have nonzero nuclear spin, and the hyperfine coupling of electron spins to host nuclei is a dominant source of spin decoherence in these materials [112, 136, 6, 137]. To eliminate this source of decoherence, group IV semiconductors—various forms of carbon, silicon, and silicon-germanium—which have predominantly zero nuclear spin, are being vig-

orously pursued as the basis of coherent spin electronic devices. Double quantum dots have recently been demonstrated in carbon nanotubes [21, 22, 23], including the investigation of spin effects [25, 26].

4.2 Device fabrication and quantum dot formation

The devices reported are based on single-walled carbon nanotubes grown by chemical vapor deposition using methane feedstock containing either 99% ^{13}C (denoted ^{13}C devices) or 99% ^{12}C (denoted ^{12}C devices; see Methods)[138]. The device design (Fig. 4.1a) uses two pairs of Pd contacts on the same nanotube; depletion by top-gates (blue, green, and gray in Fig. 4.1a) forms a double dot between one pair of contacts and a single dot between the other. Devices are highly tunable, as demonstrated in Fig. 4.1, which shows that tuning the voltage on gate M (Fig. 4.1a) adjusts the tunnel rate between dots, allowing a cross-over from large single-dot behavior (Fig. 4.1b) to double-dot behavior (Fig. 4.1c). Left and right tunnel barriers can be similarly tuned using the other gates shown in blue in Fig. 4.1a.

A notable feature of nanotube quantum dots that is not shared by GaAs dots is that the energy required to add each subsequent electron, the addition energy, often shows shell-filling structure even in the many-electron regime [25]. An example of a shell-filling pattern, with larger addition energy every fourth electron in the right dot, is seen in Fig. 4.1d. We find, however, that evident shell filling is not necessary to observe spin blockade at finite bias. Figures 4.2a and 4.2b show current through the double dot, I_{dd}, as a function of gate voltages V_{R} and V_{L} for a weakly coupled, many-electron ^{13}C double dot at +1 and −1 mV source-drain bias, respectively, in a range of dot occupancy that does not show shell structure in the addition spectrum of either dot. With a magnetic

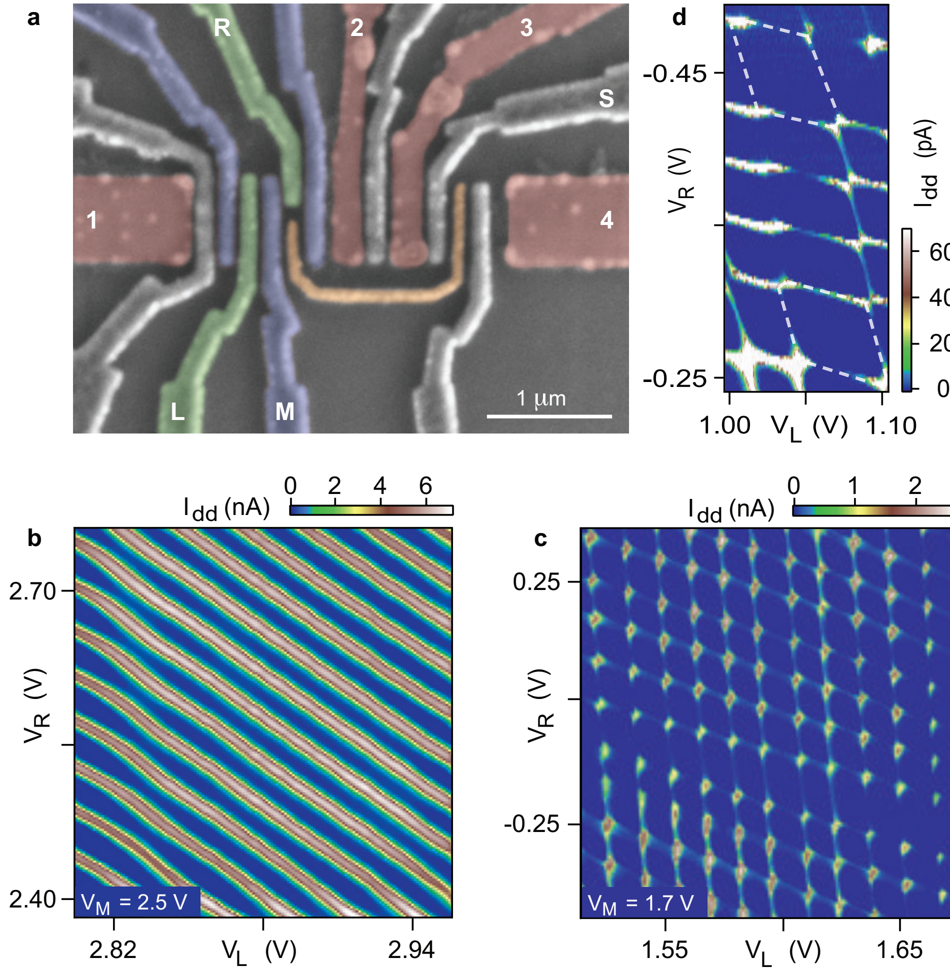

Figure 4.1: Nanotube double dot with integrated charge sensor. **a**, SEM micrograph (with false color) of a device similar to the measured ^{12}C and ^{13}C devices. The carbon nanotube (not visible) runs horizontally under the four Pd contacts (red). Top-gates (blue) create voltage-tunable tunnel barriers allowing the formation of a single or double quantum dot between contacts 1 and 2. Plunger gates L and R (green) control the occupancy of the double dot. A separate single dot contacted by Pd contacts 3 and 4 is controlled with gate plunger gate S (gray) and is capacitively coupled to the double dot via a coupling wire (orange). **b**, Current through the double dot, $I_{\rm dd}$, (color scale) with the top-gates configured to form a large single dot. **c**, When carriers beneath the middle gate, M, are depleted, $I_{\rm dd}$ shows typical double-dot transport behavior, demarcating the honeycomb charge stability pattern. **d**, Within certain gate voltage ranges, honeycomb cells with larger addition energy and fourfold periodicity (outlined with dashed lines) indicate the filling of spin and orbital states in shells. Source-drain bias is -1.0 mV for **b**, **c**, and **d**.

field $B_{||} = 200$ mT applied along the tube axis, current flow is observed throughout the finite-bias triangles at positive bias, but is suppressed at negative bias for detuning below 0.8 meV, which presumably indicates where an excited state of the right dot enters the

transport window.

4.3 Spin blockade and charge sensing

Current rectification of this type is a hallmark of spin blockade [135] (Fig. 4.2e): at positive bias, current flows freely as electrons of appropriate spin are drawn from the right lead to form the singlet ground state; at negative bias, current is blocked whenever a triplet state is formed between separated electrons, as the excess electron on the left can neither reenter the left lead nor occupy the lowest orbital state on the right without flipping its spin. Spin blockade was identified in all four devices measured, two each of ^{12}C and ^{13}C. Spin blockade was occasionally found to follow a regular even-odd filling pattern, as seen in few-electron GaAs dots [139], though no pattern was seen adjacent to the area in Fig. 4.2.

Electrostatic sensing of the double-dot charge state is provided by a gate-defined quantum dot formed on a separately contacted portion of the same nanotube. The sensing dot is capacitively coupled to the double dot by a ~ 1 μm coupling wire [108] (orange gate in Fig. 4.1a) but electrically isolated by a depletion gate between the Pd contacts. Charge sensor conductance g_s as a function of V_R and V_L, acquired simultaneously with transport data in Fig. 4.2a,b, is shown in Fig. 4.2c,d. The location of the coupling wire makes g_s sensitive to the occupancy of the right dot with no observable sensitivity to the left dot. Inside the positive-bias triangles (Fig. 4.2c), g_s is intermediate in value between their bordering regions, indicating that the excess electron is rapidly shuttling between the dots as current flows through the double dot. In contrast, inside the negative-bias triangles (Fig. 4.2d), g_s shows no excess electron on the right dot as a result of spin blockade.

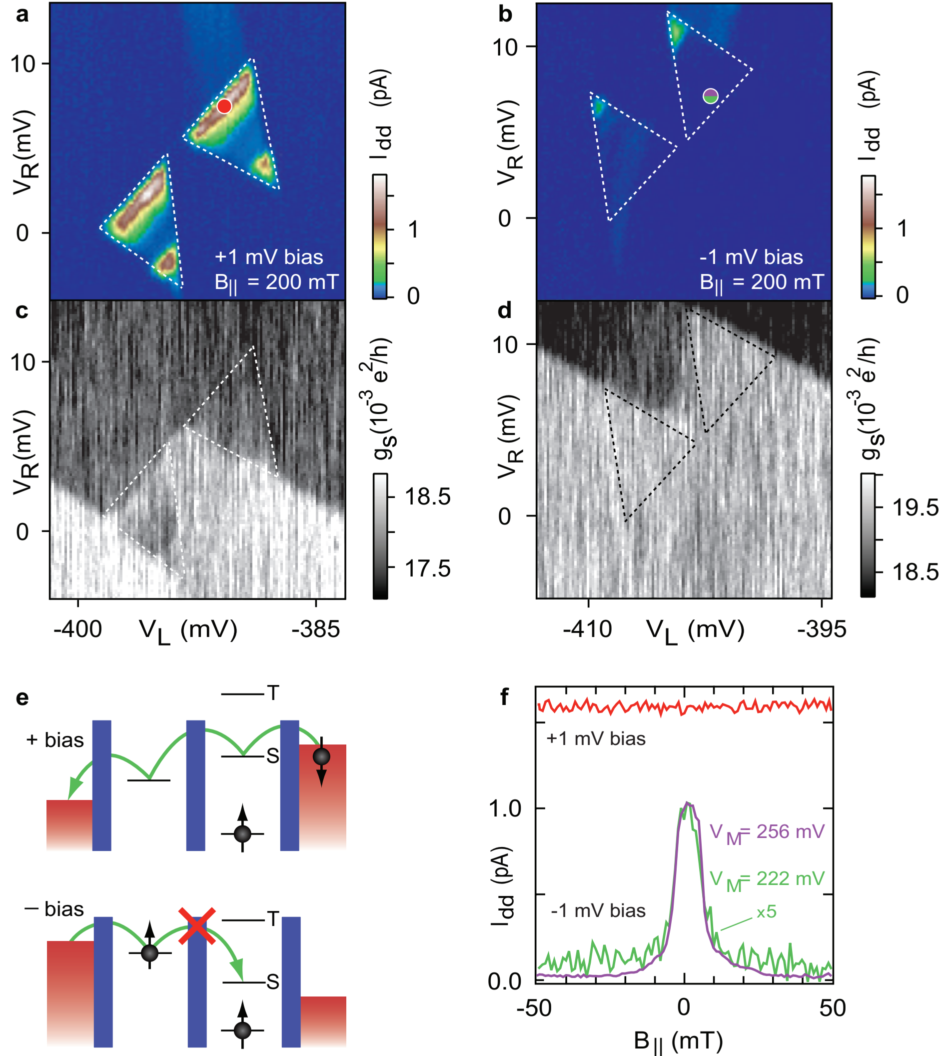

Figure 4.2: Spin blockade in a ^{13}C nanotube double dot. **a**, Current $I_{\rm dd}$ (color scale) at +1.0 mV source-drain bias, the non-spin-blockaded bias direction. Transport is dominated by resonant tunneling through the ground state at the base of the finite bias triangles and through an excited state at a detuning of 0.7 meV. **b**, $I_{\rm dd}$ (color scale) at −1.0 mV source-drain bias, the spin-blockaded bias direction. $I_{\rm dd}$ is suppressed except near the tips of the transport triangles. Suppressed transport for one bias direction is the signature of spin blockade. **c**, Charge sensing signal, g_s, (conductance of the sensing dot between contacts 3 and 4 in Fig. 4.1a), acquired simultaneously with **a** detects the the time-averaged occupation of the right dot. **d**, Charge sensing signal g_s for −1.0 mV bias (blockade direction). In **a**–**d** dashed lines indicate allowed regions for current flow in the absence of blockade. **e**, Schematic of spin-blockaded transport. Any spin may occupy the left dot, but only a spin singlet is allowed in the right dot, suppressing negative bias current once an electron enters the left dot and forms a triplet state. **f**, Current $I_{\rm dd}$ near zero detuning (position marked by circles in **a** and **b**) as a function of magnetic field for positive bias (non-blockade, red trace) and negative bias (blockade, for two values of $V_{\rm M}$, purple and green traces). For $V_{\rm M}$ = 222, $I_{\rm dd}$ was multiplied by 5.

4.4 Comparison of ^{12}C and ^{13}C spin blockade

The magnetic field dependence of spin blockade provides important information about electron spin relaxation mechanisms [140, 141]. A first look at field dependence (Fig. 4.2f) for a ^{13}C device shows that for negative bias (purple and green), spin-blockade leakage current is strongly peaked at $B_{||} = 0$, while for positive bias (red), the unblockaded current does not depend on field. The peak in leakage current is shown for two values of V_{M}, indicating that the width of the peak is independent of interdot tunnel coupling t. As discussed below, this field dependence can be understood in terms of hyperfine-mediated spin relaxation.

The striking difference in field dependence of spin-blockade leakage current between ^{12}C and ^{13}C devices is illustrated in Fig. 4.3a,b. These data show that for negative (spin-blockaded) bias, leakage current is a minimum at $B_{||} = 0$ for the ^{12}C device and a maximum at $B_{||} = 0$ for the ^{13}C device. In fourteen instances of spin blockade measured in four devices (two ^{13}C and two ^{12}C), we find that leakage current minima can occur at $B_{||} = 0$ in both ^{12}C and ^{13}C devices, particularly for stronger interdot tunneling. For weak interdot tunneling, however, only the ^{13}C devices show maxima of spin-blockade leakage at $B_{||} = 0$, presumably because the width and height of this feature are strongly suppressed in ^{12}C nanotubes. In all cases, the positive bias (non-spin-blockade) current shows no appreciable field dependence.

Figure 4.3e shows spin-blockade leakage current as a function of $B_{||}$ at fixed detuning (the detuning value is shown as a black line in Fig. 4.3a), along with a best-fit lorentzian, for the ^{12}C device. The lorentzian form was not motivated by theory, but appears to fit rather well. The width of the dip around $B_{||} = 0$ decreases with decreasing interdot tunneling (configuration Fig. 4.3e has $t \sim 50$ μeV, based on charge-state transition width [108]),

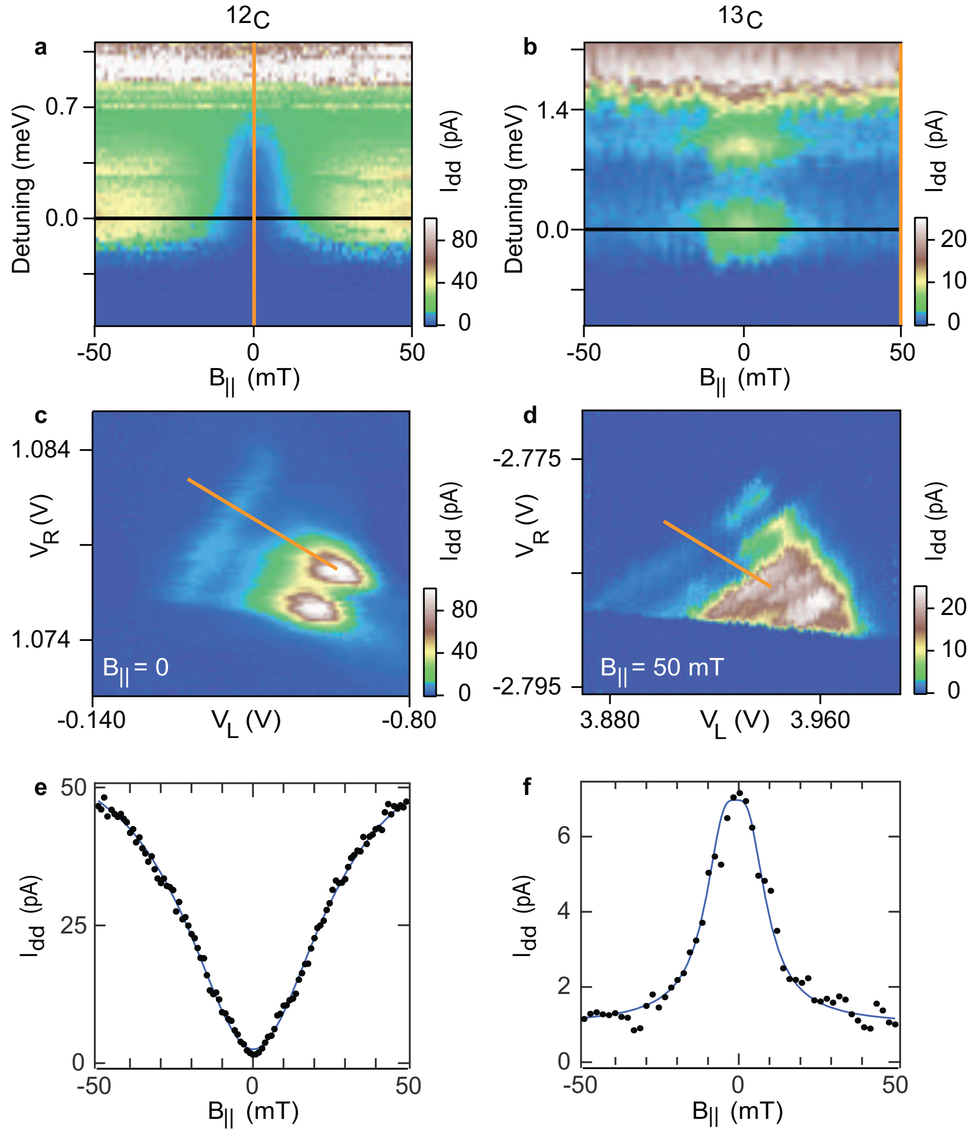

Figure 4.3: Contrasting magnetic field dependence of leakage current for ^{12}C and ^{13}C devices. Leakage current through spin blockade (color scale) as a function of detuning and magnetic field, $B_{||}$, for ^{12}C (**a**) and ^{13}C (**b**) devices. The vertical axes in **a** and **b** are interdot detuning as indicated by the orange lines in **c** and **d**, respectively. In **a** $B_{||}$ was swept and detuning stepped, while in **b** detuning was swept and $B_{||}$ stepped. Bias is -1.5 mV in **c** and -4 mV in **d**. **e** and **f** show cuts along $B_{||}$ at the detunings indicated by the red lines in **a** and **b**, respectively. The fit in **e** is a Lorentzian with a width of 30 mT, and the fit in **f** is to the theory of Jouravlev and Nazarov [141], providing a measure of $B_{\text{nuc}} = 6.1$ mT.

which may explain why it is not observed in the weakly coupled regime of Fig. 4.3b,f. We note that a similar zero-field dip in spin-blockade leakage current was recently reported in a double dot formed in an InAs nanowire [142]. There the dip was attributed to spin-orbit coupling, an effect that is also present in carbon nanotubes [70].

4.5 Signatures of hyperfine coupling in ^{13}C nanotubes

Hyperfine coupling appears to the confined electrons as an effective local Zeeman field (the Overhauser field) that fluctuates in time independently in the two dots, driven by thermal excitation of nuclear spins. The difference in local Overhauser fields in the two dots will induce rapid mixing of all two-electron spin states whenever the applied field is less than the typical difference in fluctuating Overhauser fields (at higher fields, only the $m = 0$ triplet can rapidly mix with the singlet). How hyperfine-mediated spin mixing translates to a field dependence of spin-blockade leakage current was investigated experimentally in GaAs devices [140], with theory developed by Jouravlev and Nazarov [141].

Field dependence of spin-blockade leakage current for a weakly coupled ^{13}C double dot near zero detuning is shown Fig. 4.3f, along with a theoretical fit (Eq. (11) of Ref. [141], with a constant background current added), from which we extract a root mean square amplitude of fluctuations of the local Overhauser fields, $B_{\text{nuc}} = 6.1$ mT. We note that the width of the peak in Fig. 4.3f is independent of detuning (Fig. 4.3b), consistent with our interpretation that it is governed by B_{nuc} rather than t. Assuming gaussian distributed Overhauser fields and uniform coupling, B_{nuc} is related to the hyperfine coupling constant A by $g\mu_B B_{\text{nuc}} = A/\sqrt{N}$, where g is the electron g-factor and N is the number of ^{13}C nuclei in each dot [141]. Taking $N \sim 3$–10×10^4 and $g = 2$ (see Supplement), yields $A \sim 1$–2×10^{-4} eV, a value that is two orders of magnitude larger than predicted for carbon

nanotubes [98] or measured in fullerenes [97].

Signatures of dynamic nuclear polarization provide further evidence of a strong hyperfine interaction in ^{13}C double dots. Hysteresis in the spin-blockade leakage current near zero detuning is observed when the magnetic field is swept over a tesla-scale range, as shown in Fig. 4.4a. The data in Fig. 4.4a,b are from the same ^{13}C device as in Fig. 4.3, but with the barriers tuned such that cotunneling processes provide a significant contribution to the leakage current.

We interpret the hysteresis in Fig. 4.4a as resulting from a net nuclear polarization induced by the electron spin flips required to circumvent spin blockade [143]. We speculate that this nuclear polarization generates an Overhauser field felt by the electron spins that opposes $B_{||}$ once $B_{||}$ passes through zero. The value of the coercive field, $B_c \sim 0.6$ T, the external field at which the two curves rejoin, places a lower bound for the hyperfine coefficient, $A \geq g\mu_B B_c \sim 0.7 \times 10^{-4}$ eV (equality corresponding to full polarization), independent of the value inferred from the width of the leakage current peak around zero field (Fig. 4.3c). If we instead use the value of A inferred from the current peak width (Fig. 4.3c), the size of B_c implies a $\sim 50\%$ polarization for the data in Fig. 4.4a. Hysteresis is not observed for non-spin-blockaded transport in the ^{13}C devices and is not observed in the ^{12}C devices, suggesting that this effect cannot be attributed to sources such as the Fe catalyst particles or interaction with nuclei in the substrate or gate oxide.

Figure 4.4b shows that the induced nuclear polarization persists for ~ 10 minutes, two orders of magnitude longer than similar processes in GaAs double dots [144]. The long relaxation time indicates that nuclear spin diffusion is extremely slow, due both to the one-dimensional geometry of the nanotube and material mismatch between the nanotube and its surroundings. Field and occupancy dependence of relaxation were not measured.

Large fluctuations in I_{dd} are seen at some values of magnetic field, but not at others

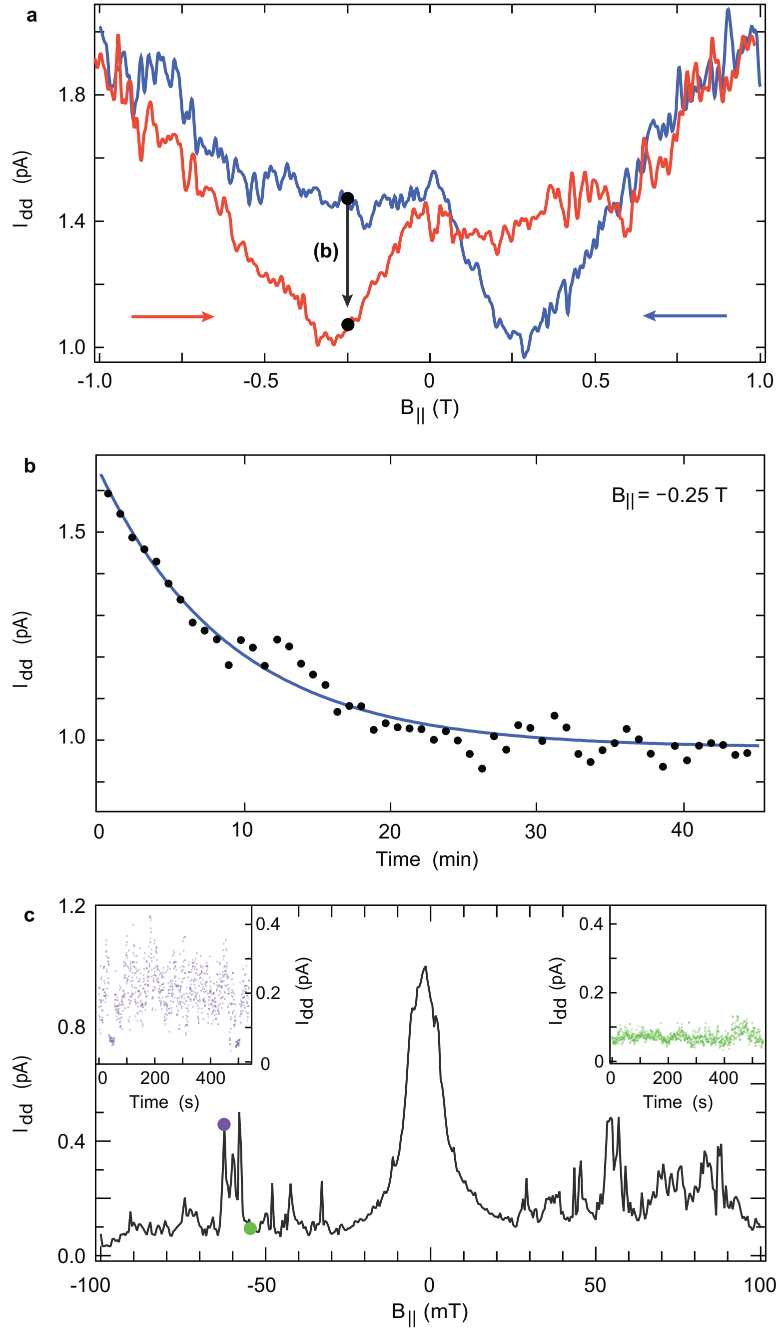

Figure 4.4: Hysteresis and fluctuations in leakage current. **a**, The spin-blockade leakage current for a ^{13}C device measured for decreasing (increasing) magnetic field (sweep rate 0.4 mT/s), shown in blue (red), after waiting at +1 T (−1 T) for 10 minutes. 2 mV source-drain bias is applied at all times. Hysteresis is seen on a field scale > 0.5 T for both sweep directions. **b**, Decay of leakage current over time measured by stopping a downward sweep at −0.25 T. The fit is to an exponential decay with a time constant of 9 min. **c**, Dependence of leakage current on $B_{||}$ near zero detuning in a second ^{13}C device. The leakage current fluctuates over time at some values of $B_{||}$, while remaining steady at others (insets).

(Fig. 4.4c), similar to behavior observed in GaAs devices [140]. This presumably reflects an instability in nuclear polarization that can arise when polarization or depolarization rates themselves are polarization dependent [145, 143].

4.6 Conclusions

An important conclusion of this work is that the hyperfine coupling constant, $A \sim 1$–2×10^{-4} eV, in the ^{13}C devices (for both electron and holes, see Methods) appears to be larger than anticipated [98, 97] and deserves further theoretical and experimental attention. It is possible that the substrate or gate oxide may enhance the degree of *s*-orbital content of conduction electrons, thus strengthening the contact hyperfine coupling. We also note that the one-dimensional character of charge carriers in ^{13}C nanotubes may greatly enhance the effective electron-nuclear interaction [101]. Finally, the large value of A motivates the fabrication of isotopically enriched ^{12}C nanotubes to reduce decoherence and the use of ^{13}C tubes as a potential basis of electrically addressable quantum memory.

4.7 Methods

Carbon nanotubes are grown by chemical vapor deposition using methane feedstock and 5 nm thick Fe catalyst islands on degenerately doped Si substrates with 1 μm thermal oxide. ^{12}C devices are grown with methane containing natural abundance (1.1%) ^{13}C; ^{13}C devices are grown with 99% $^{13}CH_4$ (Sigma-Aldrich). Nanotubes are located after growth using a scanning electron microscope, and catalyst islands, source and drain electrodes (15 nm Pd), and top-gates (30 nm Al) are patterned using electron-beam lithography. After contacting with Pd, samples are coated with a noncovalent functionalization layer combining NO_2 and trimethylaluminum, followed by atomic layer deposition (ALD)

of a 30 nm Al_2O_3 top-gate insulator (Cambridge Nanotech Savannah ALD system) [103]. Measurements were performed in a dilution refrigerator with a base temperature of 30 mK and electron temperature of $\sim$ 120 mK, determined from the charge sensing transition width [108]. Nanotubes presented in Figs. 4.1 and 4.2 have small bandgaps ($E_g \sim$ 25 meV); the ^{13}C nanotube in Fig. 4.3b,d,f and the other ^{12}C nanotube (data not shown) are large-gap semiconducting nanotubes. Charges occupying the dots and leads are electrons, except the data in Fig. 4.3b,d,f and Fig. 4.4a,b, where the charge carriers are holes. No significant differences are seen between devices with electron and hole carriers.

Acknowledgements

We thank Michael Biercuk, Karsten Flensberg, Leo Kouwenhoven, Daniel Loss, Emmanuel Rashba and Oleg Yazyev for discussions, and David Reilly for experimental assistance. This work was supported in part by the National Science Foundation under grant no. NIRT 0210736 and the NSF-NNIN Program, ARO/iARPA, the Department of Defense, Harvard's Center for Nanoscale Systems. H.O.H.C. acknowledges support from the NSF.

4.8 Epilogue

The interpretation of the data in this chapter in terms of an extraordinarily large value for the hyperfine coupling in carbon nanotubes generated a great deal of interest in exploring alternative interpretations that do not require this parameter to be so completely out of scale. I am aware of three proposals in addition to those mentioned above, s-orbital mixing and an ordered nuclear state. Before describing the more recent suggestions, it is worth commenting on s-orbital mixing. As proposed by Emmanuel Rashba, an upper bound on the contact hyperfine coupling due to curvature-induced s-orbital mixing can be

obtained by assuming that the electrons occupy s-orbitals exclusively. In that case, the contact term is $A = 16\pi\mu_{13\mathrm{C}}\mu_B|\psi(0)|^2/3$ for $I = 1/2$. For a $2s$ orbital in a carbon atom, $|\psi(0)|^2 = Z^3/8\pi a_B^3$, where a_B is the Bohr radius. The upper bound on A due to curvature is therefore $A = 2\mu_{13\mathrm{C}}\mu_B Z^3/3a_B^3 \approx 20$ μeV, consistent with the estimate in Ref. [98] of 15 μeV.

One possible explanation for the wide peak in leak current we observed came from Palyi and Burkard who examined the role of valley mixing in lifting spin blockade in carbon nanotube double dots [91]. They found that blockade can be lifted by short-range disorder that couples valleys independently and randomly in the two dots, resulting in a valley-Zeeman field that produces effects similar to Overhauser fields in GaAs dots. For certain parameters, they predict a peak in leakage current at zero field due to this effect, but its width depends on interdot tunneling*, contrary to our observation in Fig. 4.2(f).

Another possibility was raised by Coish and Qassemi who examined the role of thermally activated spin-flip cotunneling in lifting spin blockade [146]. This theory found immediate application in two experiments on spin blockade in silicon double quantum dots [40, 41], but does not fit our ^{13}C data because the linewidth it predicts (set by temperature) is too large given the $\sim$ 100 mK temperature of our experiment. Matching the width in Fig. 4.3(f) would require a temperature $<$10 mK for $g = 2$.

A final proposal (Kiss *et al.*, Ref. [147]) suggested that we consider a different limit of the Jouravlev and Nazarov theory, in which the singlet-triplet splitting $\Delta_{ST} \gg B_{\mathrm{nuc}}$ rather than the other way around. This limit is the natural one to consider when a weak hyperfine coupling is expected, but it is inconsistent with our data. In this limit, the width of the zero field peak is set by $\Delta_{ST} \approx t^2/\Delta$, where Δ is the detuning. From this expression it is clear that the width of the peak depends on both tunneling and detuning, contrary to

*Andras Palyi and Guido Burkard, private communication.

our observations [cf. Fig. 4.2(f) and 4.3(b)].

Several years after the publication of this work, the large value of A remains the only interpretation consistent with our data, but the significant problem that it is inconsistent with known hyperfine effects in carbon nanotubes persists.

4.9 Supplementary Discussion

Our estimate of A extracted from the data in Fig. 4.3f depends on the assumption that, consistent with other measurements[70], $g \gtrsim 2$ in the nanotubes studied here. Our devices exhibit the large orbital magnetic moments in parallel magnetic field ($\sim$ 10 μ_B) common in nanotube quantum dots[69], but not at the spin-blockaded transitions used to estimate A. Any enhancement of the g factor due to a large orbital moment would artificially increase, not reduce, our estimate for A. In the one spin-blockaded transition in a ^{13}C device that displayed a large g-factor inferred from the shift with magnetic field of the finite triangle base, the width of the peak in leakage current around $B_{||} = 0$ was smaller by the corresponding factor $\mu_{\mathrm{orb}}/2\mu_B \simeq 5$, compared to the data Fig. 4.3.

Considering possibilities that could artificially increase the measured value of A, there is a situation that can arise that leads to a strong suppression of the g-factor in parallel magnetic field. This can occur when $\Delta_{KK'} = (\mu_{\mathrm{orb}}/2\mu_B)\Delta_{\mathrm{SO}}$, where $\Delta_{KK'}$ quantifies the strength of mixing of K and K' points and Δ_{SO} is the spin-orbit splitting [70]. It is doubtful, however, that this could have more than a factor-of-two influence on the measured value of A without precise alignment of the nanotube axis with the applied field. Misalignment for the ^{13}C device in Figs. 4.2 and 4.4c was measured to be $\sim 5^\circ$. This mechanism would also require tuning the ratio of $\Delta_{KK'}$ and Δ_{SO} to within a few percent. Among other things, consistent results in different tubes argues against this mechanism.

Extracting A from B_{nuc} requires knowing of the number of ^{13}C nuclei, which depends on the diameter of the nanotube and the length of the dot. AFM measurements show the average diameter for our growth process to be 2 nm, consistent with orbital moments we measured [69]. We take as the length of our dots the lithographic distance between the centers of the gates used to define the barriers. Coulomb diamonds measured on single dots in these devices reveal a longitudinal level spacing of 5 meV, in good agreement with the expected level spacing of 5.1 meV for the lithographic length of 330 nm ($\Delta E = hv_F/2L$, $v_F \sim 8 \times 10^5$ m/s). Furthermore, the charging energy in this measurement was 8 meV, larger than the 3-6 meV typical of the charge transitions reported in the main text. We therefore rule out dot lengths significantly smaller than the lithographic estimate. A 2 nm nanotube 330 nm in length contains $\sim 7 \times 10^4$ carbon atoms, hence our estimate $N \sim 3\text{–}10 \ \times 10^4$. Reducing the estimate of N (by assuming the effective dot is smaller than its lithographic size or that the fraction of ^{13}C is less than 99%) further increases the estimate of A.

Chapter 5

Relaxation and dephasing in a two-electron carbon nanotube double quantum dot

H. O. H. Churchill[1], F. Kuemmeth[1], J. W. Harlow[1], A. J. Bestwick[1], E. I. Rashba[1,2], K. Flensberg[3], C. H. Stwertka[1,4], T. Taychatanapat[1], S. K. Watson[1,4], and C. M. Marcus[1]

[1]*Department of Physics, Harvard University, Cambridge, Massachusetts 02138*

[2]*Center for Nanoscale Systems, Harvard University*

[3]*Nano-Science Center, Niels Bohr Institute, University of Copenhagen, Universitetsparken 5, DK-2100 Copenhagen, Denmark*

[4]*Department of Physics, Middlebury College, Middlebury, Vermont 05753*

Abstract

We use charge sensing of Pauli blockade (including spin and isospin) in a two-electron ^{13}C nanotube double quantum dot to measure relaxation and dephasing times. The relaxation time, T_1, first decreases with parallel magnetic field then goes through a minimum in a field of 1.4 T. We attribute both results to the spin-orbit-modified electronic spectrum of carbon nanotubes, which at high field enhances relaxation due to bending mode phonons. The inhomogeneous dephasing time, T_2^*, is consistent with previous data on hyperfine coupling strength in ^{13}C nanotubes.

5.1 Introduction

Few-electron double quantum dots have enabled the coherent manipulation and detection of individual and coupled electron spin states required to form qubits [3, 6, 110, 4]. Although recent protocols mitigate decoherence due to hyperfine coupling in GaAs-based devices [148, 149], an attractive alternative is to base spin qubits on group IV elements, which primarily comprise isotopes free of nuclear spins. Progress in this direction includes double quantum dots in Si/SiGe 2DEGs [150], P donors in Si [122], Ge/Si nanowires [108], and carbon nanotubes [20, 22, 23]. Recent advances in nanotube double dots include observation of singlet-triplet physics [25] and Pauli blockade [26]. Developing these systems as spin qubits depends crucially on understanding their modes of relaxation and dephasing.

This Letter reports measurements of relaxation and dephasing times in a two-electron nanotube double quantum dot grown from isotopically enriched (99%) ^{13}C methane. Measurements use fast pulses applied to electrostatic gates combined with charge sensing measurements in the Pauli blockade regime, including spin and isospin quantum states. The relaxation time of these states, T_1, initially decreases with parallel field and has a

minimum in a field of 1.4 T. We interpret these results within the context of the recently observed [70] spin-orbit interaction in carbon nanotubes [72, 84]. We also measure a relatively short two-electron inhomogeneous dephasing time, $T_2^* \sim 3$ ns, which presumably arises from hyperfine coupling. The implied hyperfine coupling strength is consistent with values measured recently by transport [96]. In contrast, the longer $T_1 \sim 1$ μs does not show signatures of hyperfine coupling.

5.2 Device fabrication and demonstration of few-electron double dot

The double dot studied here is based on a single-walled carbon nanotube grown by chemical vapor deposition using 99% $^{13}CH_4$ feedstock [138]*. After deposition of two pairs of Pd contacts [Fig. 5.1(a), red], the device is coated with a 30 nm functionalized Al_2O_3 top-gate oxide using atomic layer deposition [151, 103]. Aluminum top-gates (blue, yellow, and gray) define a double dot between contacts 1 and 2 and a single dot between contacts 3 and 4, capacitively coupled [orange wire in Fig. 5.1(a)] to the double dot to allow charge sensing [129, 108]. The small bandgap ($\sim$ 25 meV) nanotube is operated in the electron regime. Direct current and standard lock-in measurements are carried out in a dilution refrigerator (electron temperature $\sim$ 100 mK).

Electron occupancies $(N_\mathrm{L}, N_\mathrm{R})$ of the double dot are determined from the charge stability diagram (Fig. 5.1b), measured using the conductance, g_s, of the charge-sensing dot [108]. Lever-arm ratios converting gate voltages to dot energies, extracted from nonlinear transport, give a large ($\sim$ 1 meV) interdot capacitive coupling, based on the size and shape of the stability diagram.

* $^{13}CH_4$ of 99% purity from Sigma-Aldrich, Co. 2 nm diameter is estimated from atomic-force microscope measurements of similar growths

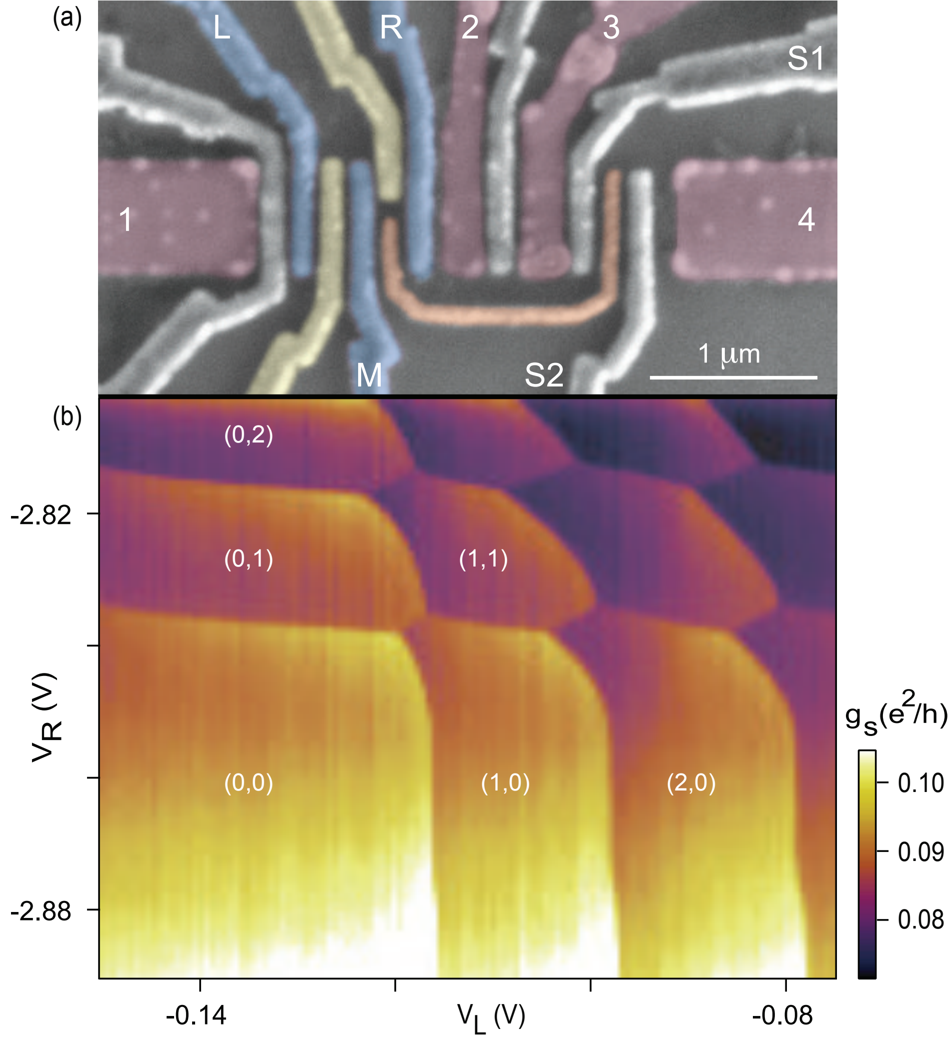

Figure 5.1: (a) False-color SEM micrograph of a device of the same design as the measured device. The ^{13}C nanotube (not visible) runs horizontally under Pd contacts (red). The double dot is defined by top-gates L, R, and M (blue). On the same nanotube, a separate quantum dot is controlled with gates S1 and S2 and capacitively coupled (orange wire) to the double dot to allow charge sensing. Fast pulses are applied to L and R. (b) Charge sensor conductance g_s measured between contacts 3 and 4 as a function of V_L and V_R showing the charge stability diagram, with electron occupancies (N_L, N_R) in each dot.

5.3 Pauli blockade with spin and isospin

Single-electron states of a nanotube quantum dot (in the lowest circumferential mode) can be classified by a quantized longitudinal mode, a real spin ($S = 1/2$), and an isospin, reflecting two valleys K and K' (or, equivalently, clockwise and counterclockwise

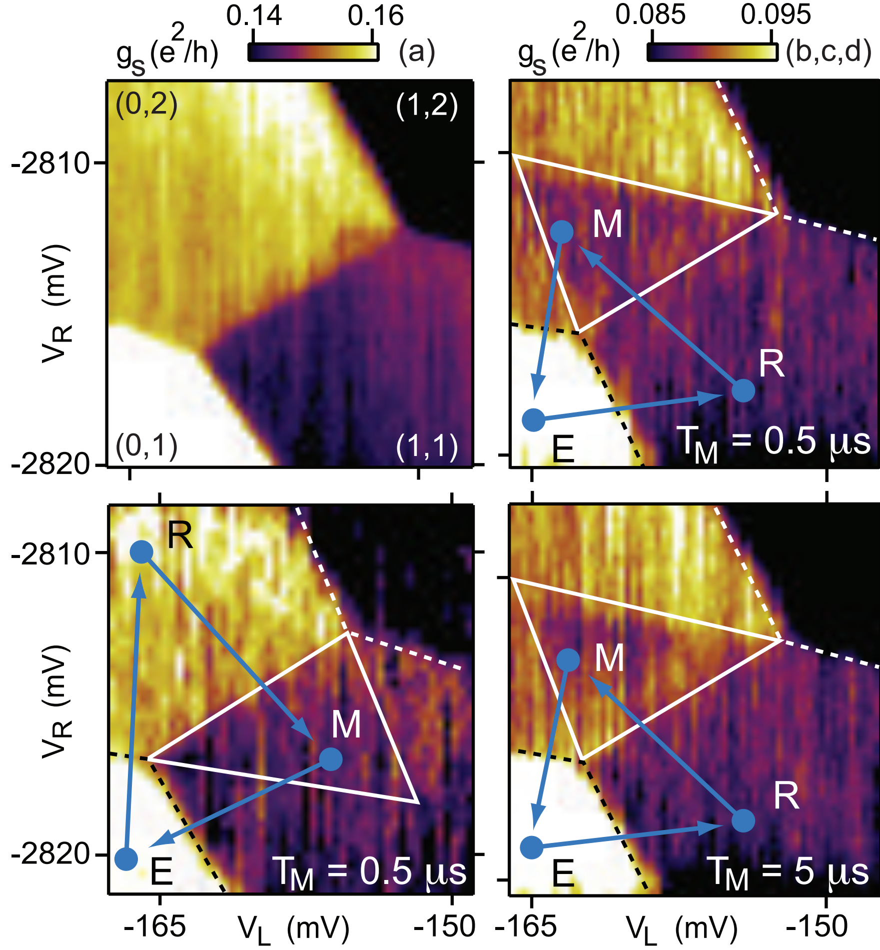

Figure 5.2: Sensor conductance g_s as a function of V_R and V_L around the (1,1)/(0,2) transition (a) without applied pulses, (b) with the T_1 pulse cycle E→R→M→E applied, $\tau_M = 0.5\ \mu s < T_1$. Dashed lines indicate the boundaries of (0,1) and (1,2) during step M. Within the pulse triangle (solid white lines), g_s is between the (1,1) and (0,2) values, indicating partially blocked tunneling from (1,1) to (0,2), (c) with T_1 pulse cycle, $\tau_M = 5\ \mu s > T_1$, and (d) control pulse cycle, with R and M interchanged. $B = 0$ in each panel. Blue arrows are schematic: point E is farther left than shown so that the pulse cycle encloses the (0,1)/(1,1)/(0,2) vertex for all points M within the pulse triangle.

motion around the nanotube circumference) [56]. Including both spin and isospin, there are 16 ways to fill the lowest longitudinal modes with two electrons in the separated (1,1) charge state. There are only six ways, however, to fill the lowest longitudinal mode of (0,2) while maintaining overall antisymmetry of the two-electron wave function.

Under the condition of conserved spin and isospin in the double dot [152], the remaining 10 of the 16 two-electron states of (1,1) may be blocked from tunneling to the lowest mode of (0,2) by selection rules on both spin and isospin. This is a generalization of the Pauli blockade [135] observed in few-electron double dots without valley degeneracy. Previous experiments on Pauli blockade have only considered spin selection rules.

5.4 Relaxation of blocked states

Pauli blockade of the $(1,1) \rightarrow (0,2)$ transition is detected by time-averaged charge sensing, using the cyclic gate-pulse sequence in Fig. 5.2(b) [5]: Starting at E in (0,1), an electron is loaded with random spin and isospin, forming a (1,1) state at point R. Moving to point M (adiabatically on the timescale of interdot tunnel coupling) where the ground state is (0,2) and remaining there for a time τ_{M}, the system may or may not tunnel to (0,2) depending on the state of (1,1). Blocked states would have to tunnel to states involving higher-lying longitudinal modes of (0,2), which are energetically inaccessible at M (they are $\gtrsim$ 1 meV higher [96]); such states must flip either real spin or isospin (or both) to reach an accessible (0,2) state.

With the cycle E→R→M→E running continuously, V_{L} and V_{R} are rastered in the vicintiy of the (1,1)-(0,2) charge transition [Fig. 5.2(b)]. Eighty percent of the pulse period is spent at M (10% each for E and R) so that the time-averaged sensor signal g_{s} primarily reflects the charge state at M. Within the triangle marked by solid white lines in Figs. 5.2c-

d, the time-averaged $\mathrm{g_s}$ lies between values on the (1,1) and (0,2) plateaus, decreasing in visibility as τ_M is increased [Fig. 5.2(c)], with edges of the triangle disappearing faster due to thermal activation [5]. We also observe faster relaxation within 200 μeV of the base. On the contrary, $\mathrm{g_s}$ is independent of the pulse period outside the pulse triangle. A control cycle with R and M interchanged does not show a triangular region in (1,1), indicating that none of the loaded $(0,2)$ states is blocked from tunneling into (1,1) [Fig. 5.2(d)].

5.5 Magnetic field dependence of relaxation

In a magnetic field, B, applied within a few degrees of parallel to the tube axis, forward bias ($V_2 > V_1$) current—the Pauli-blockade direction—shows a dip around $B = 0$ [Fig. 5.3(a)], indicating a reduced spin- and/or isospin-flip rate near zero field. A phenomenological Lorentzian fit (red curve) to the dip has a FWHM of 11 mT. In the reverse-bias case ($V_1 > V_2$), current is independent of B (~ 1 pA) over the same range.

The pulse-triangle visibility, $I = \frac{\mathrm{g_s}(\tau_\mathrm{M}) - \mathrm{g_s}(\infty)}{\mathrm{g_s}(0) - \mathrm{g_s}(\infty)}$ as a function of τ_M, measured in the center of the triangle [Figs. 5.2(b), (c)] at $B = 0,\ 100,$ and 200 mT, is shown in Fig. 5.3(b) along with the relaxation time T_1 extracted from fits to $I(\tau_\mathrm{M}) = \frac{1}{\tau_\mathrm{M}} \int_0^{\tau_\mathrm{M}} e^{-t/T_1}\, dt$ [5]. The relaxation time decreases with increasing B, but with a weaker dependence than the transport data [Fig. 5.3(a)]. We speculate that these trends are due to phonon-mediated relaxation enabled by spin-orbit coupling [70, 84][2], a mechanism that is suppressed at small magnetic fields by Van Vleck cancellation [153].

Characteristics of the single-particle spectrum of the individual dots can be inferred from the B dependence of the addition spectrum, measured for the left dot via charge sensing [Fig. 5.3(c)]. Field dependences of the addition energies for the first four electrons suggest

[2]Results in Ref. [96] required many-electron configurations where these spin-orbit effects are absent or diminished.

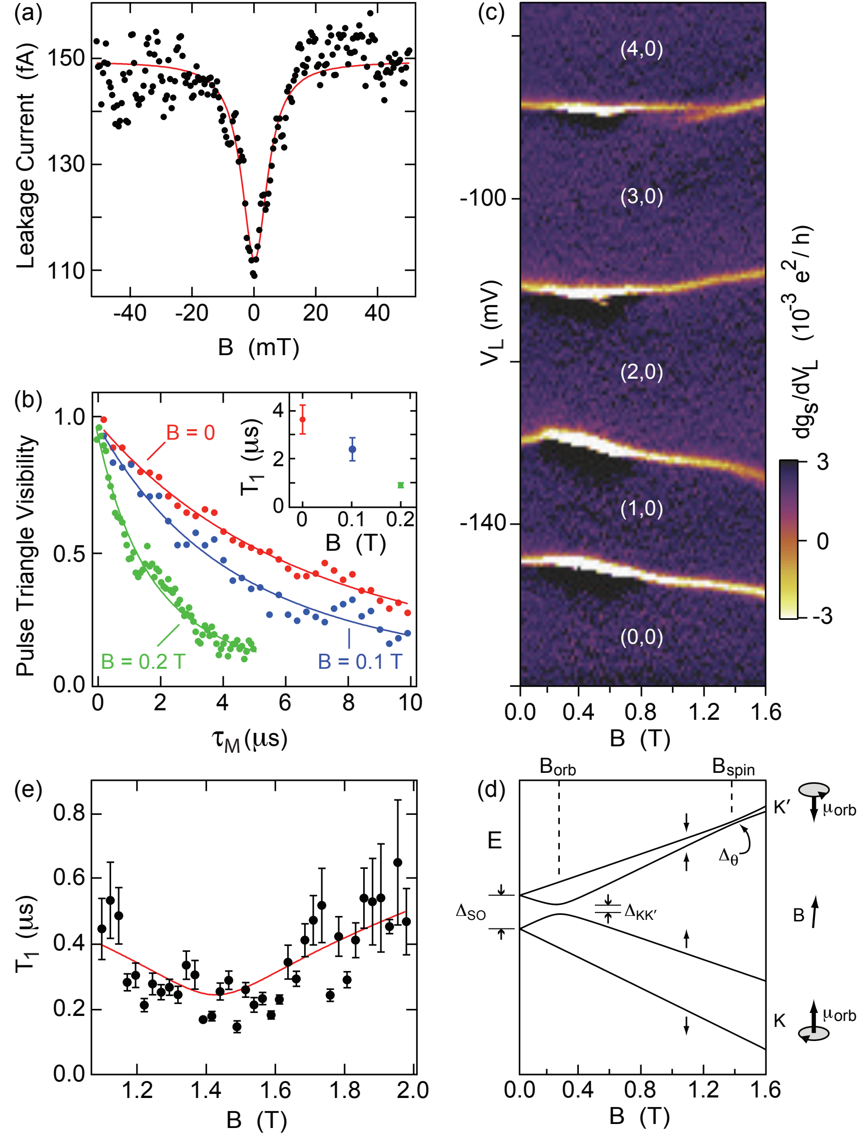

Figure 5.3: (a) Leakage current through blockade near zero detuning for small B, $V_{12} = -2$ mV. (b) Decay of pulse triangle visibility I as a function of τ_M measured in the center of the triangle at several values of B. (c) $\mathrm{dg_s}/\mathrm{d}V_L$ as a function of V_L and B, showing the dependence of ground state energies on B for the first four electrons on the left dot. (d) Energy level diagram of the lowest states of a nanotube with spin-orbit coupling; $\Delta_\mathrm{SO} = 170$ μeV, $\Delta_{\mathrm{KK}'} = 25$ μeV, $\theta = 5^\circ$, and $\mu_\mathrm{orb} = 330$ μeV/T. Arrows indicate spin component parallel to the nanotube axis. Schematics (right) indicate orbital magnetic moment, μ_orb, for clockwise (K) and counterclockwise (K') moving isospin states. At B_orb (B_spin), the orbital (Zeeman) shifts compensate Δ_SO and states with opposite isospin (spin) anti-cross. (e) T_1 extracted as in (b) for B between 1.1 and 2 T. Error bars: standard deviation of the fit parameter T_1. One-parameter fit (red curve) to theory of Ref. [84], modified for B misaligned by 5° (see text).

the spectrum shown in Fig. 5.3(d), consistent with Ref. [70],[3] with spin-orbit coupling playing an important role. We note, in particular, that the energy to add the second electron first increases with B at small B, then decreases at higher field. This indicates that the second electron first occupies a counterclockwise (K') isospin state at small B, then changes to a clockwise (K) isospin at $B \sim 250$ mT. The energy to add the third electron does the opposite. Fits to the low field slopes for the second and third electron addition energies yield moments of 390 μeV/T and -270 μeV/T, respectively, with a difference in magnitudes within 10% of $2\mu_B$, a signature of a spin-orbit dominated spectrum [70]. Thus we infer an orbital moment $\mu_{\rm orb} = 330$ μeV/T and a zero-field spin-orbit splitting $\Delta_{\rm SO} = 170$ μeV.

A consequence of the spectrum in Fig. 5.3(d) is a predicted [84] minimum in T_1 as the two K' states with opposite spin approach one another at $B_{\rm spin} = \Delta_{\rm SO}/g\mu_B$, which for this nanotube occurs at 1.4 T [cf. Fig. 5.3(d)]. The expected coupling of these two states is via 1D bending-mode phonons with quadratic dispersion, leading to a $T_1 \propto \sqrt{\Delta}$ dependence on the energy splitting Δ due to the density-of-states singularity at zero energy in 1D [84]. This is in contrast to higher dimensions, where T_1 diverges as $\Delta \to 0$ [84, 153, 154]. A discussion of relaxation at this point in light of more recent theory [95] is described in §5.8.

Values for T_1, extracted from fits as in Fig. 5.3(b), are shown in Fig. 5.3(e), where a minimum in T_1 is observed at the predicted value, $B \sim 1.4$ T. Also shown in Fig. 5.3(e) is a fit of the form $T_1 = C\sqrt{\Delta_\theta}$, where the splitting

$$\Delta_\theta = g\mu_B\sqrt{(B\cos\theta - \Delta_{SO}/g\mu_B)^2 + (B\sin\theta)^2}$$

is anti-crossed, accounting for a misalignment angle, θ, between the nanotube axis and the

[3]Reference [84] infers the sign of the spin-orbit interaction from Ref. [72]. It is opposite to the sign found experimentally in Ref. [70] and here. As a result, the two lower, not upper, levels of our Fig. 5.3(d) cross in Ref. [84].

direction of the applied field.[4] For these fits, we use $g = 2$ and the measured quantities Δ_{SO} and θ (5° determined by the electron micrograph); the only free parameter is an overall scale for T_1, $C = 65$ ns/$\sqrt{\mu\text{eV}}$, only a factor of ~ 5 smaller than the estimates in Ref. [84]. Attributing the measured T_1 minimum to this mechanism requires loading a two-electron state involving at least one of the two higher states of Fig. 5.3(d) at step R, which is expected because the levels of the left dot are well below the electrochemical potential of the left lead at R. We note that hyperfine relaxation should also be strongest near a degeneracy [5], but the ratio $\Delta_\theta/(g\mu_B B_{\text{nuc}}) \sim 20$ (Ref. [96]) would require huge inelastic tunnel rates ruled out by transport measurements to explain the measured T_1.

5.6 Dephasing

We do not observe signatures of hyperfine-mediated relaxation near $B = 0$,[5] but note that a difference in effective magnetic fields between the two dots should induce dephasing of prepared two-particle spin and isospin states. To measure the inhomogeneous dephasing time T_2^* of a state at $B = 0$, a pulse cycle [Fig. 5.4(a)] first prepares an (0,2) state at P, then separates the electrons via P′ into (1,1) at S for a time τ_s, and finally measures the return probability to (0,2) at M [6]. For small τ_s, the prepared state always returns to (0,2). For $\tau_\text{s} \gtrsim T_2^*$, a fraction of prepared states evolves into blocked states, reducing the return probability within the pulse triangle [Fig. 5.4(a)].

The dephasing time is obtained from the value of g_s in the center of the pulse triangle versus τ_s, which reflects the probability of return to (0,2) when calibrated against the equilibrium (1,1) and (0,2) values of g_s [Fig. 5.4(b)]. A likely source of dephasing is the hyperfine interaction. Assuming a difference in Overhauser fields acting on the two

[4] This form is exact only for $\Delta_{KK'} = 0$ but is justified because orbital mixing is suppressed by large B.

[5] Hyperfine-mediated relaxation would reduce T_1 and increase leakage current near $B = 0$.

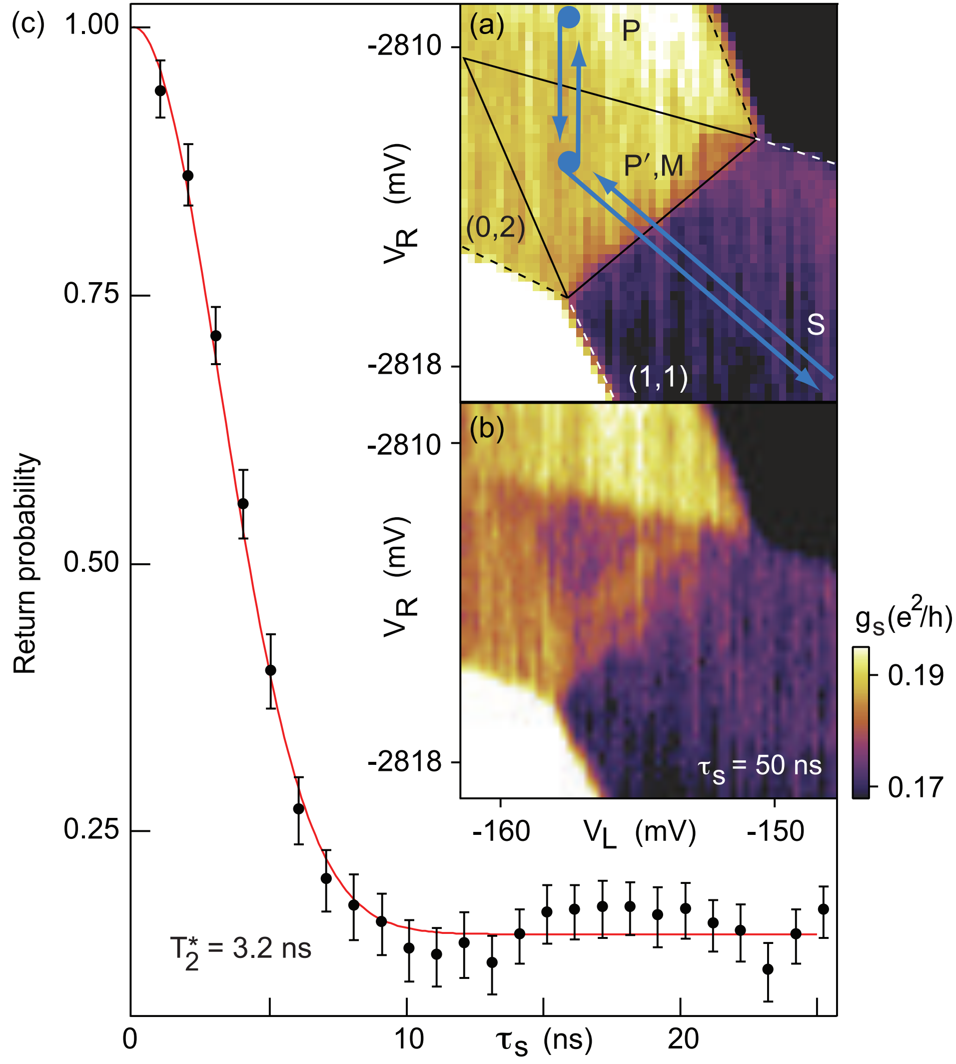

Figure 5.4: (a) Pulse sequence to measure the dephasing time T_2^* (see text). If a state prepared at P dephases into a Pauli-blocked state while separated at S for a time τ_s, g_s is reduced within the pulse triangle outlined in black (shown in (b) for $\tau_P = \tau_{P'} = 100$ ns, $\tau_S = 50$ ns and $\tau_M = 2$ μs at $B = 0$). (c) g_s calibrated to reflect the return probability to (0,2) versus τ_s. A Gaussian fit (red) [155] gives $T_2^* = 3.2$ ns and $\delta B_{nuc}^{||} = 1.8$ mT. The data points are an average of 500 individual traces; error bars are the standard error.

electrons of root mean square strength $\delta B_{\rm nuc}^{||}$ parallel to the nanotube axis [149, 155], the decay is fit to a Gaussian form, giving $T_2^* = \hbar/g\mu_B \delta B_{\rm nuc}^{||} = 3.2$ ns. The corresponding $\delta B_{\rm nuc}^{||} = 1.8$ mT is a factor of two smaller than our estimate of the single dot nuclear field $B_{\rm nuc}$ in ^{13}C nanotubes.[6] The difference may be due to anisotropic dipolar hyperfine coupling [97] or to accidental suppression of $\delta B_{\rm nuc}^{||}$ [149]. Future work on ^{12}C nanotubes will allow dephasing mechanisms other than the hyperfine interaction to be investigated.

Finally, we note that the saturation value of the return probability in Fig. 5.4(c) is 0.17, smaller than the value of 1/3 for singlet-triplet dephasing at $B = 0$ in GaAs [6, 156], likely due to the richer spectrum allowed by isospin. Similarly, the tunneling probability from (1,1) to (0,2) (inferred from the visibility of the T_1 pulse triangle for $\tau_{\rm M} = 0.5$ μs $< T_1$, Fig. 5.2b) is ~ 0.15, lower than the 0.375 expected from state-counting arguments (6 unblocked states out of 16 total) combined with adiabatic passage. This issue requires further study.

5.7 Summary

In summary, we have measured relaxation and dephasing in a two-electron ^{13}C nanotube double quantum dot. We identify signatures of spin-orbit coupling in the magnetic field dependence of both the addition spectrum and the relaxation time T_1, and we observed a dephasing time T_2^* consistent with recent measurements of the hyperfine coupling strength in ^{13}C nanotubes. The short dephasing time motivates development of nanotube devices with less than the 1% natural abundance of ^{13}C.

[6] These data are for the device in [96] with $B_{\rm nuc} = 4$ mT.

Acknowledgements

We thank C. Barthel, E. A. Laird, and D. J. Reilly for technical assistance. This work was supported by the National Science Foundation under grant no. NIRT 0210736, ARO/iARPA, the Department of Defense, and Harvard's Center for Nanoscale Systems. H.O.H.C. acknowledges support from the NSF.

5.8 Epilogue

At the time this work was published, we compared our T_1 data with the only available theory for relaxation near the high-field anti-crossing B_{spin}, which was that of Bulaev and Loss who described coupling to the nanotube bending mode deformation potential [84]. Subsequent work by Rudner and Rashba considered a different relaxation mechanism in which the locking of the spin direction along the nanotube axis by spin-orbit coupling causes spin relaxation as the deflections of nanotube axis tilt the spin up and down in an external field [95]. The deformation potential mechanism predicts an enhancement of the relaxation rate in the high-temperature limit (compared to the splitting of spin states Δ_θ), but a suppression in the low-temperature limit. The experiment described in this chapter is in the intermediate regime with $\Delta_\theta \sim k_B T$ so the applicability of this mechanism is ambiguous. The deflection coupling mechanism predicts enhanced relaxation at small splittings for all temperatures and is moreoever expected to be stronger by a factor $1/\Delta_\theta$ than the deformation potential mechanism [95].

One open question from these experiments is the low saturation value of the return probability (~1/6) in the dephasing experiment. Reynoso and Flensberg studied this question in detail in both the clean limit ($\Delta_{KK'} = 0$) [107] and the disordered case in which different valley couplings in each dot lead to mixing between as well as within Kramers

doublets [106]. In both situations the minimum return probability predicted is 1/3 at zero field, just like the case without the additional valley degree of freedom. If an excited state of (0,2) is prepared in the disordered case, a return probability of 1/6 is possible, but it is combined with an initial $\tau_S = 0$ return probability of 1/2 which is incompatible with the available data. The original conclusion regarding the low return probability stands: this issue requires further study.

Chapter 6

Conclusions and Outlook

The preceding chapters have described experiments on similar device structures built on top of two quite different one-dimensional semiconductors, Ge/Si nanowires and carbon nanotubes. In terms of spin qubit applications, the state of the art is quite similar for the two systems: it is possible to define and control double quantum dots [108, 20, 22, 23, 27], observe spin blockade, and measure spin lifetimes [157, 96, 94]. The prospect of extended coherence through diluted nuclear spins has not been confirmed, and qubit manipulations have not been demonstrated.

Ge/Si core/shell nanowires seem to have a promising future. These nanowires would be like many other semiconductors material except that the valence band offset between the Ge core and Si shell is such that a hole gas accumulates in the core. This fact, combined with the protection afforded by the Si shell and the possibility of depletion of isotopes with nuclear spin, creates a high-quality system with unique properties. In particular, the valence band of Ge/Si nanowires has been predicted to support an unusually strong spin-orbit interaction that may make these wires particularly well-suited for spin-orbit qubits [14]. Even without isotopic purification, these nanowires should also have a

reduced hyperfine interaction because the p-orbitals occupied by the holes have no contact hyperfine interaction, ignoring s-admixutre. However, valence bands have a reputation for low mobilities and heavy masses, and Ge/Si nanowires may be no different. The mobility of these wires was quite low (<1000 $\text{cm}^2/\text{V}\cdot\text{s}$) in some cases [158, 159], but in others a mean free path >500 nm was estimated [113], which is more than sufficient for quantum dot experiments. The large mass (0.28 m_e for heavy holes in Ge) means that devices with appreciable level spacing must be made very small, but it seems this size is not out of reach [157]. Future high-quality bottom-gated devices made with Ge/Si nanowires will show whether the material is good enough for its potential in spintronics to be realized.

The outlook for carbon nanotube qubits is more complicated and depends on one's interests. Some nanotubes host quantum dots that are controllable and stable and beautiful in all the ways a quantum dot can be. Their electronic structure provides a physical richness that will surely continue to inspire detailed study of basic questions and novel phenomena. But most nanotube quantum dots are, unfortunately, worth their weight in gold[1] which poses a serious problem for quantum information applications. The situation is that 'carbon nanotube' does not describe a single material, but a class of materials with widely varying properties depending on chirality. Nearly every application of carbon nanotubes is plagued by a chirality problem, and quantum dots are no different.

Two characteristic energy scales of importance to quantum dot spintronics are the band gap and spin-orbit coupling. Excluding graphene and some zero-gap II-VI materials, common semiconductor materials have band gaps that vary by about a factor of 50 from $\sim$ 0.1 eV (InAsSb) to 5 or 6 eV (diamond, AlN). The range for nanotubes is from a few meV to about 1 eV, a factor of more than 100. Considering spin-orbit coupling, silicon has a relatively small atomic spin-orbit coupling of 44 meV, while Pb has a spin-orbit gap (2

[1]For a typical 200 nm dot, that's 50 attodollars at current prices.

eV) that is larger by a factor 50 [160]. In carbon nanotubes (restricting the diameter range between 1 and 2 nm), the spin-orbit strength is predicted to vary from 20 μeV (2 nm zigzag, electrons) to 1 meV (1 nm zigzag, holes), also a factor of 50 [77]. Focusing on these two energy scales, carbon nanotubes of different chiralities exhibit relative variations on a scale encompassed by nearly all other semiconductor materials combined.

Currently available methods to select particular chiralities by growth, purification, or characterization are either not compatible with high-quality quantum dot fabrication or prohibitively time consuming, so in the work presented here, we selected band gaps of approximately the desired size using room temperature and 4 K transport measurements. However, nanotubes with nearly identical band gaps can have dramatically different electronic structures through the chirality dependence of the spin-orbit coupling. For few qubit studies, this chirality problem is not so severe, but their impact on scaling seems catastrophic.

The redeeming quality of carbon nanotubes is that the highest quality, as-grown devices are also the easiest to make. As described in Appendix B for example, a fabrication run consisting of two ebeam steps, three photo steps, and two CVD runs over two or three days (with lucky scheduling) can produce about 1000 potential devices, with successful single nanotube contact 5-10% of the time. One can then imagine developing a combination optical spectroscopy and nanomanipulation protocol that overcomes the chirality problem. Deciding to pursue such a program would require an advantage of nanotube qubits over other materials and qubit implementations. Despite the efforts presented in this thesis, the existence of such an advantage remains undetermined.

Appendix A

Top-gated carbon nanotube double dot devices

This appendix describes the fabrication of top-gated carbon nanotube quantum dot devices in which nanotube growth occurs near the beginning of the process, and leads, gate insulator, and topgates are fabricated on top of the nanotube. All of this processing after growth results in devices with significantly more long-range disorder than those in which nanotube growth occurs at the end; nevertheless, the version of these devices fabricated with the Jeol JSM-7000F ebeam writer (rather than Elionix ELS-7000) are the ones described in Ch. 3 and 4. A very similar process was used by Jie Xiang and Yongjie Hu to fabricate the Ge/Si nanowire device described in Ch. 2, with nanowire deposition substituted for nanotube growth. The first section of this appendix describes fabrication of that first generation of devices, and the second section describes various attempts to reduce the long-range disorder that made controllable formation and tuning difficult for top-gated nanotube quantum dots. A lot of the procedures in §A.1 are not optimized, but they were what we used to create devices that were successful at the time. Where the potential for misinformation

or wasted time is unbearable, I will describe improvements.

A.1 First-generation top-gated devices

Here is a summary of the steps required to fabricate these devices:

- prepare substrates, write alignment marks
- pattern and deposit iron catalyst pads, grow nanotubes
- locate nanotubes with SEM
- pattern and deposit Pd contacts
- deposit NO_2 functionalized Al_2O_3 topgate insulator
- pattern and deposit top-gates

A micrograph of a finished device is shown in Fig. 4.1(a) and 5.1(a) (same pig, different lipstick).

A.1.1 Wafer selection

The best wafers to use for these back-gated devices with charge sensors are degenerately doped silicon (we always used wafers with resistivities < 0.005 ohm·cm) with 0.5-1 μm of chlorinated, dry thermal oxide with forming gas anneal. Dry thermal oxide is higher quality than wet, but is also much slower to grow so most vendors will not want to provide more than 300 nm of dry oxide. We have had luck in the past with Nova Electronic Materials, Inc. A more flexible option is to buy bare silicon wafers from anywhere and send them to Rogue Valley Microdevices for oxide, or oxidize them in-house in the furnace at CNS. The CNS furnace seems to produce high-quality oxide based on one batch of as-grown nanotube devices.

The wafers' orientation should be [100] for easy cleaving into squares and single-side polished to avoid confusion when chips are inevitably dropped. Diameter is irrelevant, but thicker wafers are much easier to grab firmly with tweezers. Too thick and they are more difficult to cleave. The sweet-spot is 525 μm in my opinion, standard for 4" wafers.

A.1.2 Prepare blank substrates and write alignment marks

Cleave a piece of silicon (5×5 mm for the Jeol and a bigger piece $\sim$ 1×2 inches for the Elionix). Sonicate for at least 4 minutes each in cups of trichloroethylene (TCE), acetone, and isopropanol (IPA); blow dry, thoroughly, with N_2 at the end. This will be referred to as the 'standard clean' below. This is the first step of a 'real' standard clean, RCA SC-1. A useful trick is to squeeze the acetone squirt bottle as you screw the top back on so it doesn't spray once it's closed. Another useful technique when a chip is stuck to something (such as carbon tape after evaporation): don't grab both sides of the chip with the tweezers and twist to remove it, push from one side until it's loose. You're much more likely to scratch the surface by twisting. Check with an optical microscope (in darkfield mode if you really want to find out how dirty it is) for inadequately dried IPA and debris, including flakes of silicon from cleaving. Repeat three solvent sonication until the surface is clean. Small particles are not usually important to the device since it is small, but particles cast shadows during resist spinning that create streaks of thickness variations which may affect lift-off.

Bake 4 minutes on hot plate, 170 C. Meanwhile, check the vacuum of the spinner– turn the vacuum on, place your finger over the hole, and the hissing should stop. Spin on Microchem PMMA 950K A4: static dispense, 45 seconds at 4000 rpm. Bake PMMA on hot plate, 10 minutes at 170C (this is overkill, but that was the recipe). Write alignment marks. Develop PMMA in 1:3 MIBK:IPA for 1 minute, rinse in IPA for 15 seconds, blow dry

thoroughly with N_2. De-scum for 1 minute in the cleanroom UV-ozone box (Samco UV-1). Make sure the sample area is not hot–if it is, wait for the temperature to get below 50 C. Also make sure the O_2 flow is 1 slm. Inspect the pattern in an optical microscope–skipping this step is one of the best ways to ruin a chip.

Deposit metal: 5/50 nm Ti/Pt by ebeam evaporation (I now recommend Cr anything that goes in a CVD furnace because Ti reacts with Si). Platinum is used so the markers hold their shape during nanotube growth at 900 C. Ebeam evaporation is required for Pt; with thermal it is nearly impossible. Lift-off: Soak in acetone for several hours (or if you're in a hurry, sonicate after the first hour, then set it on the hot plate at 65 C for another hour and sonicate again). Sonicate a couple of times, 1 second each. Put the chip in a wafer tray filled with acetone and inspect lift-off progress in an optical microscope. You may have to do syringe blasts with acetone to help lift-off. There are four levels of aggression to use as needed during lift-off: spray with acetone bottle, blast with syringe, sonicate in a teflon cup, and when all else fails, sonicate in a glass beaker. Keep inspecting, rinsing with acetone, and sonicating until lift-off is complete (if the ebeam dose is good, the alignment marks should never peel off due to excessive sonication in a plastic cup). Soak in IPA for 5 minutes and dry with N_2. If you were working with a large piece with several dice on it, chop it up using a scriber or the cleanroom cleaver.

A.1.3 Catalyst Pads

Clean chips in cleanroom and spin on PMMA (950K C2, bake 5 or more minutes). Pattern catalyst pads (with Elionix: 100 pA, 150 um, 20K dots, 8 μs. 1 nA and 0.8 μs and photolithography work just as well.) Develop PMMA, 90 seconds in 1:3 MIBK:IPA, rinse in IPA, then 1 minute UV-ozone. Evaporate Fe in Sharon TE-4–four hour reservation is enough pumping (should be low 1e-7 mbar range). The standard thickness is 5.0 nm, but

this thickness can be tuned to iron out variations in nanotube yield: *less* Fe results in *more* nanotubes (down to 1 nm at least). Evaporate at a rate of 1 Å/s, and increase the power slowly enough that the pressure during evaporation is in the 10-7 mbar range. Liftoff: 1 hr. soak in acetone; a couple of blasts with acetone using syringe. Do not sonicate because little iron chunks will land everywhere. Soak for 5 minutes in IPA and dry with N_2. Inspect catalyst pads using microscope, which are barely visible at a thickness of 5 nm.

A.1.4 Nanotube Growth

The Marcus Lab nanotube growth recipe when I joined the lab consisted of growth with CH_4 feedstock, iron thin film catalyst deposited on the device chip, and some additional silicon pieces with IPA-diluted iron nitrate catalyst that were placed downstream from the device chip and reused from run to run. Nanotube growth was carried out in a Lindberg Mini-mite furnace, with the chip in a quartz boat inside a one-inch diameter quartz tube, four MKS 2179A mass-flow controllers (Ar, H_2, CH_4, and $^{12/13}CH_4$), and an MKS 613 mutli-gas controller. Several developments during my time included:

- elimination of the additional catalyst chips (they were unnecessary)
- switching from evaporated iron catalyst to alumina-supported iron nitrate and molybdenum acetate catalyst (iron nitrate catalyst is easier to apply and has higher, more consistent yield compared to evaporated iron catalyst)[1]
- placing the chip on a large piece of silicon rather than a quartz boat (the idea was to encourage laminar flow for flow-aligned growth, which did not succeed; our nanotubes

[1] The recipe is from Kong *et al.* [161]: 0.05 mmol (20.2 mg) $Fe(NO_3)_3 \cdot 9H_2O$ (stays in dry box, should be clear, not yellow), 0.015 mmol (4.89 mg) $MoO_2(acac)_2$, 15 mg Al_2O_3 nanoparticles, 15 mL H_2O, IPA, or methanol (I prefer water). Stir for a long time (> 3 hours), sonicate for 1 hour, should be deep orange or red. Develop pattern, squirt on catalyst, blow off with N_2, spray chip with acetone bottle, soak in acetone 5 minutes (don't spray into this bottle in the previous step), rinse in IPA, grow nanotubes (not necessary immediately).

are not long enough), which is more convenient for samples that just fit inside the tube.

Ruby Lai put considerable effort into developing a non-magnetic catalyst recipe using rhodium chloride; the yield was decent, but not quite high enough for the as-grown devices we were making at the time.

Table A.1: Original nanotube furnace bakeout recipe.

Temperature (C)	Gas (slm)	Time (min)
25	5 Ar	5
25 → 800	0.8 Ar, 0.1 H_2	15
800[1]	0.8 Ar, 0.1 H_2	90
800 → 25	0.8 Ar	10

Bake the furnace before growing nanotubes, unless a growth or bake has been done in the last day or two. Do not put the extra catalyst chips upstream of growth chip–this leads to short, curly nanotube often in annoying abundance. Orient the chips as in the pictures in the log book from previous runs.[2]

Table A.2: Nanotube growth recipe.

Temperature (C)	Gas (slm)	Time (min)
25	5 Ar	5
25 → 900	0.8 Ar, 0.1 H_2	30
900	1.5 CH_4, 0.1 H_2	15
900 → 25	0.8 Ar	10

When cooling down, the top of the oven can be opened below 600 C. Turn the fan on to further speed things up, and remove the sample below 100 C. Make sure to return

[1]The current recipe is identical except that the baking temperature is increased to 900 C.

[2]The chips were oriented so that the big alignment mark downstream from the device area because it often produces a lot of extra nanotubes, but we never had directed growth that would have made such a precaution necessary.

the boat to the center of the quartz tube and turn off the gases.

A.1.5 Locate nanotubes with SEM

When I joined the project, nanotubes were located by AFM. This time consuming process was the primary bottleneck for nanotube device fabrication, so we began to locate nanotubes using SEM. The advantage of AFM is that it is harmless to the nanotubes and provides a measure of the nanotube diameter. SEM has the potentially harmful effect of contaminating the nanotubes with hydrocarbon scum, but we deemed the speed advantage to be worth the risk. The loss of diameter information can be compensated somewhat by doing AFM scans of many devices under identical growth conditions (temperature and catalyst, for example), then switching to SEM once a statistically significant average diameter is known. We did this after switching to $FeNO_3$ catalyst, for example. As will be described in Appendix B, SEM imaging was not the limiting source of disorder in our devices.

To get a good image, use the In-Lens detector, 0.7-2 kV, maximum working distance (about 4 mm). To minimize contamination, minimize the amount of time spent zoomed in on the nanotubes. Therefore, focus, stigmate, and optimize contrast/brightness on the big alignment mark near the device area, then take one image that contains all four corner alignment marks. Use an image size of 2048×1536, with frame averaging turned on to get a sense of stage drift (drift will causing the image to get more blurry rather than cleaner, and should not be noticeable). Rotate and skew the image in Photoshop, load the image into DesignCAD, and align the pattern in DesignCAD with the image. The alignment accuracy using this method is about 100 nm ($\sim$ 2 pixles) with the 150 μm scan sizes we used. In other words, we used contact widths of 500 nm and successfully hit the nanotubes nearly every time. More details can be found on the Marcus Lab Wiki under "NPGS Design Notes for Nanotubes". When selecting nanotubes for devices, we picked

long, straight nanotubes with straight taking precedence over long.

A.1.6 Contacting nanotubes

Prepare chips with the standard clean (no sonication now, though nanotubes that are stuck to a substrate will not move under sonication) and PMMA preparation (C2, bake at least 8 min). The recipe for the Elionix ELS-7000 is 100 pA, 150 μm chip size, 20k dots, 15 μs dwell time for small features. This dose is for a cold develop (see §A.2.1) in which the MIBK beaker sits in an ice water bath for 20 minutes prior to developing: 90 seconds in 1:3 MIBK:IPA, then 1 minute UV-ozone. By slowing down the reaction of the developer with the exposed resist, this cold develop process increases the contrast between exposed and unexposed regions, resulting in finer features and a larger process window for clean lift-off at the expense of 2-3 times longer writing [162].

Deposit 15 nm of Pd using ebeam evaporation (EE-3 at CNS). Compared to thermal evaporation which we used in the beginning, the deposition rate is much easier to control, the base pressure regularly gets into the mid-8s, and the films lack the so-called 'Pd disease' (little Pd flecks scattered around the edges of features). Most importantly, on switching from thermal to ebeam, our average room temperature conductances went up by 50% after switching from thermal to ebeam. The deposition rate should be 3.5 Å/s (high rates are apparently better for Pd). Deposit only 15 nm–thicker layers do not stick well. The recipe for the devices described in Ch. 3 and 4 calls for no sticking layer, but we later found that 1 nm Ti layer is sufficient for films up to 50 nm thick (the thickest we tried), with no effect on average conductances (hundreds devices were made to back up that assertion).

A.1.7 Room temperature characterization

Once the nanotubes have been contacted, they can be probed at room temperature to estimate the band gap and contact transparency. It is notoriously difficult to predict the characteristics of a nanotube at low temperature based on room temperature back-gate sweeps. However, for few-electron quantum dots, the best ones are small band gap metallic nanotubes with maximum conductances around 0.2-0.5 e^2/h at room temperature. For large band gap nanotubes, the conductance must be higher ($> 1e^2/h$) to have reasonable current through the device near the band gap. Characteristic back-gate sweeps are shown in Fig. 2.3. Figure 2.3(a) is about as good as it gets for a large-gap nanotube, but the conductance of the small-gap nanotube in Fig. 2.3(b) is too high to have a weakly coupled double dot with a total device length less than one micron.

A.1.8 ALD gate insulator

The next step is to deposit a top gate insulator. Here is a brief description of how the addition of a high-κ gate dielectric affects metal contacts to carbon nanotubes. Palladium creates excellent p-type contact to nanotubes because of its very high work function. When a high-κ dielectric material such as Al_2O_3 or HfO_2 covers the device, interface states are formed between the dielectric and the metal/nanotube [163]. This interface dipole model provides an interpolation between the Schottky model of metal-semiconductor contacts in which the barrier height is determined soley by work functions, and the Bardeen model in which the barrier is independent of work function and completely dominated by interface states. As described in Ref. [163], the effect of these interface states is to shift high work functions down and low work functions up toward intermediate values so that a metal that makes decent ambipolar contact to a small-gap nanotube will stay that way, but a metal such as Pd that makes excellent p-type and terrible n-type contact will

make moderately good p-type and noticeably better n-type contact after the application of the dielectric. The higher the dielectric constant of the insulator is, the stronger this effect becomes, so maintaining excellent contacts with HfO_2 ($\kappa \sim 20$) covered devices is more difficult than with Al_2O_3 ($\kappa \sim 8$) covered devices. This interface dipole model agrees fairly well with our observations of the behavior of devices before and after application of gate insulators.

To minimize these effects, we used atomic layer deposition (ALD) Al_2O_3 with a non-covalent NO_2 functionalization layer developed by Damon Farmer in the Gordon group[103] and adapted for our reactor by Jimmy Williams. The idea behind the NO_2 layer was to eliminate the conductance changes and doping associated with deposition of Al_2O_3 directly on nanotubes, which is indeed what happens if the NO_2 dose is just right. In practice it is quite difficult to achieve the desired result in terms of doping, but we made a lot of devices, and some of them came out well with the middle of the band gap near zero volts on the back gate.

The Marcus Lab's Cambridge Nanotech Savannah 100 ALD reactor was upgraded in 2009 with new valves and plumbing (described in A.14, so the recipe described here would need to be modified, primarily by reducing the pulse times to account for the change from Parker to Swagelok valves.

NO_2 deposition is done at room temperature ($\sim$ 30 C), while the oxide deposition is done at 120 C, so the first step is to cool down the sample space. This is done by setting the temperatures of the sample area and wall (heaters 9 and 8, respectively) to 0 C and placing a fan blowing directly at the system. Without the fan the minimum temperature is about 45 C.

Clearing the precursor lines

Make sure the precursor, water, and all NO_2 valves are closed. Run the following clearing recipe to make sure lines are cleared from last run; that is, until the pressure doesn't spike when pulsing. This condition could only be met after many cycles and was one of the primary motivations for the upgrade. The reason for this complicated clearing procedure is that the H_2O and NO_2 precursor line were connected by a tee and shared the same pulse valve in the original setup.

Table A.3: NO_2 and precursor clearing recipe

Precursor	Pulse (s)	Pump (s)
H_2O/NO_2	1	5
TMA	0.1	5

Open NO_2 line up to the regulator valve (keep that closed). Run 20 cycles or so of the clearing recipe (or until pressure doesn't spike anymore) and close the NO_2 line.

Now load the sample: close stop valve (vent), change the N_2 flow to 100 sccm. When pressure reaches 1 atm, you can open the lid. It tends to stick, so don't be shy about pulling hard, but a sticky lid plus lower than usual maximum pressure after venting are signs that the stop valve is leaking and should be replaced. Place the sample in the center of the chamber, change flow back to 20, open stop valve, wait for pressure to stabilize.

Functionalization layer depostion

Make sure temperature is around 30-35 C with the fan flowing on the system. Open all valves on the NO_2 line and the TMA precursor valve. Run the following recipe for the desired number of cycles (we used between 5 and 50, settling with 5 in the end):

The long pumping time after the TMA pulse is required for unreacted precursor to fully desorb at the low temperature of this process.

Table A.4: NO_2 functionalization recipe

Precursor	Pulse (s)	Pump (s)
H_2O/NO_2	0.5	7
TMA	0.1	120

NO_2 pulses should be 30-100 torr. If they're smaller than that, consider increasing the regulator pressure or the temperature of the NO_2 bottle. On the last cycle, press abort right after the TMA pulse to prevent the system from pumping out for 2 minutes (you want to get the intermediate deposition done ASAP and it will take more than 2 minutes to get it going).

Low-temperature alumina capping layer deposition

The NO_2 layer must be locked in place to prevent desorption upon heating to > 100 C for the primary Al_2O_3 deposition. Close the TMA precursor valve and all NO_2 valves. To get rid of any NO_2 left in the lines, run 5 cycles of the cleaning recipe (same as above). Open the TMA precursor valve and water valve. With the temperature still at 30 C, do 5 cycles of the regular alumina deposition:

Table A.5: Low-temperature alumina capping layer recipe

Precursor	Pulse (s)	Pump (s)
H_2O	0.1	5
TMA	0.1	5

Thick alumina deposition

Heat up the sample area and chamber wall to the desired oxide deposition temperature (120 C and 110 C, respectively, in the final recipe for these devices). This takes about 10 minutes. Aluminum oxide deposition using the TMA precursor should deposit

about 1.1 Å/cycle. If you get more, you're not waiting long enough between cycles; if you get less, increase the dose. Deposit the desired alumina thickness using the same recipe as for the capping layer.

When the deposition is finished, remove your sample, pump the chamber down, close all precursor valves, and run the clearing recipe again to clean out the lines.

A.1.9 Top-gates

The final step is to pattern top gates. Do the standard clean (no sonication) and spin PMMA (C2, bake at least 12 min). The devices in Ch. 3 and 4 were written with the Jeol JSM-7000, using a 20 pA beam current and 30 nm thick Al gates. The Al was deposited by thermal evaporation, with an alumina-coated tungsten boat (Al causes bare W boats to crack). For devices of the same design written with the Elionix ELS-7000 the parameters for small features are 20 pA/150 μm chip size/240K dots/20 μs for single pixel lines (sensor couplers), and 150 μm/20K dots/49 μs for polygons). As with contacts, the top-gate pattern should be cold developed: 1 minute in 1:3 MIBK:IPA, rinse 15 seconds in IPA, 60 seconds UV-ozone.

With the 100 kV Elionix machine, lines could be made smaller, so we began using films of 2/18 nm Ti/AuPd for top gates. AuPd was supposed to have a smaller grain size than plain Au, but I didn't notice a difference. These films were thermally evaporated at 1.5 Å/s for Ti and 2.5 Å/s for AuPd. Some say AuPd is sticky by itself, but we found the Ti to be necessary for tiny features. Like Al, AuPd was also evaporated in an alumina coated tungsten boat. We let lift-off go a very long time for these top gate patterns–six hours or overnight–for both Al and AuPd gates. Single-pass lines for sensor couplers could be destroyed by sonication in a plastic cup, but rarely with even the most aggressive syringe blasts.

A.2 Devices designed to reduce long-range disorder

In response to the difficulty of reaching the few-electron regime with the devices described in the previous section, we developed a number of device designs intended to reduce the effects of long-range disorder. The assumption guiding these developments was that pristine, as-grown nanotubes are clean. I believe this assumption to be true based on transport studies of as-grown nanotubes by other groups [63, 70, 27], and our own experience with as-grown nanotube devices described in Appendix B. Based on that assumption we set out to create devices that came as close as possible to the as-grown ideal while maintaining the requirements of multiple gates and charge sensing required for spin-qubit applications.

It should be pointed out in the beginning that all of the device designs described below 'worked' in the sense of producing gate-able carbon nanotube quantum dots on which transport and charge sensing measurements could be carried out. However, they *all* failed in the goal of reducing long-range disorder. They were all just as riddled with extra dots and random tunnel barriers—the manifestations of long-range disorder—as the first-generation devices described above. To be clear about the way these devices misbehaved, I note that they were not in general noisy or switchy.

The conclusion of this effort to reduce long-range disorder was that more than the substrate, or the ALD gate insulator, or defects in the nanotubes themselves, the dominant source of disorder in these devices was doing electron beam lithography over the nanotubes. The problem could be the resist or the beam itself, but disorder present in the bottom-gated/etch-through-ALD devices described in §A.2.4, combined with the cleanliness of the as-grown, ALD-coated devices described in Appendix B, strongly suggests that some aspect of the electron beam lithography process dominated the disorder in these devices.

A number of designs intended to reduce disorder were explored, including devices

that were

- smaller by a factor of two, sometimes annealed
- covered in an ALD insulator immediately following growth
- suspended above the substrate by wet-etching
- coated with ALD insulator as-grown, then top-gated

Each of these approaches are described in this section.

A.2.1 Smaller devices

With the arrival of the 100 kV Elionix ELS-7000, we were able to fabricate devices with dimensions about a factor of two smaller than had been possible with the 30 kV Jeol JSM-7000F. The length between contacts for the double dot portion of the device was reduced from about 1 μm to about 500 nm. The thinking was that smaller dimensions would make few-electron dots more controllable because less disorder would be incorporated over a smaller distance, and there would be half as many electrons in the device for a given density to start with. The effect on tunnel rates could be compensated by selecting nanotubes with slightly larger band gaps, but the large mass might also make them more susceptible to disorder.

A micrograph of such a device is shown in Fig. A.1. Aside from the new machine, the most important fabrication technique required to make this design work was cold-developed PMMA. We learned of this technique from the Berggren group [162] at MIT via Jimmy Williams. Later (and more successfully) we fabricated contacts and top-gate patterns using ZEP 520A ebeam resist. ZEP has the advantage of high resolution similar to cold-developed PMMA, but with 6 or 8 times faster exposures and superior lift-off.

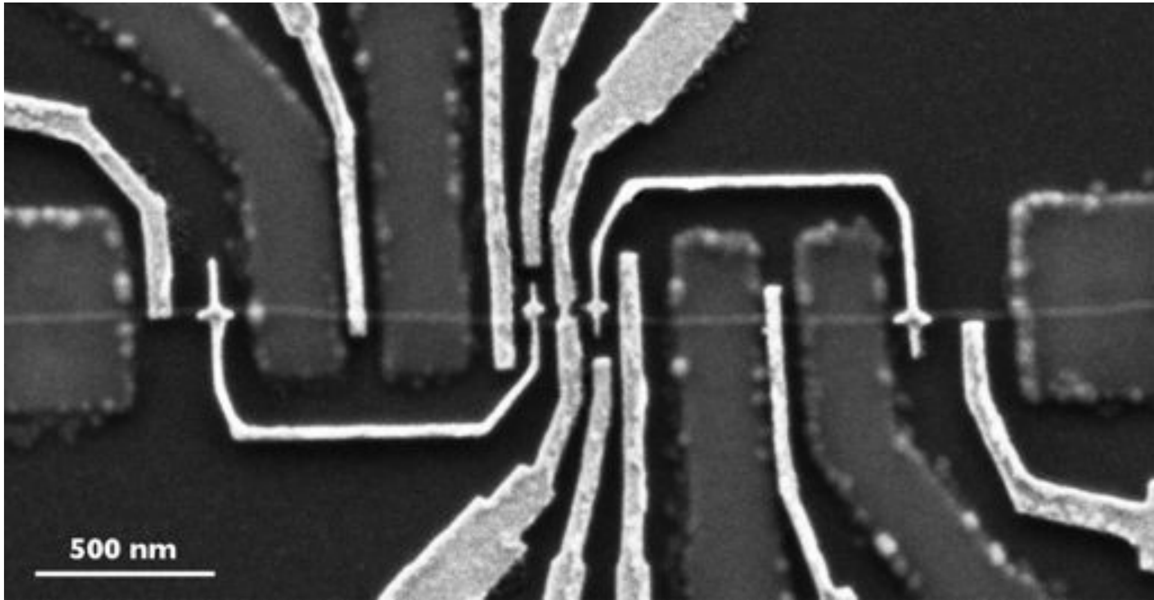

Figure A.1: Carbon nanotube double quantum dot device fabricated with the Elionix ELS-7000. The 100 keV beam and cold-developed PMMA allowed fabrication of devices approximately half as long as those used in Chapters 4 and 5.

Figure A.2 shows a comparison of a top-gate test pattern (dose test, best cases shown) made with PMMA (950K C2) and ZEP 520A dissolved 1:1 in anisole. The rough edges in the PMMA pattern are responsible for the bumps visible in Fig. A.1; such particles appear larger after application of Al_2O_3 by ALD. The downside of ZEP is that it is more difficult to dissolve than PMMA and requires either trichloroethylene or dimenthylsulfoxide (DMSO) in addition to acetone for complete removal. After lift-off in acetone only, scum remains that is visible in an optical microscope near the corners of the chip where the edge bead makes the resist thicker. DMSO and TCE give similar results, and we eventually settled on lift-off of ZEP in a 1:1 mixture of acetone and TCE since TCE was already part of the standard chip cleaning process. Additionally, ZEP should never be subjected to a UV-ozone de-scum after developing because it is sensitive to UV and can in fact be used as a deep-UV photoresist [164].

Other than size and choice of ebeam resist, the fabrication steps for these devices

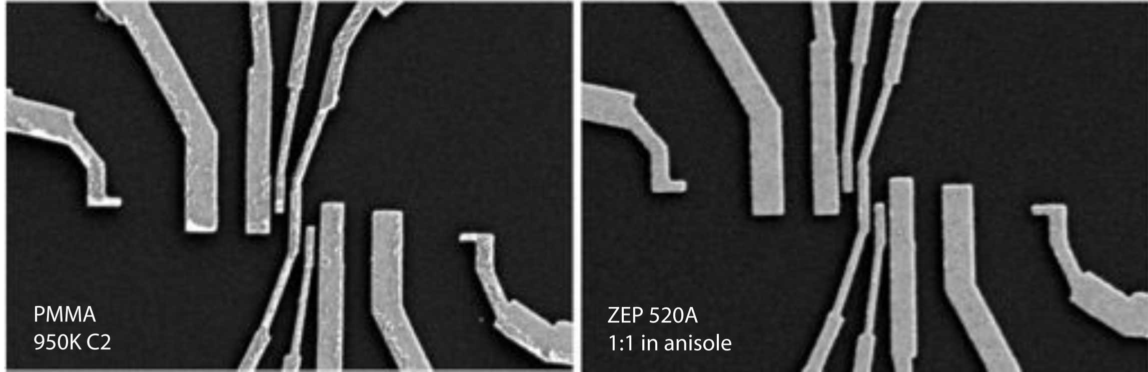

Figure A.2: Top-gates pattern with 950K C2 PMMA (top) and ZEP 520A diluted 1:1 in anisole (bottom).

were identical to those of the previous section. These smaller devices showed the same characteristics of high disorder—additional quantum dots, inability to tune barriers—that plagued the larger first-generation devices. Such an example is shown in Fig. A.3 for an etched-ALD device described in §A.2.2, where instead of the desired double quantum dot honeycomb, it can be seen that three quantum dots are present. The hallmark of a disorder-induced extra dot is its persistence over a wide range of gate voltages—they refuse to disappear. These data are representative of all of the approaches described in this section. At least two devices of each type described were measured in a dilution refrigerator, but undesirable data will not be repeatedly shown for each case.

In one generation of the smaller devices, we annealed them in forming gas after the contacting step. We tried anneal times of an hour for a range of temperatures between 300 and 700 C. Although promising shifts in mid-gap gate voltage position and contact transparency were observed, these devices did not show significantly less disorder than un-annealed devices.

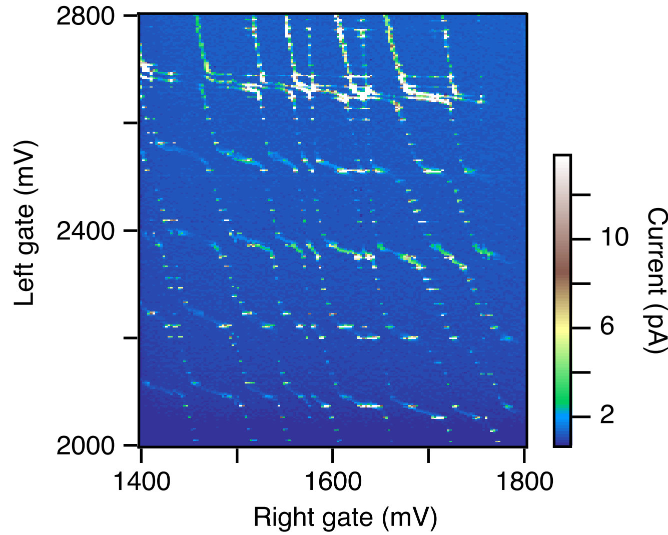

Figure A.3: Charging of a triple quantum dot is evident in this DC transport data for an etched-ALD double dot device.

A.2.2 ALD-covered devices

To control for the possibility that exposing the nanotubes to ebeam resist was the dominant source of disorder, we fabricated a series of devices in which the nanotubes were covered with ALD Al_2O_3 immediately following growth. With the ALD step moved in front of contacting in the process, an additional etch step to contact the nanotubes was required. Al_2O_3 can be etched in both HF and KOH, with the choice depending on whether the layer under the Al_2O_3 is Si or SiO_2. HF etches SiO_2 rapidly and not Si, and KOH etches Si rapidly and SiO_2 only slowly, so for these back-gated devices on SiO_2, it is preferable to etch the Al_2O_3 in KOH.

A 5% solution of KOH was prepared by dissolving 2 mg of KOH flakes in 40 mL of deionized water, and placed on a hotplate set to 80 C for 20 minutes (no thermometer was placed in the KOH, so its temperature could have been anywhere between room temperature and 80 C, but consistent from run to run). The etch rate of our ALD Al_2O_3 in this heated 5% KOH solution was 15 nm/minute. Nanotubes were located by SEM and contact patterns

designed and written as before. The easiest procedure would be to develop the contact pattern, etch the Al_2O_3, and deposit Pd contact metal, but the easy way is of course not possible. Although PMMA and ZEP do not dissolve in KOH (at least for etches up 5 minutes), the films tend to delaminate from the chip, much more for PMMA than ZEP. This delamination occurs with HF etches also, though only for resist on Al_2O_3 and not for resist on SiO_2. Even with ZEP, transfer of high-resolution patterns (such as the nanotube contact pattern) with a KOH etch is not possible because the film begins to delaminate and the etch runs under the resist mask. The solution we developed was to deposit a thin Cr sticking layer before spinning ebeam resist. Titanium is not a good choice for the sticking layer because it is etched rapidly in HF and becomes mushy in KOH [165]. This method made it possible to do accurate, small-area etches of Al_2O_3.

Using the Cr resist sticking layer, the process was

- cover entire chip with 5 nm Cr film by ebeam evaporation
- bake 2 minutes at 180 C, spin 1:1 ZEP:anisole at 5 krpm, bake 4 minutes at 180 C
- write etch pattern, develop ZEP: 20 seconds in o-xylene, 15 seconds in 1:3 MIBK:IPA, rinse in IPA
- 5 second dip in Cr etch, rinse in DI water
- 3 minute etch in '80' C 5% KOH
- rinse in water
- remove ZEP in 1:1 TCE:acetone for 5 minutes, rinse in acetone, then IPA
- 1 minute Cr etch to remove sticking layer
- proceed as in previous devices

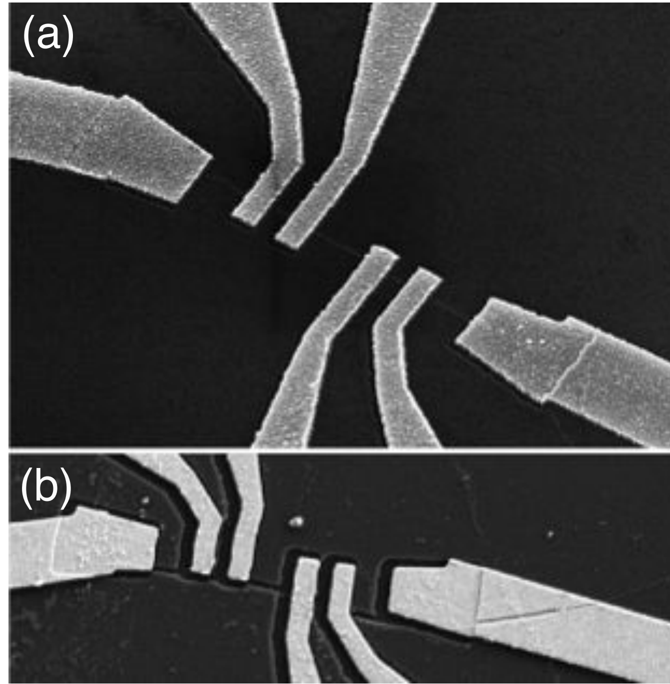

Figure A.4: Nanotube device in which the nanotube was covered with ALD Al_2O_3 immediately following growth, then windows in the Al_2O_3 were etched with KOH and Pd contacts were deposited. (a) Successful device. (b) Device in which KOH creeped rapidly along the nanotube (in addition to being over-etched because of the variability of the Cr-etch step).

A micrograph of one device contacted in this way is shown in Fig. A.4. Completed devices were no cleaner than previous devices, indicating that exposure to ebeam resist alone was not responsible for the disorder in our devices.

One mysterious observation during the fabrication of these devices is that for some nanotubes, once the KOH reached the nanotubes buried below the Al_2O_3, the KOH was able to zip along the nanotube quite rapidly and etch Al_2O_3 microns away from where the window in the resist was opened. An example of this phenomenon is shown in Fig. A.4(b), in which the path of the nanotube is traced out by etched Al_2O_3 (in this example, the Cr was also over-etched, but that is unrelated). We did not investigate which nanotubes allow this to happen, or whether the nanotube is destroyed in the process.

A.2.3 Wet-etch suspended devices

Another possible source of disorder in the devices described so far is the SiO_2 substrate on which the nanotubes lie, either because of charge traps in the oxide; poor interfaces among the SiO_2, Al_2O_3, and nanotube; or some combination of traps and interfaces. Both problems (except for the Al_2O_3/nanotube interface) could be solved by suspending the nanotube above the SiO_2 surface. A generation of devices was made in which after the contacting step, the nanotubes were suspended by removing 100 nm of the SiO_2 substrate with buffered HF, and maintaining suspension for further processing by critical point drying. Following suspension and critical point drying, the nanotubes were coated with ALD Al_2O_3 or HfO_2 and top-gates were added using a rotating two-angle evaporation as described below. A completed device is shown in Fig. A.5.

This section describes solutions to a few of the unique challenges posed by suspended, top-gated devices; in particular, maintaining suspension and fabricating thin top-gates over bumpy terrain.

Wet-etching and critical point drying

To create a suspended carbon nanotube device using nanotubes that are initially substrate-bound, the substrate must be etched away and the sample must be dried in such a way that the nanotube never touches a liquid-gas boundary, which would pull the nanotube with it as it recedes and either break the nanotube or stick it back down to the substrate. This is accomplished by critical point drying (CPD) and by keeping the sample in liquid at all times between the etchant and the dryer.

For nanotubes on Si/SiO_2 substrates, the most convenient etch is buffered hydrofluoric acid (BOE), usually diluted 1:5 in water (that is, 5 parts water). The etch rate of thermally grown SiO_2 in 5:1 BOE at room temperature is about 100 nm/minute. After

a 1 minute etch, the contact metal will be about 125 nm above the surface of the substrate, so it is impossible to run lines for top-gates over them. The solution is to pattern resist mask (as above, ZEP is best) so the etch only occurs within a few microns of the nanotube. Since the features are larger and the etches are shorter than in §A.2.2, it is not necessary (or even possible due to nanotube suspension) to use the Cr sticking layer to pin the resist mask in place.

After the BOE step, the sample will be very hydrophobic (incidentally, if you want a hydro*philic* sample, do an O_2 plasma etch), which means when it's removed from the BOE, the bead of water on top of the chip will run off and the sample will be ruined. The best way around this problem is to set the sample in a small cup within the BOE beaker, so

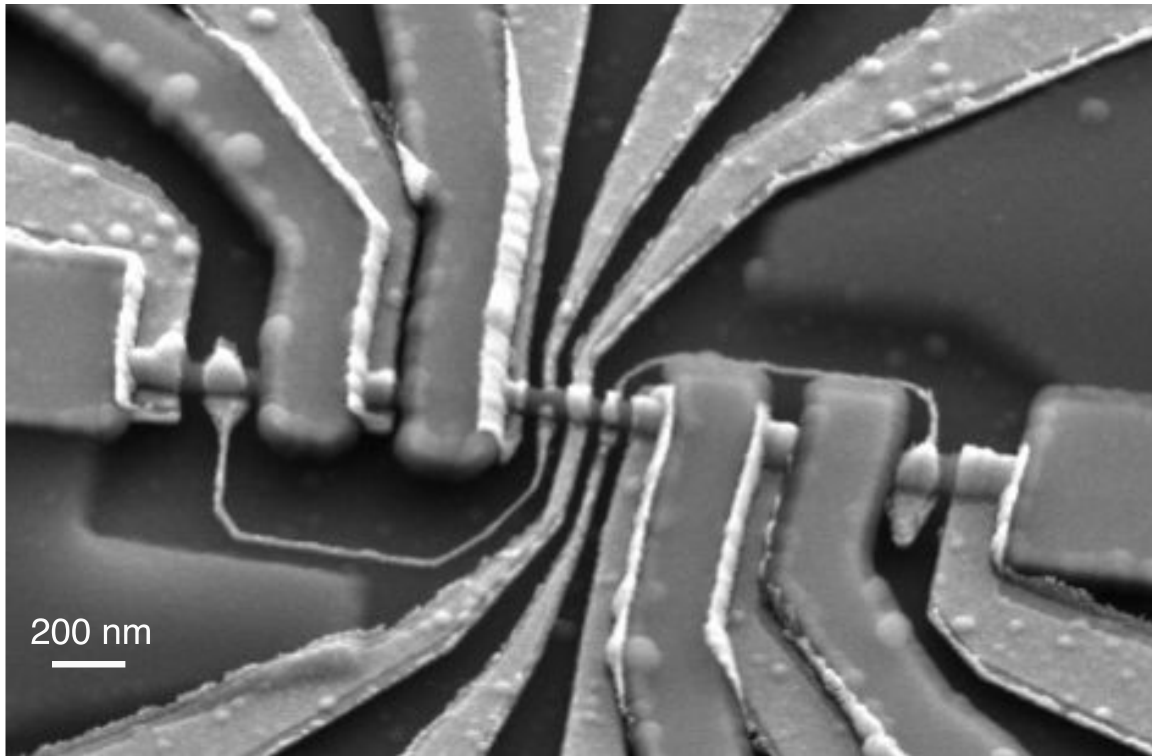

Figure A.5: Nanotube device in which the nanotube was contacted with Pd, etched in 5:1 buffered oxide etch for 60 seconds, critical point dried, coated with ALD Al_2O_3, and top-gated with a rotating two-angle evaporation.

it's always sitting in a small bath of something as it is transferred from BOE to water for rinsing to methanol for the CPD. Because there's more HF to dilute with the small cup, we generally used two beakers of DI water sequentially for rinsing.

Angled evaporation of very thin films

Once the devices were suspended, we coated them with 40 nm of NO_2 functionalized Al_2O_3 or HfO_2, followed by top-gates. Because the linewidths of the sensor couplers and plunger gates were approximately 20 nm, top-gate metal cannot be much thicker than 20 nm, and certainly not the 80 nm required to climb up the side of the Al_2O_3-coated suspended nanotube. The solution to this problem was to do a three-angle evaporation: one at normal incidence to metallize the sensor couplers and thin plungers gates, and two at 30 degrees to hit each sidewall of the nanotube. This procedure was inconvenient because it required three pump-downs of the evaporator chamber, and would only work for one nanotube orientation within the plane of the chip. A more convenient solution was to have a rotating, tilting sample stage built for the ebeam evaporator which provided *in situ* control of the angle of the chip relative to the ebeam source (up to about 45 degrees) and control over the rotation of the sample about the tilted axis. A picture of the rotating, tilting sample holder I designed with help from CNS PVD guru Ed Macomber is shown in Fig. A.6.

Coating suspended devices with ALD created an additional problem, which is that the changes in band line-ups between the nanotube and Pd contact metal got worse compared to substrate-bound devices (see §A.1.8 for a more detailed description of the problem). This meant that rather than going from strong p-type conductance to mediocre p-type conductance with Pd, we were left with unacceptably poor p-type and n-type conductance. We initially wanted HfO_2 top-gate dielectric to improve sensor coupling and increase the

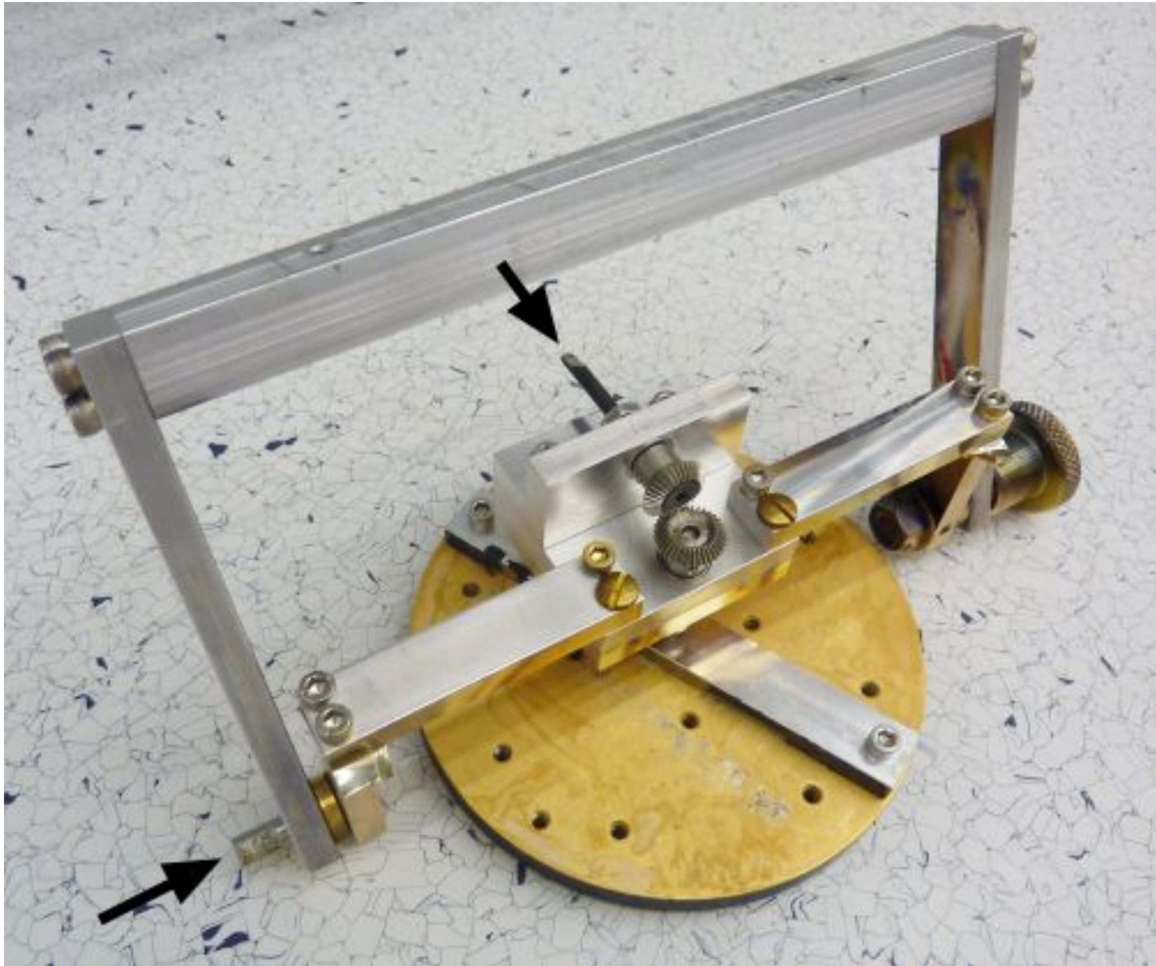

Figure A.6: A rotating and tilting sample for stage for electron beam evaporation at angles up to about 45 degrees with continuous rotation about the tilted axis. The stage is mounted to the evaporator using the two bolt holes on top, and flexible shafts are attached at the points indicated with arrows to allow rotation (motor: Lesker MagiDrive KZSADC-A) and *in situ* tilt control. The knob on the right side can be used to lock the tilt angle if desired.

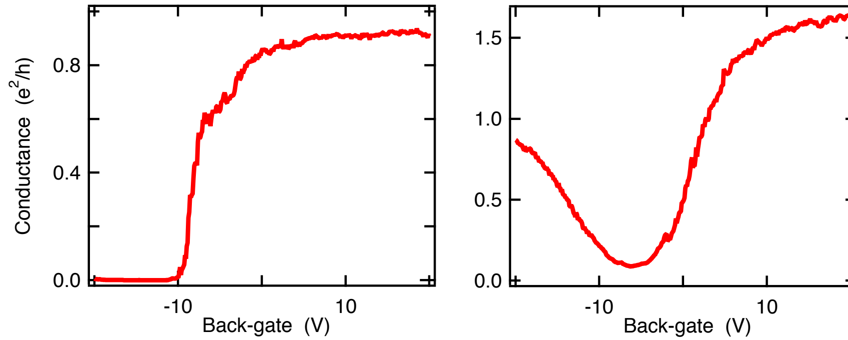

Figure A.7: Room-temperature back-gate sweeps for two Sc-contacted nanotubes.

nanotube level spacing, but as mentioned above, dielectric-induced work function shifts are proportional to κ, so the problem was more severe with HfO_2 than with Al_2O_3. Hoping that we would have more luck with electrons than with holes, we made a batch of devices using scandium contacts, which have been shown to make transparent contacts to the conduction band of nanotubes [166].

We found this to be the case, as shown in Fig. A.7, but unfortunately scandium is such a reactive metal that it was incompatible with our suspension and top-gate procedures (it is rapidly etched in most acids and oxidizes to a thickness of at least 50 nm at temperatures as low as 120 C). The up-side of its reactivity is that it is an excellent getter in evaporation chambers, better than titanium and chromium in our experience. We tried various means of protecting the Sc, but it was not a fruitful direction.

Here is the recipe for wet-etch suspended devices of this type:

- Fabricate Pd-contacted nanotubes as in section A.1
- Pattern etch mask using 1:1 ZEP:anisole, develop 20 seconds o-xylene, 15 seconds 1:3 MIBK:IPA, rinse in IPA
- Etch 1 minute in 5:1 BOE inside small dipper cup, rinse in two separate DI water

cups

- Still using the dipper, transfer to a cup of methanol, then the methanol in the critical point dryer
- During the drying step, be patient! Be patient when replacing the methanol with CO_2, be patient when warming up, and be patient when releasing the CO_2 at the end. If the CO_2 boils or condenses on the chip, it's ruined.
- Deposit 40 nm of NO_2 functionalized Al_2O_3.
- Fabrication top gates using 1:1 ZEP:anisole. Deposit 1/12 nm Ti/Au with no tilt, then tilt to 30 degrees and deposit another 1/20 nm Ti/Au with the rotation going.

As with previous generations, these devices did not show signs of reduced disorder, indicating that protecting nanotubes from ebeam resist and removing the SiO_2 substrate were not sufficient by themselves to create clean devices.

A.2.4 Suspended as-grown, ALD insulator coated, top-gated devices

This generation of devices represented the closest a top-gated device could come to the as-grown ideal. Two different design strategies were tried (as described below) but they all shared the feature of growing nanotubes over pre-patterned contacts, coating them with ALD Al_2O_3 or HfO_2, and placing top-gates and charge sensing couplers over them. The biggest challenge of this approach was in creating a contact pattern that was large enough to have a significant probability of having a nanotube land on it, but small enough to allow high sensitivity charge sensing. We assumed running sensor couplers over contact metal would destroy sensitivity. This assumption was never tested, but the nanotube's small diameter hurts here: the capacitance of the coupler would be dominated by the hundreds of

nanometer wide contact metal rather than few nanometer wide nanotube. Subject to the constraint that the couplers must run around the contacts and not over them, the width of the target for nanotubes presented by the contacts could only be a few hundred nanometers to keep the total coupler length below a couple microns. Any longer and the capacitance to the backgate would begin to hurt sensitivity. A detailed, numerical analysis of similar considerations in the context of two-dimensional quantum dots is provided by Trifunovic *et al.* [45].

The first designs of this type had the contacts patterned as six concentric, nearly closed rings. To allow short sensor couplers, the rings would be undercut with BOE near the nanotubes so they would break when the chip was dried. It was possible to break the rings within about 200 nm of the nanotube. The rings were made circular to keep the contact spacing constant in light of random nanotube orientation, and nearly closed to catch as many nanotubes as possible on the assumption that finding a nanotube bridging all six contacts would be a rare event (it was). Given that rarity, many thousands of rings were fabricated on each chip, and there were two methods pursued to measure only the rings with successful nanotube contact. One idea was to connect about 50 rings on six long bus lines ending in bond pads, and the bus connections to all but the ring of interest would be destroyed by undercutting them with an HF etch and sonicating. The advantage of this approach was that small-area etching of ALD oxide was not necessary, but the yield of the interconnection destruction was not 100%, so this direction was abandoned. The large number of bus connections placed too tight a constraint on the yield of bus-busting.

Isolated ring devices and etching HfO_2

In the second approach, all the of the rings were isolated from each other, and each ring terminated in a pad so that by etching the small area of Al_2O_3 or HfO_2 over

the pads, contact could be made to the rings. As shown in Figure A.8, a large array (nine 15×15 grids) of rings were patterned on each 5 mm chip, and nanotubes were grown across the contacts (sometimes) by placing catalyst in the center of the rings. Once the nanotubes were coated with 40 nm of Al_2O_3 by ALD,[3] they could be located with an optical microscope [Fig. A.8(c)]. To eliminate shunt capacitance for the sensor couplers, the rings could be broken off with about 200 nm accuracy by undercutting them in HF (the rings were composed of SiO_2/Cr/W/Pt) and sonicating. Conveniently, the ebeam evaporated SiO_2 layer under the contacts etches much faster than the bottom layer thermal SiO_2. The top-gate patterns were the same as for the wet-etch suspended devices.

We learned two useful facts in pursuit of this direction. First, ALD HfO_2 is difficult to etch selectively. The etch rate of HfO_2 in BOE at room temperature is only a few nm/minute, which is so much slower than the SiO_2 etch rate that it is impractical to use (ideally an etch would stop when the HfO_2 is gone, but in this case, the rate would take off). This rate mismatch is a problem even when etching down to metal pads because the alignment is never perfect and the etch is never perfectly localized. BOE etching of HfO_2 on SiO_2 can be made nearly workable by diluting 49% HF (we did not try BOE) 1:4 in methanol (this particular combination of acid and solvent does not explode). It works not by speeding up the HfO_2 rate but by slowing down the SiO_2 rate (by about 10x), so that the HfO_2 is only a few times slower than the SiO_2 rate. Still, it was difficult to get the etch time just right, so we went with Al_2O_3. We did not try dry etches out of (a perhaps unfounded) fear of damaging the nanotubes.

[3] We later found that 50 nm of Al_2O_3 makes them significantly easier to see.

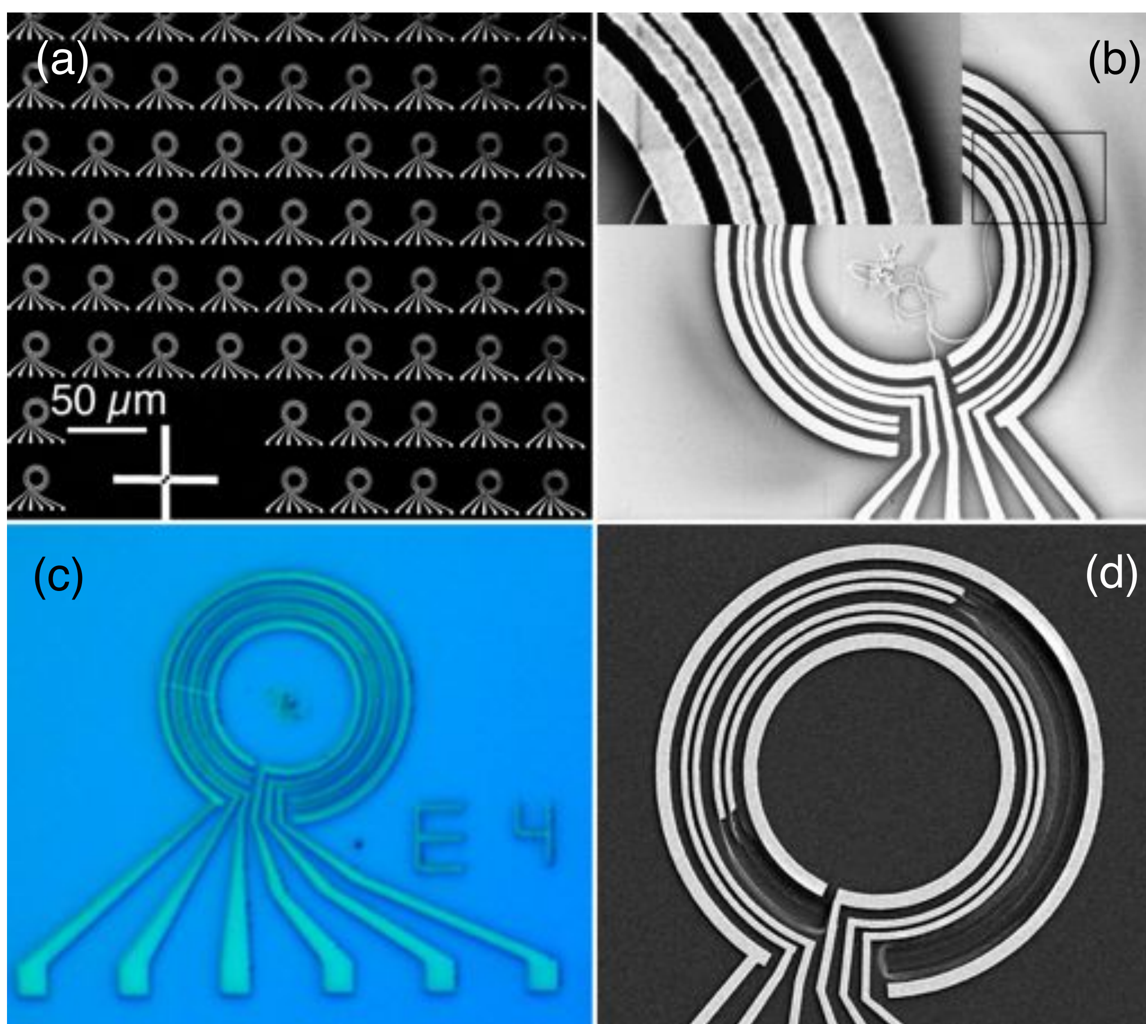

Figure A.8: (a) Array of ring contacts. (b) Catalyst was placed in the center of the rings so that, occasionally, a single nanotube was be suspended across the contacts. Inset: detail of region inside black rectangle. (c) Once the sample was coated with 40 nm of Al_2O_3 by ALD, suspended nanotubes were visible in an optical microscope (100x objective, NA 0.9). In this case the nanotube is pointing at about 9 o'clock. (d) To eliminate charge sensor shunt capacitance, the contacts were undercut and broken off by sonciation.

IPA as an Al_2O_3 precursor for ALD

The second useful fact we learned was that neither KOH nor HF will etch through the NO_2 and trimethylaluminum (TMA) functionalization layer. We found that when the etch had clearly made it all the way through the Al_2O_3, we could not successfully contact the metal pads underneath. As confirmed by test devices with and without the NO_2 step, the NO_2 was the problem. Another ALD process that adheres to pristine nanotubes was needed, and Allen Hsu of the Palacios group at MIT had suggested trying IPA instead of water as the oxygen supplying precursor in the Al_2O_3 process for making Al_2O_3 stick to hydrophobic surfaces such as some polymers [167, 168] and as-grown carbon nanotubes. This process worked quite well and Al_2O_3 with IPA precursor sticks to as-grown nanotubes with fairly good coverage up to about 150 C. This process is comparable to the NO_2 process in terms of nanotube coverage, but has two signifiant advantages. First, it is not sensitive to the dose of IPA used, so it is a much more reproducible process. Second, the film is Al_2O_3 all the way through, without an intermediate film of unknown thickness or structure. The reaction of IPA with TMA is not quite as complete as H_2O with TMA; consequently, there is more residual carbon in the IPA/TMA films and we therefore deposited only as much of the IPA film as needed for adhesion (typically 50 cycles). Room temperature characterization of two nanotube devices (chosen to be representative of typical behaviors) before and after coating with IPA/TMA Al_2O_3 is shown in Fig. A.9. For one device [Fig. A.9(a)], the position in gate voltage of the middle of the band gap did not shift appreciably, but the contact transparency increased for electrons and decreased for holes, consistent with the changing band offsets due to the Pd/Al_2O_3 and nanotube/Al_2O_3 interfaces. For the other device [Fig. A.9(b)], the midgap position shifted much closer to zero, but the overall conductance was reduced somewhat. In both cases the conductance traces were noisier before coating with ALD.

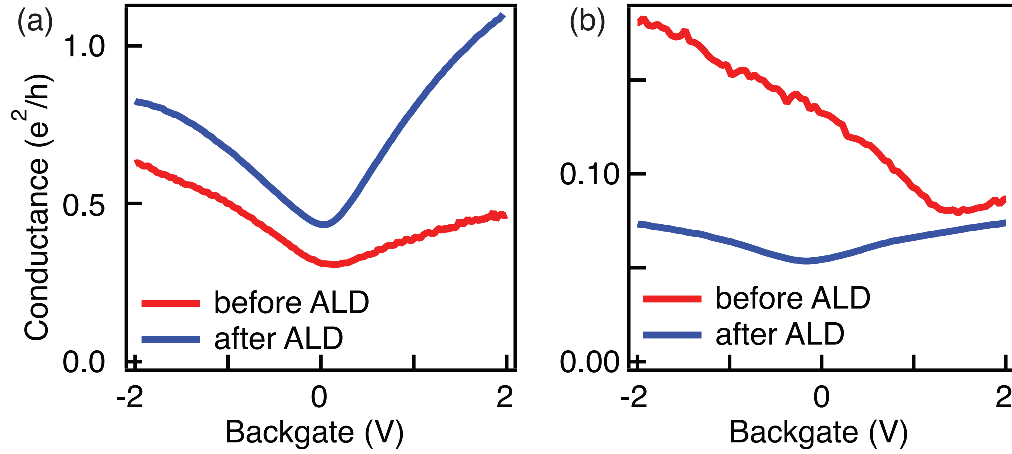

Figure A.9: Room temperature conductance vs. backgate sweeps for two suspended devices before and after depositing 40 nm of Al_2O_3 by ALD.

At lower temperatures (30-35 C) we were surprised to learn that neither NO_2 nor IPA is required to make Al_2O_3 stick to nanotubes. H_2O and TMA stick just as well, so that is the process we settled on in the end for the bottom-gated devices described in Appendix B. The coverage of the nanotube by Al_2O_3 is quite good using this process, as demonstrated in Fig. A.10.

Dashed-ring devices

To avoid the additional step of breaking the rings off near the devices to make a low-capacitance channel for the sensor couplers, the final design we pursued for these suspended as-grown, ALD-coated, top-gated devices was to fabricate the rings as dashed lines as shown in Fig. A.11. The price of this simplification was slightly lower yield since the nanotubes would be less likely to land on the contact pads, as well as a requirement of more precise Al_2O_3 etching since the contact pads could not be made very large. As for the isolated ring devices described above, nine 15×15 arrays of rings were fabricated on each 5 mm chip (one 15×15 array, mostly covered by bond pads, is shown in Fig. A.11(a)). With

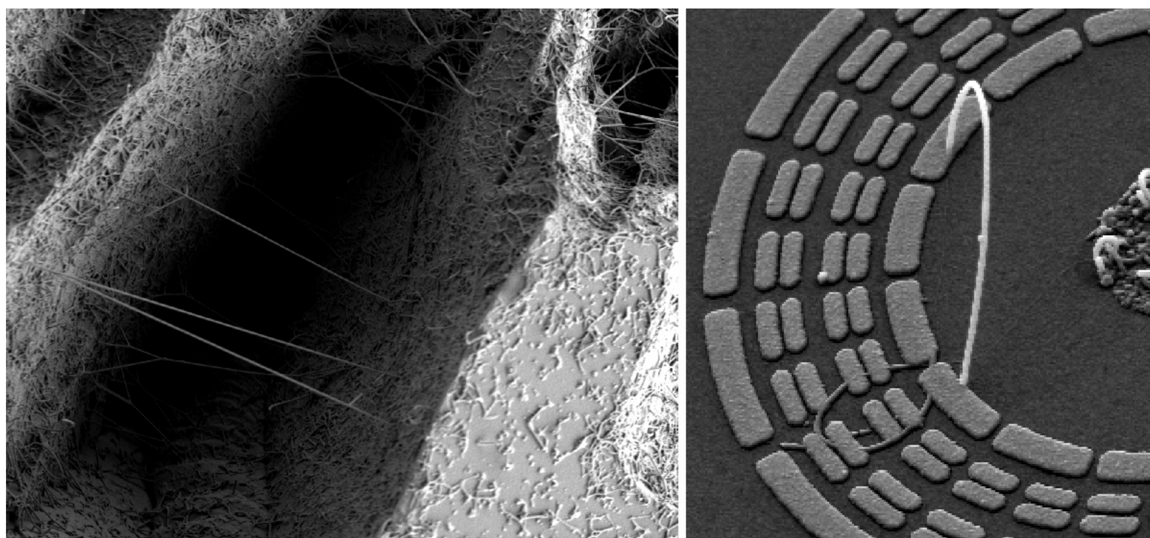

Figure A.10: Left: nanotubes are suspended across a trench (catalyst deposited directly on scribed silicon) for 20 μm with no gaps in coverage by Al_2O_3 using low temperature ALD process. Right: An nanotube arch with a diameter of ~ 5 μm also shows uniform converage.

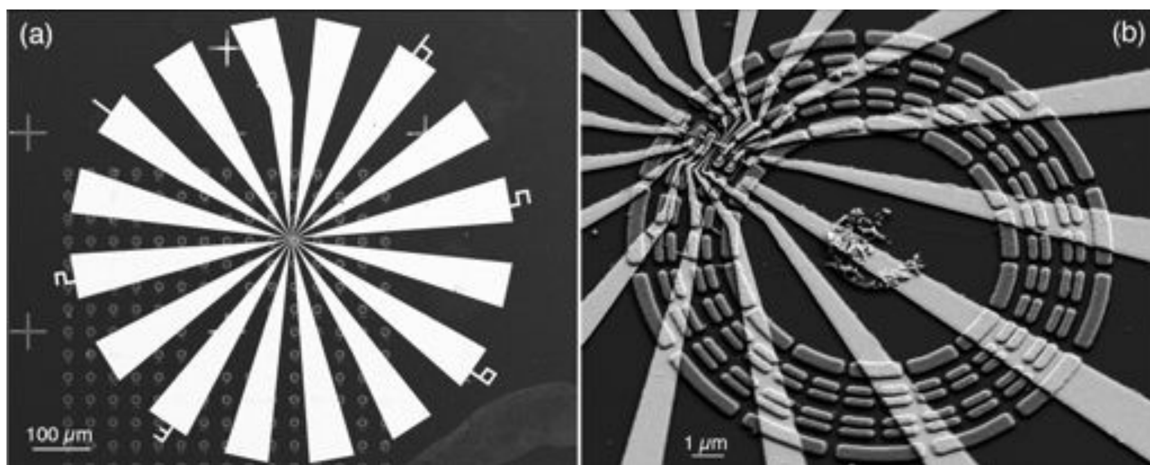

Figure A.11: (a) Nine 15×15 arrays of dashed-ring patterns were placed on each 5×5 mm chip so that one device per array could be contacted. Numbered bond pads are contacts to facilitate room temperature screening. One pad is crooked to avoid a short near an alignment mark. (b) Zoom-in on a single ring with a completed device. Catalyst is placed in the center of the ring. A rotating two-angle evaporation is required to have the thin top-gate metal run continuously over the tall ($\approx$ 80 nm) contact pattern and suspended nanotube.

this strategy, nine complete devices could nearly always be made per chip.

A completed dashed-ring device is shown in Fig. A.12. The recipe for making such a device (which is not recommended in light of the results in Appendix B) is

- Pattern alignment marks and dashed rings on a Si/SiO_2 substrate using 1:1 ZEP:anisole.
- Deposit 50/2/10/20 nm of SiO_2/Cr/W/Pt by ebeam evaporation (the Cr is unnecessary and not recommended, but that's what was used).
- Pattern catalyst pads using either 950K C2 PMMA or photolithography.
- Deposit nantube catalyst (iron nitrate recipe) and grow carbon nanotubes.
- Immediately after growth place in ALD reactor and deposit 50 cycles of Al_2O_3 at 30 C and 400 cycles at 250 C.
- Deposit 5 nm Cr sticking layer by ebeam evaporation, spin on 1:1 ZEP:anisole, and pattern etch mask.
- Etch Cr for 5 seconds in Cr-etch, then etch 2 minutes 30 seconds in 5% KOH at '80' C, remove ZEP with a five-minute soak in TCE/acetone, three solvent clean, 1 minute Cr etch, then three solvent clean.
- Pattern top-gates and connections to contact pads using 1:1 ZEP:anisole.
- Deposit 1/12 and 1/20 nm Ti/Au using rotating/tilting sample stage at normal incidence and 30 degrees with rotation on.

CVD-compatible metal stacks

One useful process we developed in the course of making top-gated, suspended devices was how to make metal stacks that survive the CVD process for nanotube growth.

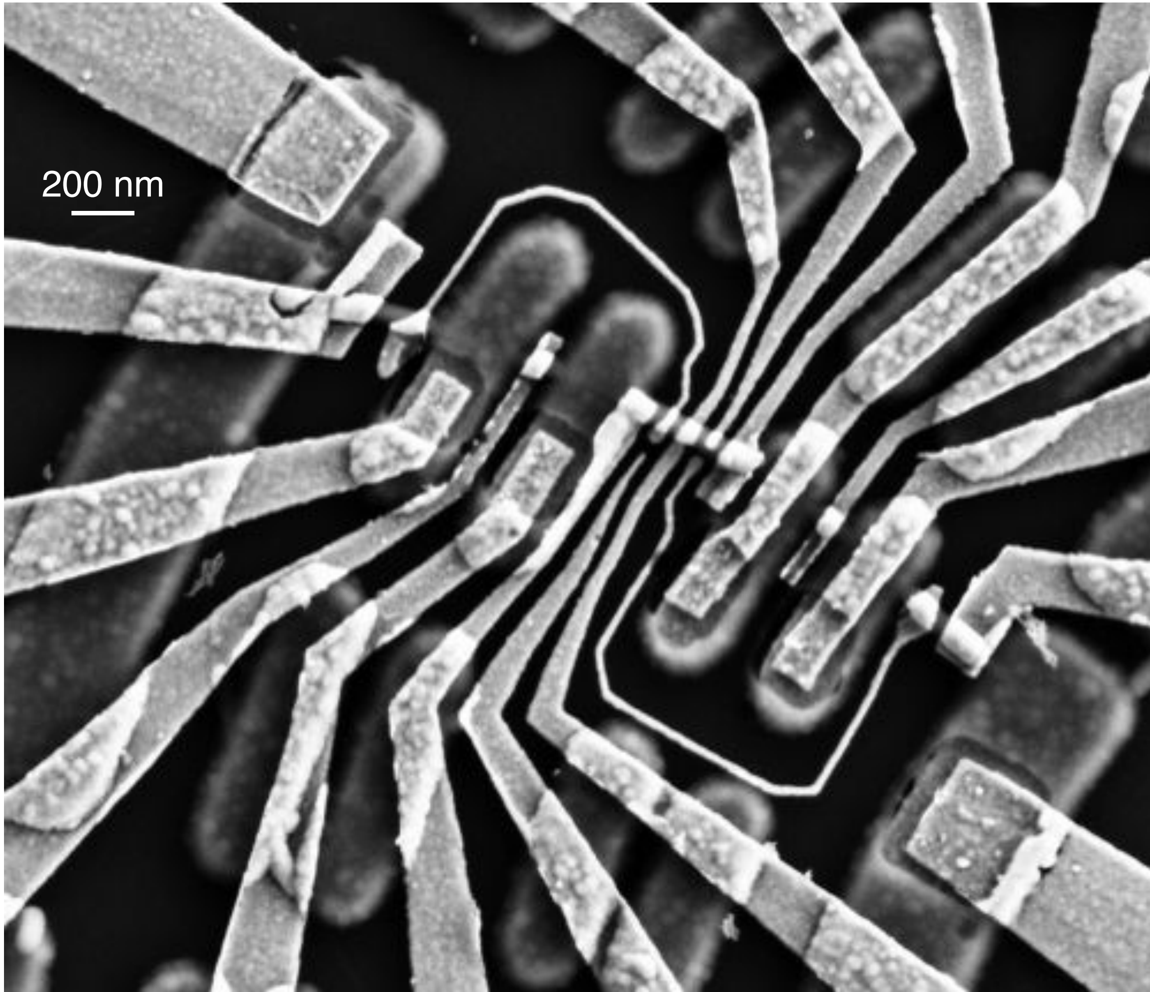

Figure A.12: Suspended as-grown, ALD-coated, top-gated device. A carbon nanotube was grown suspended over SiO_2/Cr/W/Pt contact pads and coated with 50 nm of Al_2O_3 by ALD immediately following growth. The Al_2O_3 was etched to make windows for contact to the pads, and Ti/Au top-gates were deposited in a two-angle rotating evaporation.

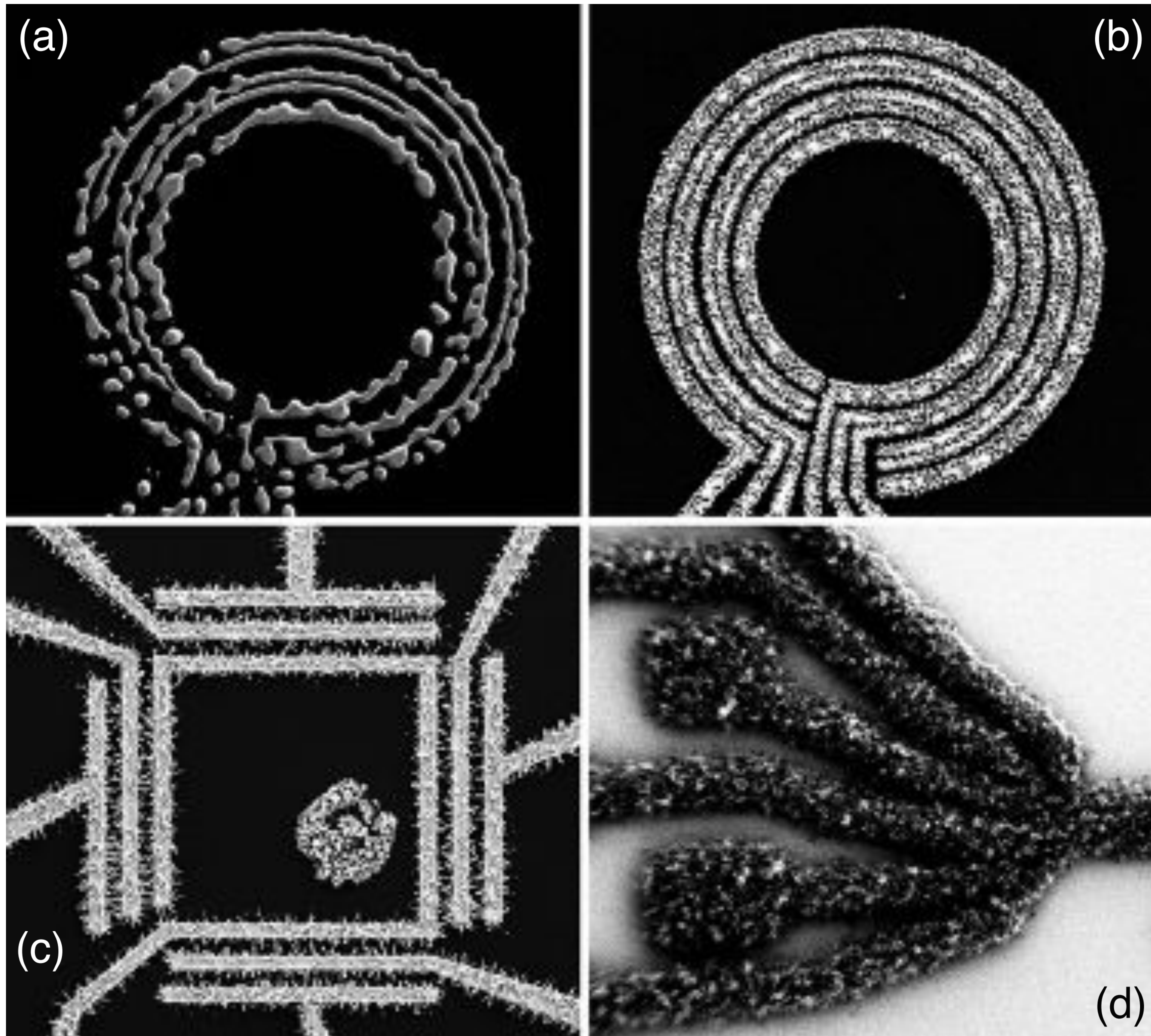

Figure A.13: (a) 2/75 Ti/Pt. (b) 20/10/50 Ti/W/Pt. (c) 2/20/50 Ti/W/Pt. (d) 2/10/60 Ti/W/Pd. The recommended stack is 50/10/20 SiO_2/W/Pt.

The difficulty is that most combinations either melt, react violently, or grow nanotubes themselves. Four examples are shown in Fig. A.13, in which devices are shown with several variations on the recipe above. By omitting W, the Pt melts and balls up [Fig. A.13(a)], using a lot of Ti (20 nm) allows it to burst through the W and Pt [Fig. A.13(b)], using too much W (20 nm) causes it to sprout some kind of nanowires [Fig. A.13(c)], and, most shockingly, using Pd instead of Pt as the top layer creates an extremely efficient catalyst for multiwalled nanotubes [Fig. A.13(d)].

A.2.5 ALD upgrade

Around the time we were making ALD-covered devices, we decided to upgrade our ALD system with new valves and plumbing below the sample chamber for better reliability (the old valves broke frequently) and better compatibility with the NO_2 functionalization process. In the old configuration, the water and NO_2 precursor lines were unheated and joined at a tee below the pulse valve so there was always a mixture of the two reacting in the tee. This arrangement made it difficult to clear out the lines by pumping and allowed nitric acid to form in the tee. We also wanted to be able to have the system configured to deposit Al_2O_3 and HfO_2 without having to swap precursor cylinders and worry about cross-contamination of the valves.

To address these problems, the number of valves and precursor lines was increased from two to four, we switched from the original Parker valves to Swagelok ALD valves,[4] the water and NO_2 lines were made to be completely separate until they reached the sample space, and a combination of an expanded heater block and heat tape was used to prevent accumulation of unreacted precursor in all areas of the system. Pictures of our ALD system

[4]Part number 6LVV-ALD3TA333P-CSVH. These valves also require MAC solenoid pilot valves powered by compressed air, MAC part no. 34C-ABA-GDFC-1KT. Quick-connect fittings to these valves can be made with Legris part no. 3198-04-19 and 3199-04-19.

Figure A.14: Cambridge Nanotech Savannah 100 ALD system before and after converting it from two Parker valves (aluminum precursor on one, H_2O and NO_2 on the other) to four Swagelok valves (H_2O, aluminum precursor, hafnium or zirconium precursor, and NO_2 or IPA) with improved heating of precursor lines. Inset: valve assembly and heater block before application of thermal insulation and attachment of precursor cylinders.

before and after the upgrade are shown in Fig. A.14. The valves were heated with two 1/4" diameter cartridge heaters (one 300 W inserted in front, the other 250 W inserted in back) powered by the Cambridge Nanotech e-box. The heater block was insulated with 1/4" thick silicone foam. Testing before the foam was applied showed it to be necessary with the heater cartridges used. Three RTD probes for temperature control were read out by the e-box and inserted in the heater block (150 C), the NO_2 heat tape (100 C), and the exhaust bellows heat tape (100 C).

With these changes, our ALD system produced films with more reliable effects on threshold voltages and contact transparency, and was able alternate between films of

Al_2O_3 and HfO_2 without cross-contamination problems.

Appendix B

Bottom-gated, as-grown carbon nanotube single and double quantum dot devices

This appendix describes the fabrication and some measurements of carbon nanotube single and double quantum dot devices in which nanotube growth is the last (or next to last, in the case of ALD-coated devices) processing step, so-called 'as-grown' devices. By encouraging nanotubes to extend over trenches during growth, they are freely suspended from the outset. This process is the ideal for studies of low-disorder devices because the nanotubes are pristine with the exception of amorphous carbon that may be accumulated in the growth furnace and gas adsorbed during transfer from the furnace to a cryostat. Remarkably, this process is also the *easiest* way to fabricate nanotube quantum dots in the case of back-gated single dots. Because of the random placement of the nanotubes during growth, we initially thought this fabrication method was incompatible with spin qubit experiments requiring charge sensing. However, with the introduction of dispersive readout

for spin qubits [169] described in Appendix D, it became possible to do charge sensing with the cleanest devices because dispersive readout requires only the attachment of a resonant circuit to a lead or gate of the device rather than a dedicated proximal charge sensor.

B.1 Single dot devices

Only a few steps are required to make a single dot device as shown in Fig. B.1:

- Contacts patterned with 1:1 ZEP:anisole, 40/2/10/30 nm SiO_2/Cr/W/Pt by ebeam evaporation.
- Bond pads patterned using chlorobenzene photolithography process (described below, see Fig. B.5), 5/25/50 Cr/Pt/Au.
- Catalyst pads patterned with C2 PMMA, iron nitrate/molybdenum acetate/alumina catalyst, standard nanotube growth.

Using tungsten and platinum as contact metals for as-grown nanotubes is standard, but the use of ebeam evaporated SiO_2 is not. The idea is to avoid etching the substrate, which could be accomplished with thicker W and Pt layers (the trench should be at least a tenth as deep as it is wide to have a high probability of suspension), but in that case the metal does not hold up as well in the furnace. But putting a pad of SiO_2 under the contact metal, the metal can be thin enough to remain relatively smooth after growth and still maintain the right aspect ratio for the trench. Another advantage of this approach is that thick layers of tungsten sprout short, mutli-walled nanotubes of their own, which cause electrical shorts if they are longer than the contact spacing. We settled on 10 nm as a thickness of W that is enough to stabilize the Pt layer without generating very many

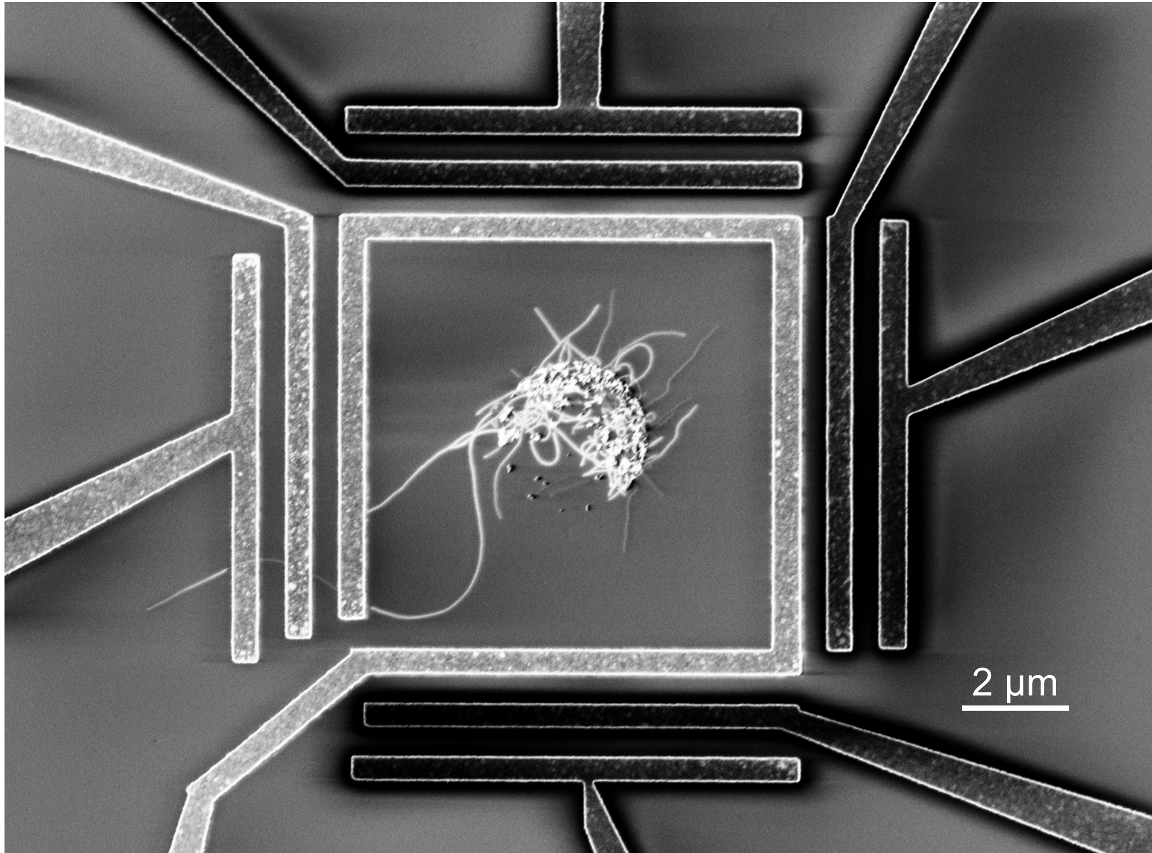

Figure B.1: Carbon nanotube suspended across three SiO_2/Cr/W/Pt (Pt on top) contacts to make two separate back-gated single quantum dot devices with the same nanotube. The nanotube appears narrower where it is suspended and wider where it is bound to the substrate due to charging of the substrate. Charging of the contacts is responsible for the brighter shade of the contacts bridged by the nanotube compared with those with no nanotube. The central circle is composed of Fe/Mo catalyst particles. Image: Zeiss Ultra55 SEM, 2 keV, WD 5 mm, In-Lens detector.

stray nanotubes (see also §A.2.4). The Cr under the W is not necessary and also not recommended because it can diffuse during growth, but that was the recipe at the time.

In order to have a reasonable chance of getting a nanotube to land across the contacts, a large number of contact patterns must be written. In this case the device shown in Fig. B.1 was patterned using the Raith 150 ebeam writer rather than the Elionix ELS-7000. With 400 nm wide contacts and no fine gates, high resolution was not required, and

writing at 30 keV rather than 100 keV provides a factor of 3 improvement in speed assuming dwell time and not blanker speed dominates the write time.

These devices are easy to make, but the downside is there is no control over the tunnel barriers defining the quantum dot for a given charge state because there is only one global back-gate. In order not to give a false impression about these devices, it should be pointed out that in practice, many devices must be screened to find the ones with the desired tunnel couplings. Conductance measurements as a function of back-gate voltage at room temperature and dilution refrigerator base electron temperature are shown in Fig. B.2 to provide a reference point for device screening, though devices that look identical at room temperature can behave very differently at low temperature. When the nanotube is populated with holes at negative back-gate voltage, the conductance is high, which is typical of contacts to nanotubes by high work function metals such as Pt and Pd. At more positive back-gate voltages when the nanotube contains electrons, the tunnel barriers are much larger and a weakly coupled quantum dot is observed.

Focusing on the first shell of four electrons, it is instructive to follow the positions of the ground-state Coulomb peaks at zero bias as a function of nearly parallel magnetic field (nearly, because the angle of the nanotube with respect to the electrodes is random for this style of device), Fig. B.2. The movement of the ground states with parallel magnetic field can be fit to the single-particle Hamiltonian eq. (2.4) that accounts for spin and orbital magnetic moments, spin-orbit coupling, and valley coupling, resulting in the green lines in Fig. B.2 with parameters $\mu_{\text{orb}} = 0.39$ meV/T, $\Delta_{SO} = 0.31$ meV, and $\Delta_{KK'} = 0.42$ meV. The model is fit only over its range of applicability (it stops when the parallel field moves the quantization line close enough to the Dirac point to bend the states. The agreement is quite good for the first two electrons, but it is evident that this model does not fully describe the data for the third and fourth electrons in the shell. One of two extensions

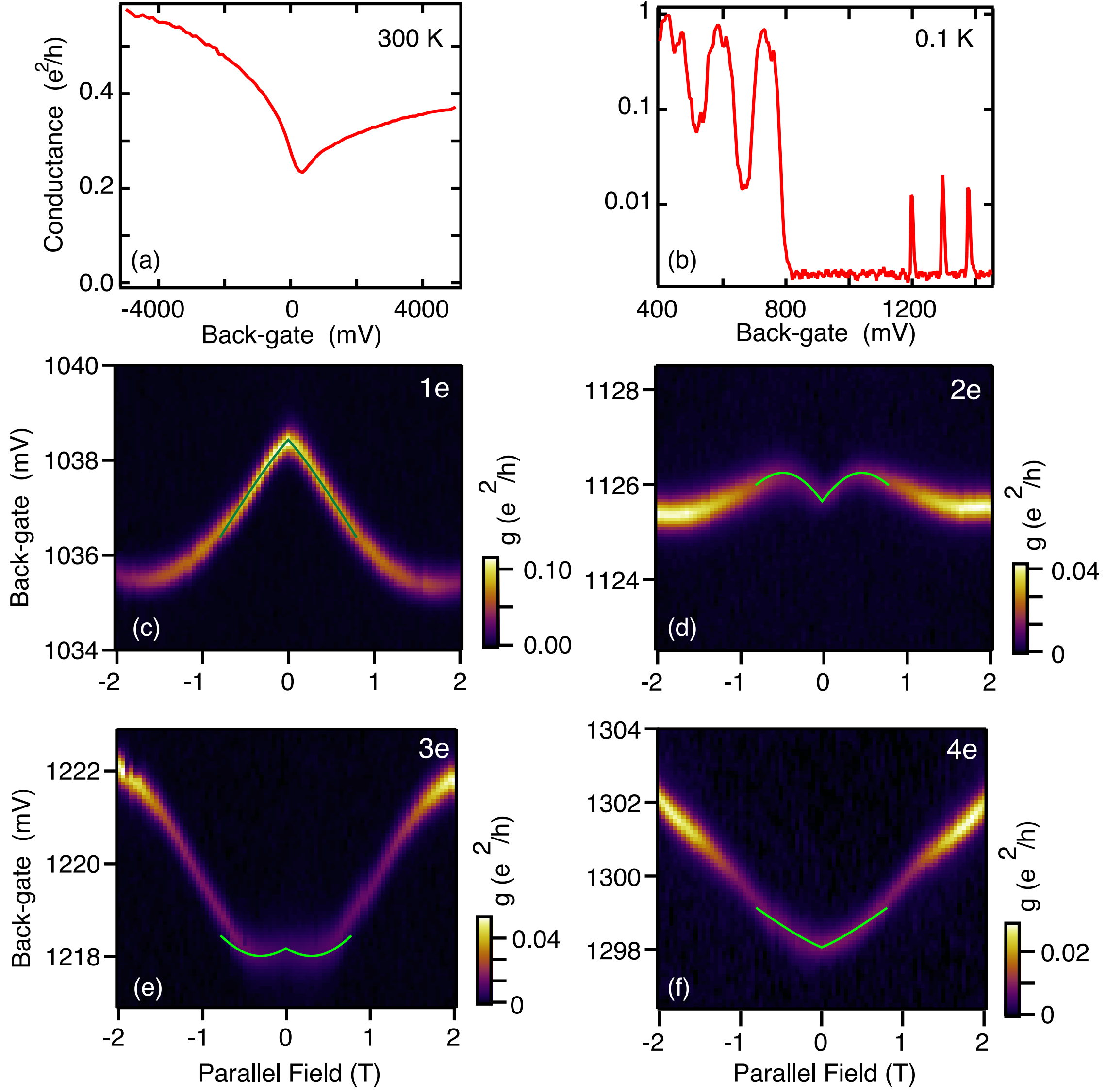

Figure B.2: (a) Room temperature and (b) 0.1 K back-gate sweeps illustrating the connection between room-temperature screening and low-temperature properties. (c)-(f) Movement of the first shell groundstates with nearly parallel magnetic field. Green lines are fits to eq. (2.4) with parameters $\mu_{\text{orb}} = 0.39$ meV/T, $\Delta_{SO} = 0.31$ meV, and $\Delta_{KK'} = 0.42$ meV.

to the model could potentially bring it into agreement with the data. One possibility is that the valley coupling changes with electron occupancy, which may be unexpected given that the longitudinal wavefunctions are identical for all electrons within the same shell. On the other hand, the current level changes with occupancy, indicating some change in the wavefunction with back-gate voltage. The other possibility is that the exchange interaction becomes important when more than one electron occupies the dot. Distinguishing between the two cases would require some *in situ* control over the length (to affect exchange) and/or longitudinal location (to affect valley coupling) of the dot, neither of which was available in these devices. A gate-voltage dependent valley coupling would be useful in the context of spin-valley qubits in nanotubes, because it would allow an electric dipole spin resonance mechanism similar to that used in GaAs spin qubits [170], except that here the spin rotations might not be incoherent as in the inhomogeneous hyperfine mechanism.

One remark that can be made about the data shown in Fig. B.2 is that even though the device was fabricated with a method that is sometimes referred to as 'ultraclean', there is significant valley coupling ($\Delta_{KK'} = 0.4$ meV $> \Delta_{SO}$) present in the device. In my experience, the as-grown fabrication method is effective at reducing long-range disorder, but has no influence on the short-range disorder responsible for $\Delta_{KK'}$.

B.2 Double dot devices

To make more controllable devices with many bottom-gates instead of a global back-gate, several additional processing steps are required compared to the single dot devices described in the previous section. A completed device is shown in Fig. B.3. Here are the steps for fabrication and device screening:

- Fabricate bottom-gate and alignment mark pattern on wafers with at least 300 nm

of thermal oxide on high-resistivity (> 3000 ohm-cm) silicon (the reason for this susbstrate is to enable high-sensitivity dispersive readout as described in Appendix D). 1:1 ZEP:anisole, 2/8/20 nm Cr/W/Pt. These bottom-gates can be written at 2 nA with the Elionix ELS-7000. Deposit bottom-gate bond pads using chlorobenzene photo process, 10/40/85 nm Cr/Pt/Au.

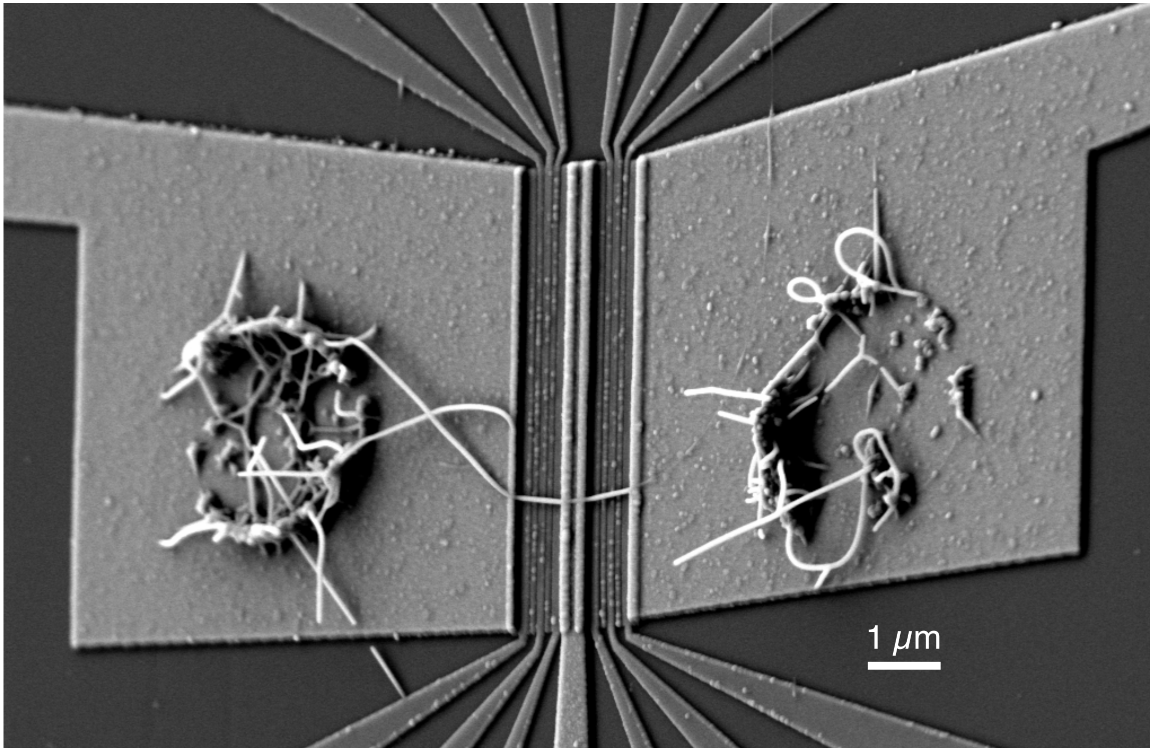

Figure B.3: Carbon nanotube suspended across three SiO_2/W/Pt (Pt on top) contacts to make two separate bottom-gated double quantum dot devices with the same nanotube. The nanotube was suspended over W/Pt bottom-gates and coated with 50 nm of ALD Al_2O_3 immediately following growth. Image: Zeiss Ultra55 SEM, 4 keV, WD 7 mm, SE2 detector, 30 degree tilt.

- Deposit bottom-gate insulator, 40 nm of PECVD SiO_2 (at CNS, use STS rather than Nexx PECVD). Etch insulator off of bottom-gate bond pads, 30 seconds in 5:1 BOE.

- Fabricate contact pattern, SiO_2/W/Pt (no Cr!) 40/10/30 nm, bilayer of 1:1 ZEP:anisole. Deposit contact bond pads, same as for bottom-gates.

- Pattern nanotube catalyst using S1805 photoresist (no chlorobenzene this time)
- Deposit catalyst and grow nanotubes, 15 minutes at 900 C
- Coat nanotubes with ALD Al_2O_3, 50 cycles at 30 C and 400 cycles at 250 C.
- Locate nanotubes bridging contacts with optical microscope, probe at room temperature, and dunk promising nanotubes for characterization at 4 K.

The yield of this process was surprisingly high, with a nanotube bridging two or three contacts about 5-10% of the time. For our experiments, we were interested in small band gap, quasi-metallic nanotubes. Dunking the promising devices at 4 K is recommended because it is difficult to predict low-temperature behavior (precise band gap, dot-lead couplings, noisiness) based on room-temperature back-gate sweeps. For contacts bridged by a nanotube, room temperature conductances range from 0 to about 0.5 e^2/h, which is a convenient upper range since any higher than 0.3-0.5 e^2/h will produce dots that are too open to the leads to be useful for spectroscopy or pulsed gate experiments. A rough rule of thumb for the band gap size is that there should be about a factor of two between the on- and off-state conductances.

These devices are fabricated on high-resistivity (float-zone growth) silicon with a few hundred nanometers of thermal oxide on top. This substrate is a convenient choice because it allows the silicon to be used as a conductive back-gate at room temperature that is insulated from the device by the oxide. The substrate then becomes an insulator at low temperatures (4 K is low enough) that creates a low-capacitance device suitable for dispersive readout.

Design considerations

The dominant failure mode of these devices arose from stray nanotubes causing shorts between contacts and gates and creating devices with multiple nanotubes in parallel. Three process developments were crucial to minimizing the stray nanotube problem: a bottom-gate insulator, optical imaging, and a photolithography process with clean lift-off. First, we developed a process to cover the bottom-gates with an insulator so that nanotubes that lie across a contact and a gate rather than two contacts do not render the gate useless. The challenge was finding a process that would survive the high-temperature nanotube growth environment. Many dielectrics that provided insulation after deposition and contact lithography became leaky after nanotube growth: ALD Al_2O_3 cracked, ALD HfO_2 became conductive, Nexx PECVD SiO_2 and Si_3N_4 became leaky. For the leaky dielectrics, one problem was that we were using a Cr sticking layer for the contact layer that we suspect was diffusing through the dielectrics.

Eliminating the Cr did not fix the Nexx films, but we switched to the STS PECVD tool at CNS and got insulation following nanotube growth with 40 nm thick films of both SiO_2 and Si_3N_4. The final recipe called for SiO_2 because it was easier to etch off of bondpads to aid probing. Developing a working bottom-gate insulator dramatically improved device yield.

Another design feature of these devices enabled by the bottom-gate insulator was that the contacts overlap with the bottom-gates on the left and right sides slightly (~ 100 nm). The reasons were to relax the alignment tolerance between bottom-gate and contact layers, to ensure efficient gating of the nanotube all the way to the contact, and to prevent a situation in which the nanotube makes contact away from the edge of the contact, leaving an un-gateable section of nanotube.

The second tool that improved throughput was the observation that suspended,

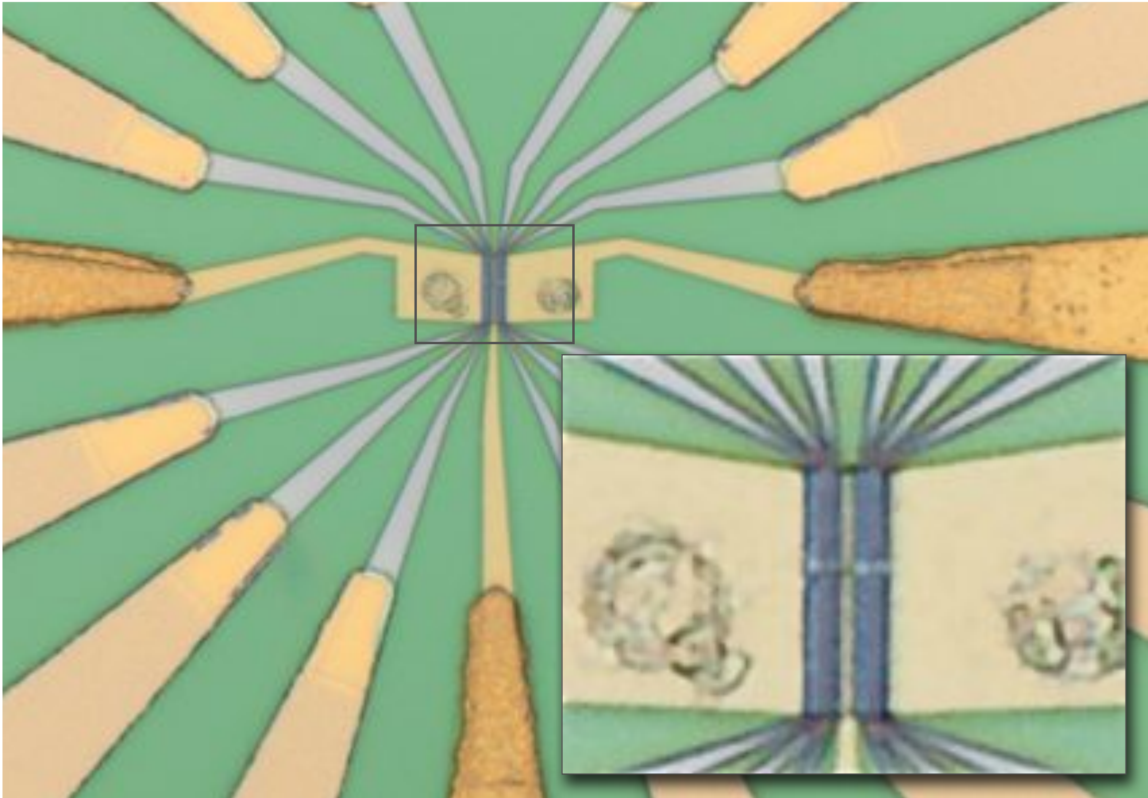

Figure B.4: Optical image of a suspended carbon nanotube double quantum dot device. The nanotube becomes visible after coating with 40-50 nm of Al_2O_3 by atomic layer deposition (ALD).

Al_2O_3-coated nanotubes are visible in an optical microscope (Fig. B.4). Optical imaging allowed us to identify potential devices out of the approximately 1000 candidates on each growth run and also allowed us to eliminate from consideration devices with multiple nanotubes suspended between the contacts (substrate-bound nanotubes between contacts remain invisible). Increasing the ALD Al_2O_3 thickness to 50 nm from 40 nm greatly improved the visibility of the suspended nanotubes. Without this capability, all contact pairs must be probed, and even then, multiple nanotubes in parallel are not apparent until superimposed Coulomb blockade charging patterns become visible at low temperatures.

Third, we developed an improved photolithography lift-off recipe because rough edges at the interface between the ebeam and photo layers were catching nanotube catalyst

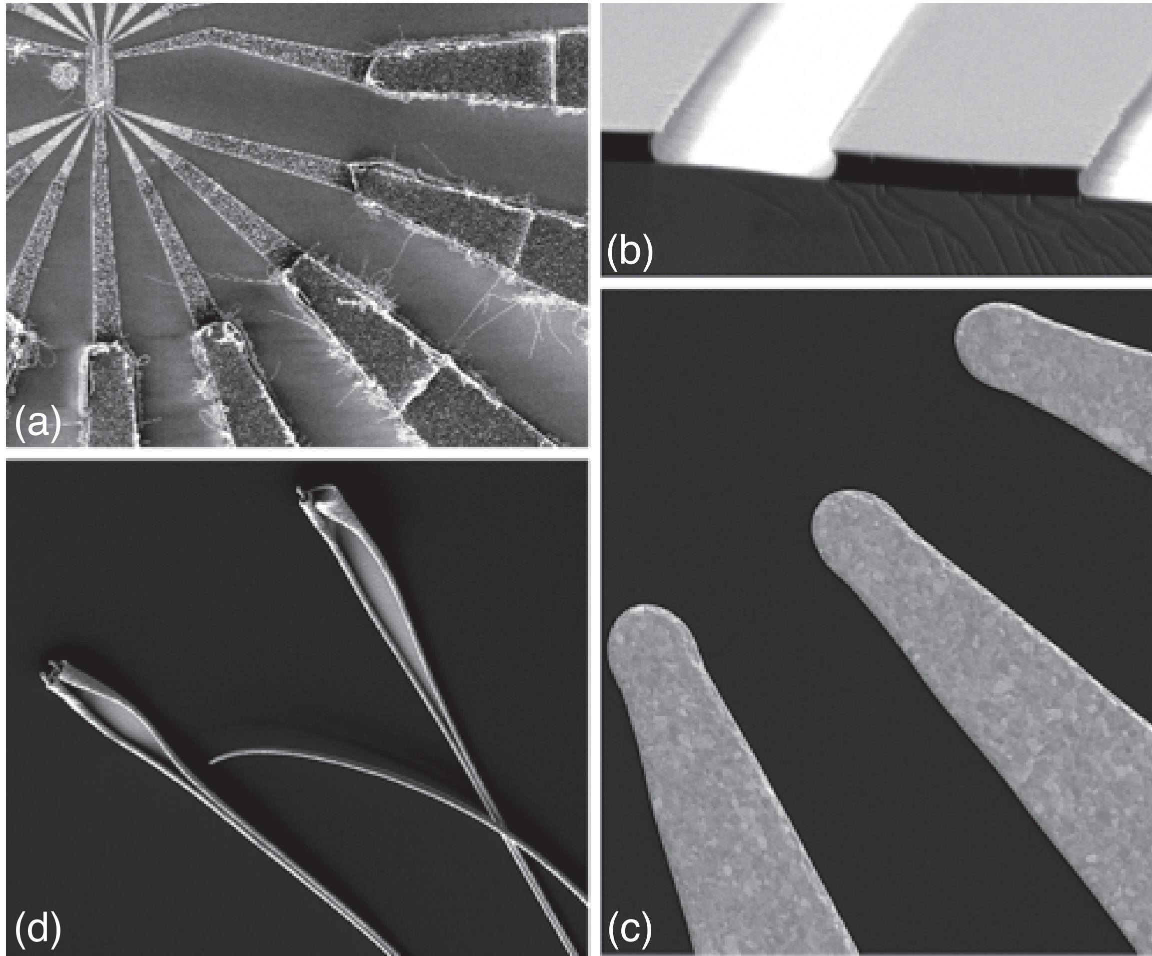

Figure B.5: (a) Regular S1805 photolithography recipe produces jagged edges that catch nanotube catalyst; multiple nanotubes cause shorts. (b) Dipping the exposed resist in chlorobenzene slows the development of the resist at the top, creating an undercut of ~ 200 nm. (c) Metal edges are much cleaner, even after nanotube growth at 900 C. (d) Developing with MF-319 instead of CD-26 causes Cr/Pt/Au contact pads to peel.

and generating lots of nanotubes that caused shorts between contacts and gates as shown in Fig. B.4(a). By dipping the exposed resist in chlorobenzene for four minutes, the top of the resist developed more slowly, creating an undercut of $\sim$ 200 nm [Fig. B.4(b)]. I learned about this process from Ref. [171]; the original reference is Ref. [172]. Lift-off was improved dramatically and catalyst no longer adhered to the edges [Fig. B.4(c)]. In our efforts to improve the process, we tried substituting MF-319 for CD-26 as the developer to improve the sidewall profile. Lift-off seemed fine, but after the nanotube growth process, the bond pads deposited with MF-319 peeled. Presumably the surfactant that is added to CD-26 to make MF-319 leaves behind some scum that is not removed by O_2 plasma.

Here is the complete chlorobenzene photolithography recipe:

- Bake a clean chip for 4 minutes at 180 C.
- Spin Shipley 1805 or 1813 photoresist (probably works for others too) at 5000 rpm for 45 seconds.
- Bake at least 2 min at 115 C (longer makes no difference for our patterns).
- Expose about about twice as long as you would without chlorobenzene (At CNS, 3 seconds when MJB4 intensity is about 25 mJ/cm^2).
- 1 minute post-exposure bake at 115 C.
- 4 minute chlorobenzene soak, blow dry (no DI water rinse, they don't mix).
- 1 minute develop in CD-26, rinse in DI water.
- 10 seconds O_2 plasma at 110 W, 40 sccm (At CNS, use RIE-9).

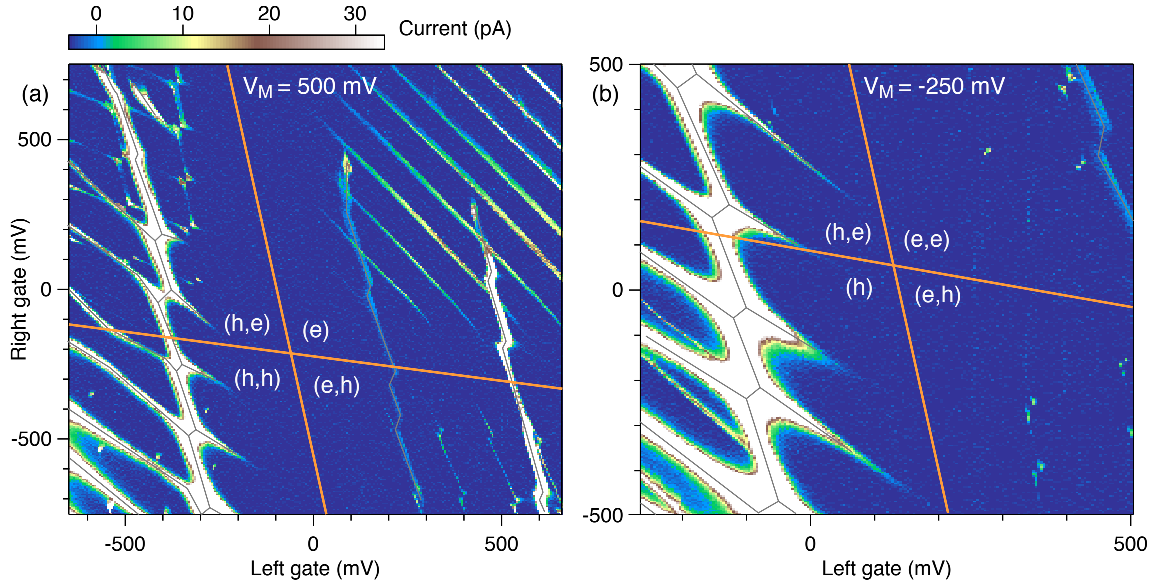

Figure B.6: DC current through two Al_2O_3-coated as-grown nanotubes in parallel as a function of gate voltages controlling the left and right sides of the device. Ignoring the charging pattern of the more strongly coupled nanotube marked with gray lines, the more weakly coupled nanotube shows characteristics of low long-range disorder [27]. (a) For V_M = 500 mV, the nanotube behaves as a double dot for holes (lower left quadrant) and a single dot for electrons (upper right quadrant). (b) Setting V_M = -250 mV changes the device behavior to a single dot for holes and a double dot for electrons. The orange lines denote the position in gate voltage of the middle of the bandgap.

Evidence of low disorder

One concern with this process was whether the ALD Al_2O_3 step (required in our opinion for large level spacing, optical imaging, and efficient gating) to as-grown nanotubes added disorder, rendering the entire effort useless. Based on several of these devices measured at low temperatures, the nanotubes appear to remain quite clean when coated with Al_2O_3 in this way. The best example is provided by a device which, unfortunately, had two nanotubes in parallel (it was fabricated before we began imaging devices optically). Measurements of DC current at 1 mV source-drain bias as a function of gate voltages controlling the charge occupancies of the left and right dots (Fig. B.6) show two superimposed sets of charge transitions, one for each nanotube. One set is strongly coupled to the leads, has

smaller gate couplings factors, and consequently appears as larger, high current features traced with gray lines in Fig. B.6. Ignoring the strongly coupled nanotube, we observe another set of charge transitions with smaller currents and stronger gate couplings resulting in smaller finite bias triangles. For this nanotube, the band gap is clearly identified in both dots as the region where there are no charge transitions, corresponding to zero electrons in each dot (orange lines in Fig. B.6.

Two features of the data in Fig. B.6 demonstrate the sort of low long-range disorder that was the goal of this device design. The first is visible in Fig. B.6(a) as the smooth reduction in current for the electron single dot as the band edge is approached. In more disordered devices many fluctuations of current up and down are observed as the device is pinched off. The second feature of cleanliness was first pointed out as a hallmark of 'ultraclean' devices by Steele *et al.* [27]. Changing the voltage on the middle gate converts the device from a double quantum for holes and a single dot for electrons, to a single dot for holes and a double dot for electrons. Such straightforward, rational control over the dot potential is rarely observed in more disordered devices. Additionally, we note that zero electrons occupy both dots when both the left and right gates are grounded (Fig. B.6), as were the remaining three gates, indicating the small degree to which the ALD Al_2O_3 process dopes the nanotube. In general, locating the few-electron regime and achieving controllable tunnel couplings with the desired number of dots is much easier in bottom-gated, as-grown devices than in top-gated devices, but the procedure is still not routine, mainly because the nanotubes' random bandgap makes it challenging to select appropriate device dimensions.

Appendix C

Manipulation and readout circuit elements

This appendix describes the design and construction of circuit elements developed for the manipulation and readout of charge states of a quantum dot intended for spin qubit applications, including:

- Bias tee evolution
- Printed circuit board designs
- Superconducting spiral inductors
- Lumped element kinetic inductance resonators
- Miscellaneous useful topics: noise, amps, heat sinks, DACs

C.1 Bias tee evolution

For pulsed gate experiments, bias tees are used to add high frequency pulses on top of DC gate voltages. When I joined the lab, we were using Anritsu K251 bias tees, which had excellent high frequency performance but an annoyingly high crossover frequency (50 kHz) between the RF and DC sides, which meant that the pulses would begin to droop significantly after about 10 μs. The droop can be compensated by giving the pulses an inverted high-pass shape, but that scheme only works up to a point given by the maximum output voltage of the waveform generator and is subject to errors from imperfect knowledge of the time constant of the droop.

A better approach is to reduce the crossover frequency to tens of Hz, which is a typical frequency used for slow sweeps of gates in DC transport measurements. A summary of the various schemes we developed to create low-crossover frequency bias tees is shown in Fig. C.1. The first approach was to chop up one of David Reilly's PCBs for RF reflectometry, Fig. C.1(b). In addition to a 10 μF capacitor and two 1 kΩ resistors, it had a 1 mH inductor, chosen to be as large as possible in a surface mount package. However, the resistor by itself presents a sufficiently large impedance to the 50 Ω RF line, so the inductor is unnecessary. This observation was the motivation for deleting the inductor from our bias tee designs, as in Fig. C.1(c). Figure C.2 shows the transmission through a 5 kΩ surface mount resistor of the type shown in Fig. C.1(b) and (c) compared to a 250 nH inductor with an 0603 package size. The resistor outperforms the inductor in blocking RF from entering the DC line, and the much larger 1 mH inductor would be even worse because stray capacitance dominates the transmission. The 5 kΩ resistor does very well up to 5 GHz and continues to do OK up to 15 GHz. Commercial bias tees must use inductors to present a small resistance on the DC side because the DC bias typically provides power—a current normally flows through

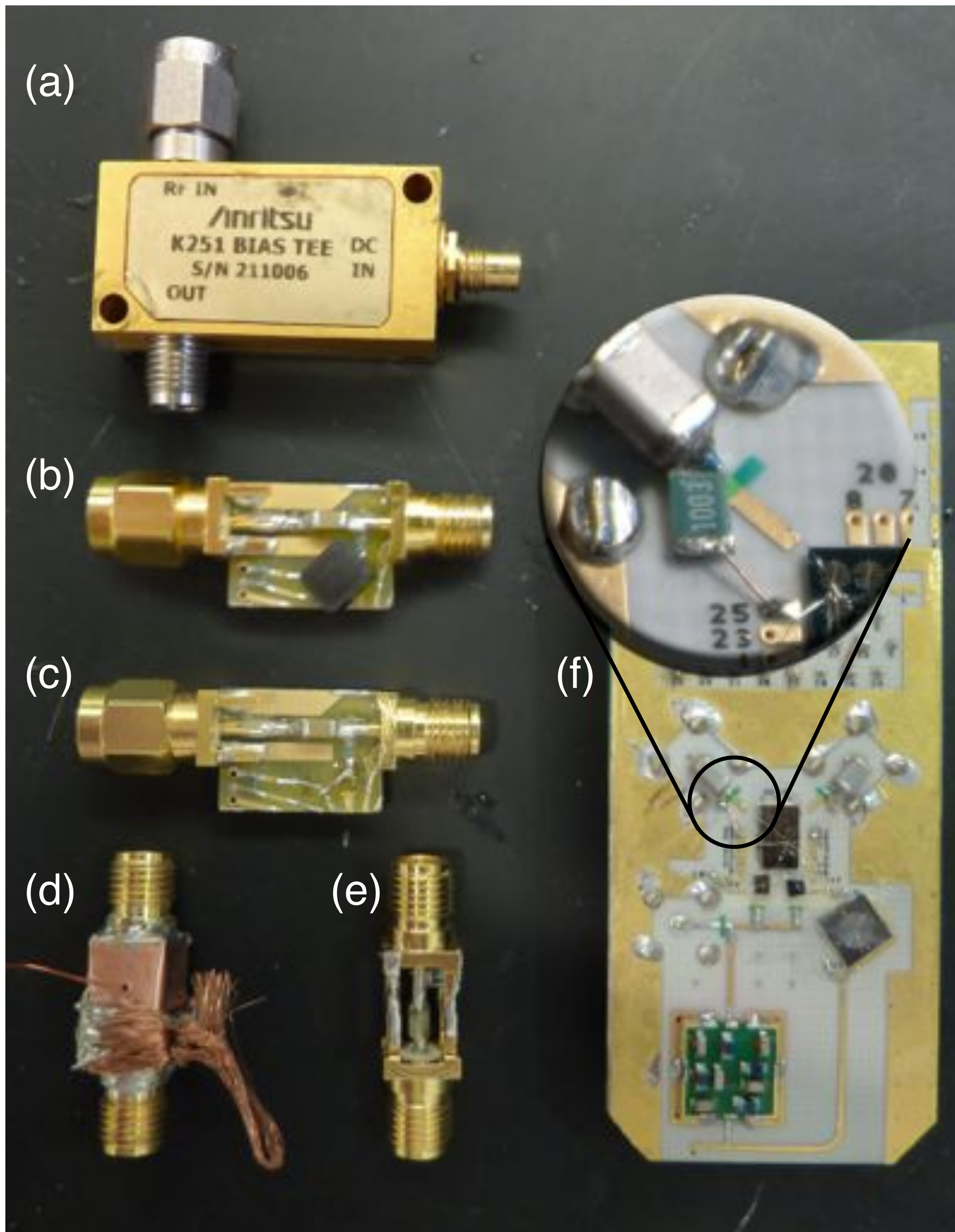

Figure C.1: Evolution of bias tees for high-frequency pulse lines. (a) Anritsu K251: 50 kHz crossover. (b) RLC bias tee: 10 μF, 2 kΩ, 1 mH. (c) same as (b) with no inductor. (d) RC bias tee, 50 kΩ and 1 μF. (e) Same as (d) with cover removed. (f) On-board RC bias tee, 100 kΩ and 100 nF.

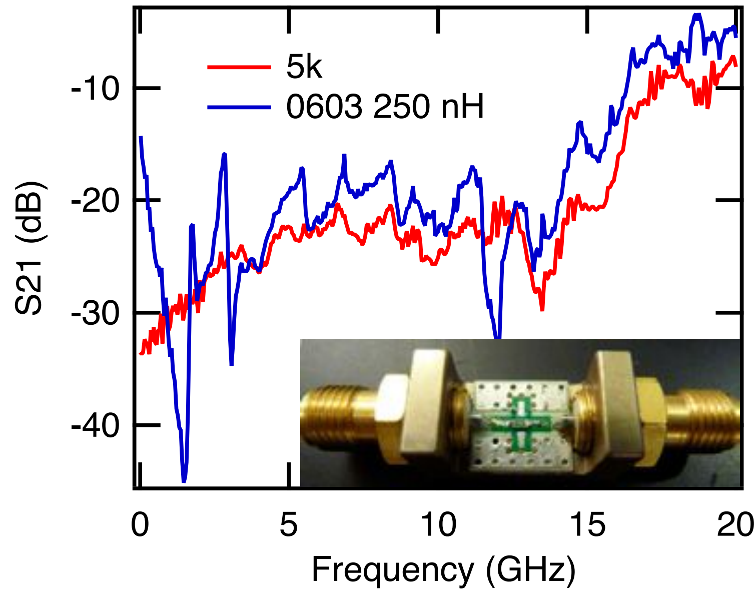

Figure C.2: Comparison of transmission, S_{21}, through a 5 kΩ resistor (Vishay TNPW0603) and a 250 nH inductor (Coilcraft, also 0603 case size). Inset: both were measured on a two-terminal Mini-Circuits test board (resistor shown).

the DC side. In our case no current flows through the gate (one hopes), so a simple RC filter is sufficient.

The bias tees made from chopped up PCBs showed significant resonances in transmission (several dB) above 0.5 GHz, so we developed the RC bias tee design shown in Fig. C.1(d) and (e) which consist of two SMA board mount connectors soldered together with a capacitor placed between the center pins of the connectors. A resistor (tyically 50 kΩ) was soldered to the center pin, perpendicular to the connectors and sticking out between the grounding legs. A wire for DC bias was attached to the resistor, and they were wrapped with copper tape and soldered shut for shielding. The performance of these tees was significantly better than the PCB version, with no resonances larger than a few tenths of a dB up to 6 GHz.

The final version I developed in collaboration with Jim Medford was an on-board

bias tee in which the capacitor created the link between a board-mount SMP connector and a PCB microstrip line. The resistor was soldered directly to the microstrip and connected to a DC line with copper wire. This design has the advantages of being extremely compact, and not interrupting the coax lines in the fridge above the sample. We found no difference in the reflections back from microstrips with bias tees attached compared to those without bias tees.

C.2 Printed circuit board designs

To facilitate dispersive readout of carbon nanotube quantum dots (see Appendix D), printed circuit boards were designed that offered a number of advantages, including ease of assembly, improved high frequency performance, and accommodations for spiral inductors. Photographs of the front and back of one of the boards are shown in Fig. C.3.

Here are some of the details that went into the design of these boards, some of which should be credited to Jim Medford who was redesigning boards for GaAs spin qubits at the same time:

- Six layers (RF/ground/DC/ground/DC/ground, top to bottom), 8 mil Rogers 4003 on outer layers, 50 microinches of soft bondable gold over 1 oz. copper on outer layers with no nickel underplating, tab routing for easy panel separation.

- DC connections are made by attaching a 25-pin Cristek micro-D connector, which greatly reduces board assembly time.

- RF and pulse lines used SMP connectors (limited detent type) so the board can be quickly and easily mounted to the fridge.

- The DC and RF connectors are mounted on the back to avoid interference with

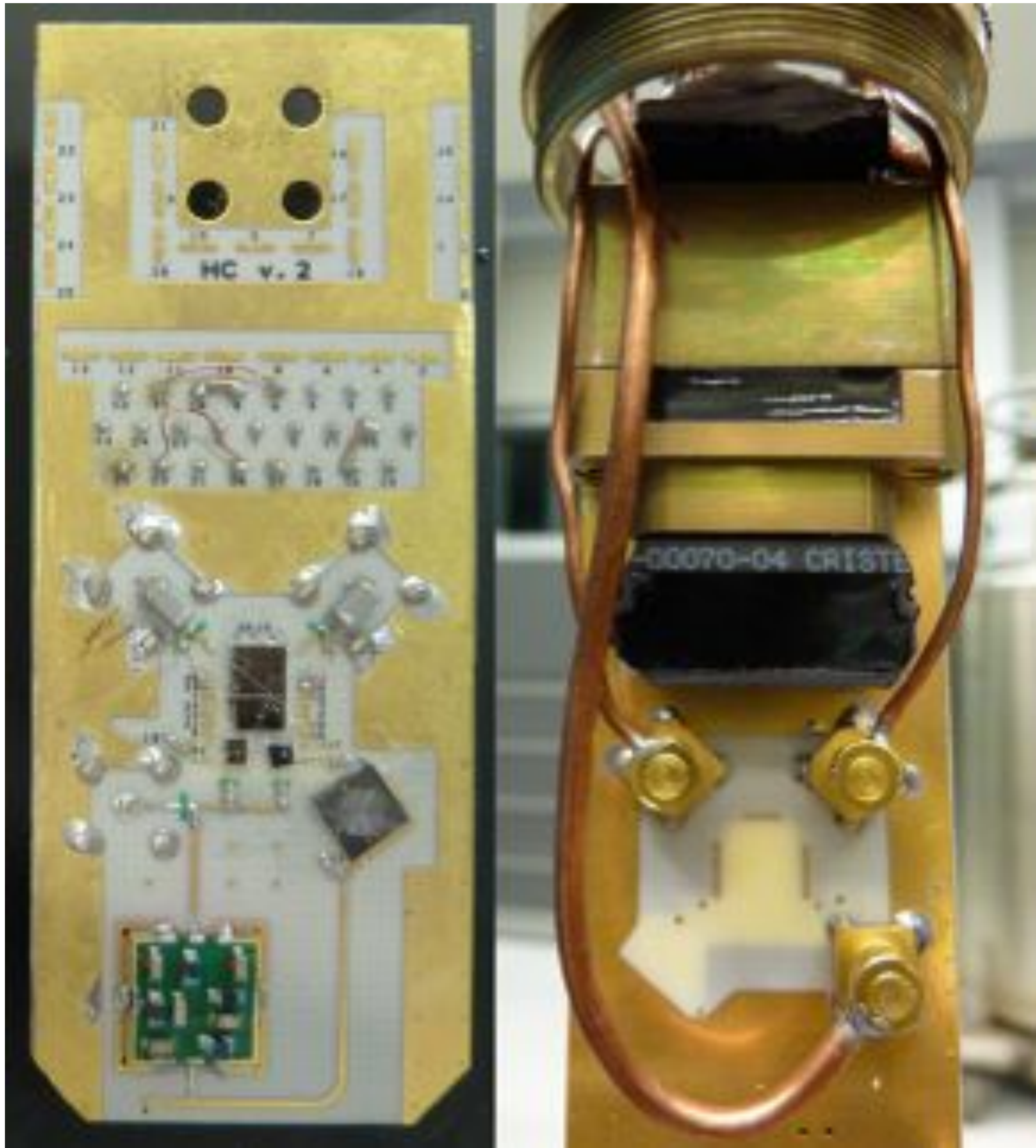

Figure C.3: Front and back photographs of printed circuit boards designed for 25 DC lines, 2 pulse lines, and up to three superconducting resonators (two small and one large). DC connections are made via a Cristek 25-pin micro-D connector and high frequency connections are made with SMP connectors and 50 Ω microstrips.

wirebonding.

- At the top on the front side there are pads for a filter capacitor (typically 10 nF, C0G dielectric, ATC non-magnetic) to ground for each DC line. For faster assembly, these were replaced by custom Glenair non-magnetic micro-D filters (also 10 nF C0G), shown in Fig. C.3 above the black Cristek connector.
- The ground planes are cut away beneath the sample and beneath the resonators to reduce parasitic capacitance, visible in the rear view of Fig. C.3 where the light shines through the center of the board, making it appear yellow.
- Microstrips for the pulse lines and high frequency resonator lines were made as short as possible.
- A Mini-Circuits RLP-83 low-pass filter was added (front side, lower left) to separate the high and low frequency resonators (more details are given in Appendix D).
- Numerous vias were placed wherever possible to create low inductance ground planes and reduce spurious resonances.
- Almost no soldermask was included for flexibility in component placement. Exceptions (front side, green strips) were places where capacitors were soldered to microstrips to block solder from covering wirebond areas.
- A topside silkscreen (black) was used to number the DC lines. The convenience more than compensated the aesthetic downside.
- The DC bond pads should be made longer than in this design for more convenient wirebonding.

These boards had Rogers 4003 laminate on the outer layers. We do not know if this high-frequency material actually helps for our applications, but compared to FR-4 it has lower losses and a much smaller change in dielectric constant with temperature. The price per board for Rogers is about twice as much, but because of the largely quantity-independent nature of PCB prices, it is possible to get Rogers boards for only about 10% more than FR-4 boards and still end up with many more boards than needed. The inner layer materials were selected to give a total thickness of about 0.05", which is thick enough not to bend during wirebonding (this was a problem with the first generation boards which were thinner). Boards were ordered from Advanced Circuits and R&D Circuits, both of which were willing to provide nickel-free boards with some persuasion.

Samples and resonators were attached to the boards using MicroChem EL-6 MMA that was concentrated to a higher viscosity by heating with the lid off at 80 C until the volume was reduced by about 75%.

C.3 Superconducting spiral inductors

Dispersive readout benefits from having the smallest possible stray capacitance in the circuit. With devices fabricated on insulating substrates and ground planes removed from under the device and under bondwires, most of the remaining stray capacitance (typically 0.1-0.2 pF) came from the chip inductors used for the tank circuits. The way to reduce this capacitance is to make smaller inductors, but reducing the size of the wires defining the inductor increases their resistance, and eventually the Q of the inductor becomes intolerably low. The solution is to eliminate the resistance of the inductors by making them out of a superconducting material. The best material for this application is NbN because its large superconducting gap can tolerate the large magnetic fields of spin qubit applications, and its

large kinetic inductance reduces the size required for a given inductance. The characteristics of these spirals are described in more detail in Appendix D, so only the fabrication steps are given here. To design the spirals, I used the 'spiral' function of SolidWorks, exported a DXF file, and imported it into DesignCAD, which was extremely inefficient. Jim Medford modified the Archimedes Spiral DesignCAD macro to make nice spirals for resonators. The macro is available on the Marcus Lab Wiki.

There are two basic ways to make these spirals: etching and lift-off. Lift-off is the simplest because only two steps are required (patterning and deposition), but etching provides higher quality films with larger critical temperatures since the lift-off process allows impurities from the resist to be incorporated into the NbN film. This problem can be reduced somewhat by sputtering a 5 nm layer of Ti first that coats the resist.[1] The Ti step is required for photoresist patterned spirals and nearly required for ebeam resist patterns (it occasionally works without the Ti). In both cases, the spirals should be patterned on high-resistivity silicon substrates, with or without SiO_2 on top, though higher Q (> 1000) resonators on bare silicon seem to outperform their counterparts on SiO_2. The steps for both processes are provided below.

Patterning spirals by lift-off

NbN is deposited by sputtering Nb in the presence of Ar and N_2, usually at a pressure of a few mTorr. Because of the high pressure compared to evaporation, the sputtered material diffuses somewhat, making lift-off more difficult. Bilayer resist processes—in which a more sensitive resist is placed under a less sensitive resist to create an undercut—are therefore essential. Doug McClure taught me about the MMA/ZEP combination that works

[1] Cr should not be substituted in this case because its antiferromagnetism can weaken superconductivity in the layer above.

extremely well for lift-off of sputtered films, even in the CNS AJA SP-2 which deposits material at a very oblique angle. We used MicroChem EL-6 MMA and 1:1 ZEP:anisole using ZEP520A from Zeon Corp. Here is the recipe:

- Standard clean, then pre-bake 2 minutes at 180 C.
- Static dispense EL-6, spin 5 seconds at 500 rpm, then 45 seconds at 5000 rpm (EL-6 is about 100 nm thick when spun at this speed).
- Bake 4 minutes at 180 C.
- Spin and bake 1:1 ZEP:anisole in the same way as EL-6.
- Expose spiral pattern. On the Elionix ELS-7000, the parameters are 10 nA beam current, aperture 3, 150 μm chip size, 5k dots [20k with (4,4) pitch], 0.5 μs dose.
- Develop 20 s in o-xylene, 40 s in 1:3 MIBK:IPA, rinse in IPA
- In the Marcus Lab system, do a Cr or Ti sweep and wait 10 minutes or so for the pressure to bottom out.
- Presputter the Nb and Ti targets for 1 minute, then sputter 5 nm of Ti at 200 W, 4 mTorr, 50 sccm Ar, followed by 100 nm of NbN at 250 W, 4 mTorr, 50 sccm Ar, 6.5 sccm N_2. On the Marcus Lab system, run the process 'Ti-NbN 5nm-100nm'.
- Lift-off in 1:1 acetone:TCE, rinse in acetone, then IPA.

Patterning spirals by etching

In the etching process, a NbN film is deposited globally on the sample, an Al hard mask with the spiral pattern is deposited, the NbN is dry etched, and the Al mask is removed in a wet etch. Here are the steps:

- Standard clean, then 1 minute O_2 plasma clean at 110 W, flow of 40 sccm. The tool at CNS is RIE-9, an Anatech SCE 106 barrel asher.
- Deposit 100 nm of NbN (no Ti required this time). Begin with Cr or Ti sweep on Marcus Lab system as above.
- Pattern resonators in EL-6/ZEP as above for lift-off process, develop as above, deposit 40 nm of Al by ebeam evaporation. Lift-off in 1:1 acetone:TCE.
- Etch NbN by RIE: 30 sccm CF4, 3 sccm O2, 250 W microwave, 40 W RF, 5 mTorr. 120 seconds is enough for 100 nm. This recipe is for RIE-6 at CNS, a Nexx Cirrus 150 ECR RIE.
- Remove the Al mask by etching for 2 minutes in Transene Al etchant, Type A, room temperature. This etchant is gunky so rinse thoroughly, then do a standard clean. If the resonator has a silvery color like Al rather than the light, dull brown characteristic of NbN, etch longer.

C.4 Lumped element kinetic inductance resonators

Spiral resonators are a good design for off-chip elements, but to put a resonator on-chip, it must be made smaller given the limited space available on chips for as-grown nanotube devices. The way to shrink the resonators is to make a superconducting meander with a small cross-section so that the meander has a large kinetic inductance. The kinetic inductance of a superconducting wire can be calculated (as in Ref. [173] for example) by rewriting the kinetic energy of the Cooper pairs as an inductive energy: $(nAl)mv^2 = \frac{1}{2}L_K I^2$, where n is the Cooper pair density, A is the cross-sectional area of the wire, l is its length, $2m$ is mass of a Cooper pair, v is their velocity, L_K is the kinetic inductance, and $I =$

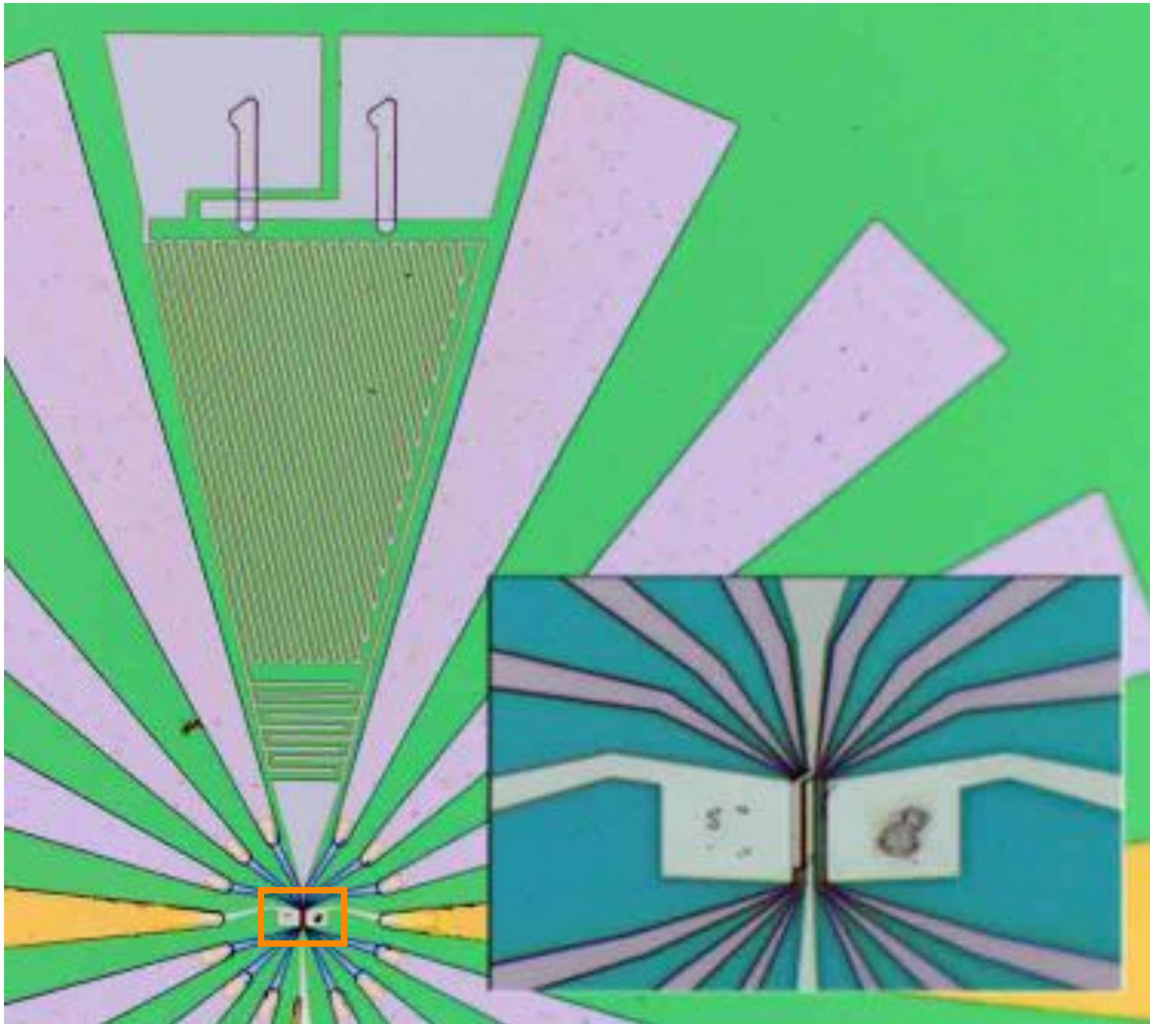

Figure C.4: Optical micrograph of a lumped element kinetic inductance resonator fabricated on top of an as-grown carbon nanotube double quantum dot device. The inset (lower right) is a zoom-in of the region within the orange box. This resonator design is not optimized but represents the general concept.

$2nevA$ is the supercurrent flowing through the wire. The kinetic inductance is then $L_K = \left(m/2ne^2\right) l/A$. To maximize kinetic inductance, then, the wire should be long, thin, narrow, and have a low density of Cooper pairs (or, equivalently, a long London penetration depth, a large normal state resistivity, or near-critical temperature or magnetic field). NbN has a particularly low Cooper pair density and large normal state resistivity and is therefore a particularly good kinetic inductor.

These resonators can be fabricated in the same ways as the spiral resonators described above. The idea is that they would be incorporated into the device design from the beginning, in which case etching would be preferable, but they could also be deposited on top of an existing device, which would require lift-off. An example of this is shown in Fig. C.4. This design is not optimized but shows the basic idea. A resonator of this design (but not on top of an existing device) with a 5/100 nm Ti/NbN film and 1.5 μm wide traces resonated at about 1.25 GHz with a Q of a few hundred at 4 K.

C.5 Miscellany

C.5.1 A quantitative benchmark for 60 Hz noise

Many theses provide grounding advice for reducing noise in low-frequency transport measurements. I will not provide any such advice; instead, I will define a unit of 60 Hz noise, the kuemmeth,[2] that is intended to help future students decide when enough is enough while searching for ground loops. One kuemmeth (1 Kü) equals a peak height of 1 μV measured with a spectrum analyzer connected to the X1 output of an Ithaco 1211 current preamplifier set to 10^{-8} A/V sensitivity which has its input connected to a quantum dot in deep Coulomb blockade.

[2] Its small magnitude indicates that this unit is honorific rather than defaming.

If low electron temperature is the goal, maximum peak heights (at 60 and 180 Hz, for example) of 300 Kü are sufficient for an electron temperature of 30 mK as measured by Ferdinand in the Vericold fridge. If the 60 Hz is in that ballpark, the electrons are most likely not being heated by ground loops. If a low noise transport measurement is the goal, the lower the better. The DC current measurements in Ch. 3 are particularly low noise by Marcus Lab standards, with an RMS current noise of 10 fA with an Ithaco time constant of 100 ms. The Stanford fridge at its quietest benefitted from a relatively small capacitance seen by the input of the Ithaco because there were no RC filters on the DC lines other than cold resistors and the loom capacitance, but that setup also had very low 60 Hz noise. The harmonics had peak heights of 70, 40, and 30 Kü for the 60, 120, and 180 Hz harmonics respectively. Students in the new lab in Denmark should have no problem achieving a 120 Hz peak much lower than 40 Kü.

C.5.2 Homemade low-noise cryogenic amplifiers

A liberating change in Marcus Lab fast readout technology came with the decision to purchase broadband (CITLF1, .001-1.5 GHz, 45 dB gain, $T_N = 3$ K) cryogenic amplifiers from Sander Weinreb's group at Caltech to replace the narrowband ($\approx$ 200-250 MHz) Quinstar amplifiers we had been using. However, the lead time for the Weinreb amps was quite long so I made a similar one based on Ref. [174], taking advantage of extraordinarily generous instructions (including a bill of materials and machine shop drawings) from Karl Petersson. A picture of the completed amplifier is shown in Fig. C.5. I never measured the low temperature noise temperature, but at room temperature, the noise temperature was about 100 K according to the Y-factor method [175], comparable to that in Ref. [174], and the S-parameters at 4 K were also similar.

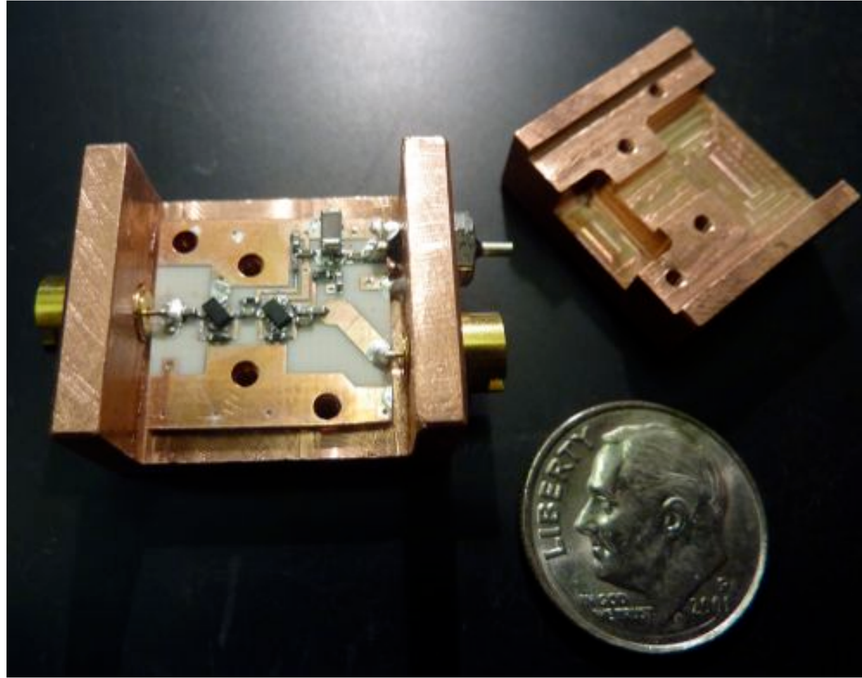

Figure C.5: Low-noise cryogenic amplifier built according to Ref. [174] and Karl Petersson's instructions.

C.5.3 Sapphire coax heat sinks

Soon after I began using the fridge David Reilly wired for fast readout, the sapphire heat sink at the still made by Leo DiCarlo shattered, and I had to make a new one (two, eventually, since the homemade cryoamp and Weinreb CITLF1 caused unacceptable heating unless a second one was added at the mixing chamber). The ones I made had a microstrip design (400 μm wide) using a single 0.5 mm thick piece of sapphire (University Wafer). These were much easier to construct than the stripline design with two sapphire slabs because it is difficult to get the top sapphire piece to sit neatly on top of the SMA center pin. The lid of the box was designed by Angela Kou to provide even pressure on the sapphire piece to prevent breaking and thermal failure in the common event of cracked silver epoxy. The SMA connectors were selected to have center pins with diameters close to the microstrip width to improve impedance matching. The pins were soldered to the

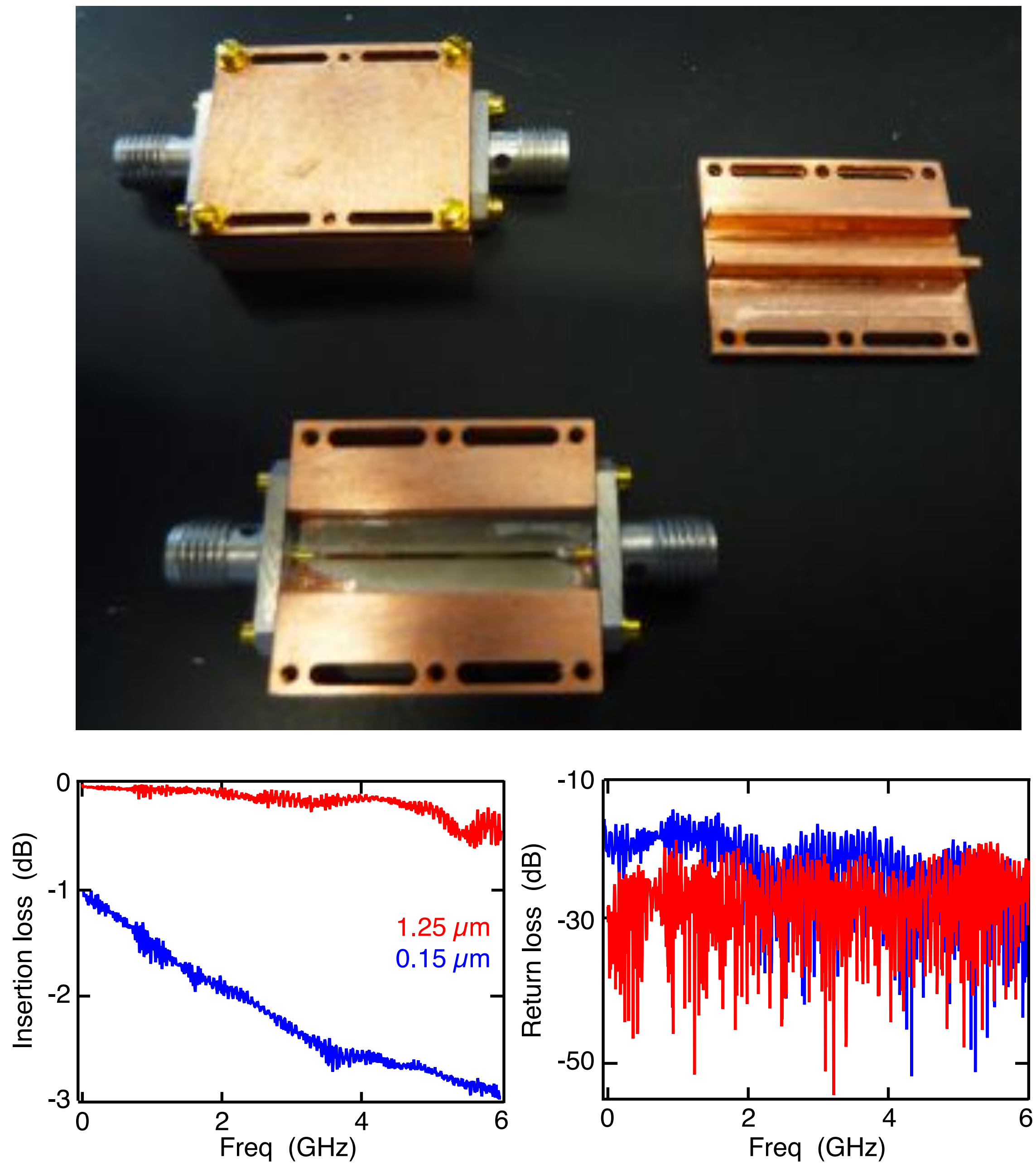

Figure C.6: Gold microstrip (1.25 μm thick, 400 μm wide) on 0.5 mm thick sapphire, attached to a copper box (lid design by Angela Kou) by silver epoxy (Epo-Tek 4110) for heat sinking readout coax. Lower panel: insertion and return loss for the sapphire box shown. A rather thick Cr/Au film must be used to limit losses.

microstrip with regular tin/lead solder.

Insertion and return loss measured at 4 K for one of two sapphire boxes I made is shown in Fig. C.6. A thick film (50/1250 nm) of Cr/Au had to be used to make the losses acceptably small (red in Fig. C.6). A 5/150 nm Cr/Au of the same design (blue in Fig. C.6) was not perfectly matched and attenuated more than 1 dB of precious, un-amplified signal even at low frequencies, and would have reflected 10 dB more RF back down to the sample.

C.5.4 Look-up table DAC calibration

Careful calibration of DAC channels is important for taking data that is free from junky looking digital artifacts, particularly when compensating a charge sensor to stay on a narrow Coulomb blockade peak. The standard procedure is combine two channels on a single gate in a coarse/fine configuration. For a long time our code used all 16 bits of the coarse channel, then used the fine channel to fill in the gaps. A better approach is to use the full range of the fine channel because the unavoidable errors in the DAC output are reduced by a factor of the fine-channel divider (100 in my case). In the best case, this technique would reduce the errors to $0.2\ \mathrm{V}/2^{16} \sim 3\ \mu\mathrm{V}$, but despite the best efforts of the manufacturer, all the bits of the DAC are not created equally, and big jumps can occur when a large number of the bits roll over (from 0111... to 1000...).

Because the coarse channel is only used for 32 discrete values, a better approach is to measure the voltages associated with each of those bins, make a look-up table that provides the best coarse bin for a desired voltage, and use the fine channel to make up the difference. This technique reduced all residuals of a linear fit to the DAC output below 10 μV, and the remaining errors could be nearly[3] eliminated by carefully calibrating the slope

[3]Nearly, because of a few μV nonlinearity in the fine channel that would require its own lookup table to remove.

of the fine channel so that consecutive coarse bins are stitched together accurately. The results are summarized in Fig. C.7. No code is included because it seemed not to be easily incorporated in other setups.

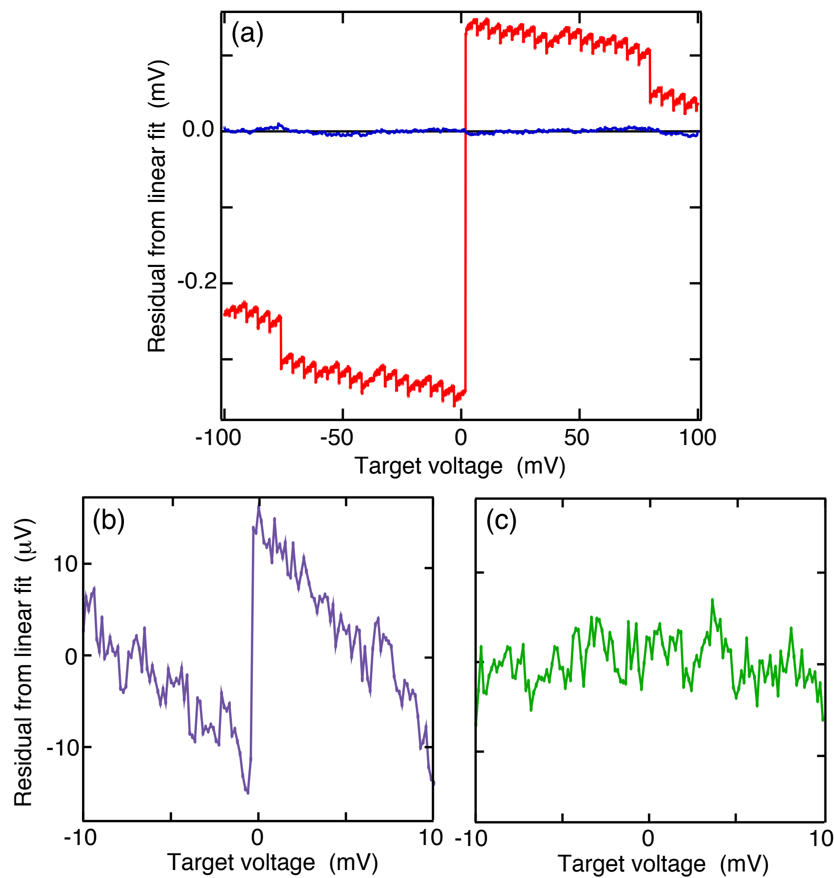

Figure C.7: (a) Comparison of former code (red, mostly coarse channel) with newer code (blue, mostly fine channel). (b) Further improvement by using a lookup table for each of 32 coarse bins. (c) Remaining jumps removed by calibrating the slope of the fine channel. Note vertical scale is 20x smaller in (b) and (c).

Appendix D

Superconducting spirals for dispersive readout of quantum dots

D.1 Introduction

Some means of detecting charge transitions for spin-state readout is required to make the devices described in Appendix B attractive as potential spin qubits. In a dispersive readout scheme, the frequency shift of a resonant circuit is detected in response to a change in the state of the device of interest that modifies the capacitance or inductance of the resonator. This technique is common in the field of superconducting qubits [176] and has more recently been applied to spin qubits by attaching a resonant circuit directly to one lead of a quantum dot [169]. In the context of this thesis, using dispersive readout for charge detection allowed us to embrace a fully as-grown fabrication technique and abandon the dedicated charge sensors that dominated the complexity of our earlier devices.

An on-chip resonator for dispersive readout of quantum dots was demonstrated by Frey *et al.* [177]. Due to the large size of coplanar waveguide resonators, the technique used

in Ref. [177] is incompatible with semiconductor quantum dots based on materials for which device yield is inherently low because the placement of quantum dots is largely uncontrolled, as in the case of nanowires and carbon nanotubes. One solution is to grow nanotubes in the vicinity of a pre-patterned resonator, followed by an additional lithography step to add leads and gates to the device [178]. To take advantage of the cleanest, as-grown devices, a fruitful approach is to attach resonant circuits to devices after successful ones have been fabricated and located. Another advantage of this method is that dispersive readout can be performed on devices not specifically designed for that purpose. An off-chip resonant circuit was used by Petersson *et al.* by wirebonding a lumped element LC tank circuit to one lead of a GaAs double quantum dot [169]. This technique was also applied to a carbon nanotube double dot by the same group [179]. However, tank circuits provide limited sensitivity in a dispersive readout scheme because the stray capacitance of the circuit is dominated by the normal metal conductor that forms the inductor, and because quality factors are limited to $Q < 100$. Here we describe a compromise between the flexibility of an off-chip method and the sensitivity of an on-chip superconducting resonator, by coupling superconducting spiral resonators to the leads and a gate of a carbon nanotube double quantum dot device.

D.2 Spiral and quantum dot fabrication

Superconducting spiral resonators (shown in Fig. D.1) were fabricated by depositing a 100 nm film of NbN on 500 μm thick silicon substrates ($\rho = 3000\ \Omega\cdot$cm) at room temperature by reactive DC sputtering of Nb with 12% N_2 in Ar. Spirals were patterned by electron beam lithography, and 40 nm of Al was deposited by electron beam evaporation to serve as a hard mask for reactive ion etching of the NbN using CF_4 and O_2. The Al mask was removed by etching in Al etchant (Transene Type A). Films prepared in this way have

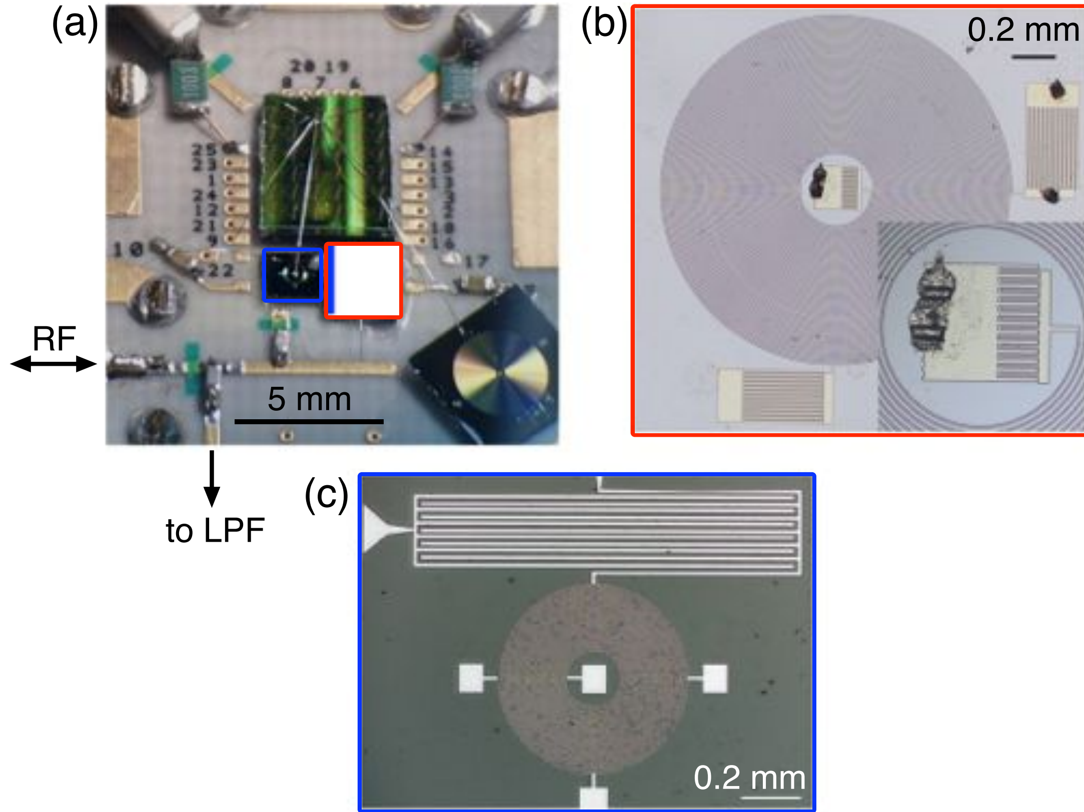

Figure D.1: (a) Board layout for dispersive readout circuit. The RF excitation was applied as indicated to the microstrip feedline, where it branched via wirebonds to one end of two higher-frequency spirals [one higher Q (b) and one lower Q (c)] and a lower frequency spiral through a low-pass filter. The other ends of the spirals were connected to the sample (green, center) by wirebonds.

$T_C \sim 12$ K. More details of spiral fabrication are provided in Appendix C.

The spirals were used to readout the charge states of carbon nanotube quantum dots. The nanotube devices were fabricated on $\rho = 3000\ \Omega{\cdot}$cm silicon substrates with 400 nm of thermal SiO_2. W/Pt bottom-gates and contact patterns were patterned by electron beam lithography. Alumina-supported $FeNO_3$ and Mo catalyst was deposited on the contacts, and suspended carbon nanotubes were grown across the contacts by methane CVD at 900 C [Fig. D.2(a)]. More details of nanotube device fabrication are provided in Appendix B.

D.3 Spiral characterization

The quantum dot device and resonators were mounted on a PCB [Fig. D.1(a)] in a dilution refrigerator with a base temperature of 30 mK and an electron temperature of 100 mK. In a typical arrangement, three resonators were placed on the board, and one resonator was attached by wirebonds to each lead and the third to a bottom-gate. In the board design, the ground plane was omitted underneath the resonators and the sample to minimize stray capacitance. The inductances $L = L_G + L_K$ of these superconducting spirals are dominated by a geometrical term, L_G, with a smaller kinetic term, L_K. L_G was calculated according to Ref. [180][1], and L_K was estimated based on Ref. [173][2]. Capacitances of the resonators, C, (when coupled to the quantum dot) are calculated from the resonant frequency and the inductance via $f_0 = 1/2\pi\sqrt{LC}$. The resonator coupled to the left lead of the device [$R1$, blue in Fig. D.1 and D.2] had an outer diameter of 600 μm, 40 turns with 2 μm wide lines separated by 2 μm gaps with a total length of 4.9 cm, $f_0 = 415$ MHz, loaded quality factor $Q = 50$, $L_G = 850$ nH, $L_K = 120$ nH, and $C = 0.15$ pF. The resonator coupled to the middle gate of the device [$R2$, red in Fig. D.1 and D.2] had an outer diameter of 1.65 mm, 60 turns with 4 μm wide lines separated by 7 μm gaps with a total length of 13.1 cm, $f_0 = 225$ MHz (the second harmonic at 453 MHz shown in Fig. D.2(b) was used), $Q = 1000$, $L_G = 3.1$ μH, $L_K = 150$ nH, and $C = 0.15$ pF. The quality factor was larger for this resonator because it was decoupled from the feedline with an interdigital capacitor, $C \sim 0.1$ pF. An additional decoupling capacitor on the sample side of this resonator was not used. The resonator coupled to the right lead of the device [$R3$, lower left in Fig. D.1(a)

[1] More conveniently: `http://www.circuits.dk/calculator_planar_coil_inductor.htm`

[2] Ref. [173] estimates 0.6 pH$\cdot\mu$m for NbN at $T \ll T_c$, which can be used to estimate a kinetic inductance for a given spiral or meander by multiplying by the length of the resonator and dividing by the cross-sectional area of its traces. We found this estimate to hold approximately for NbN meanders fabricated by us (see §C.4).

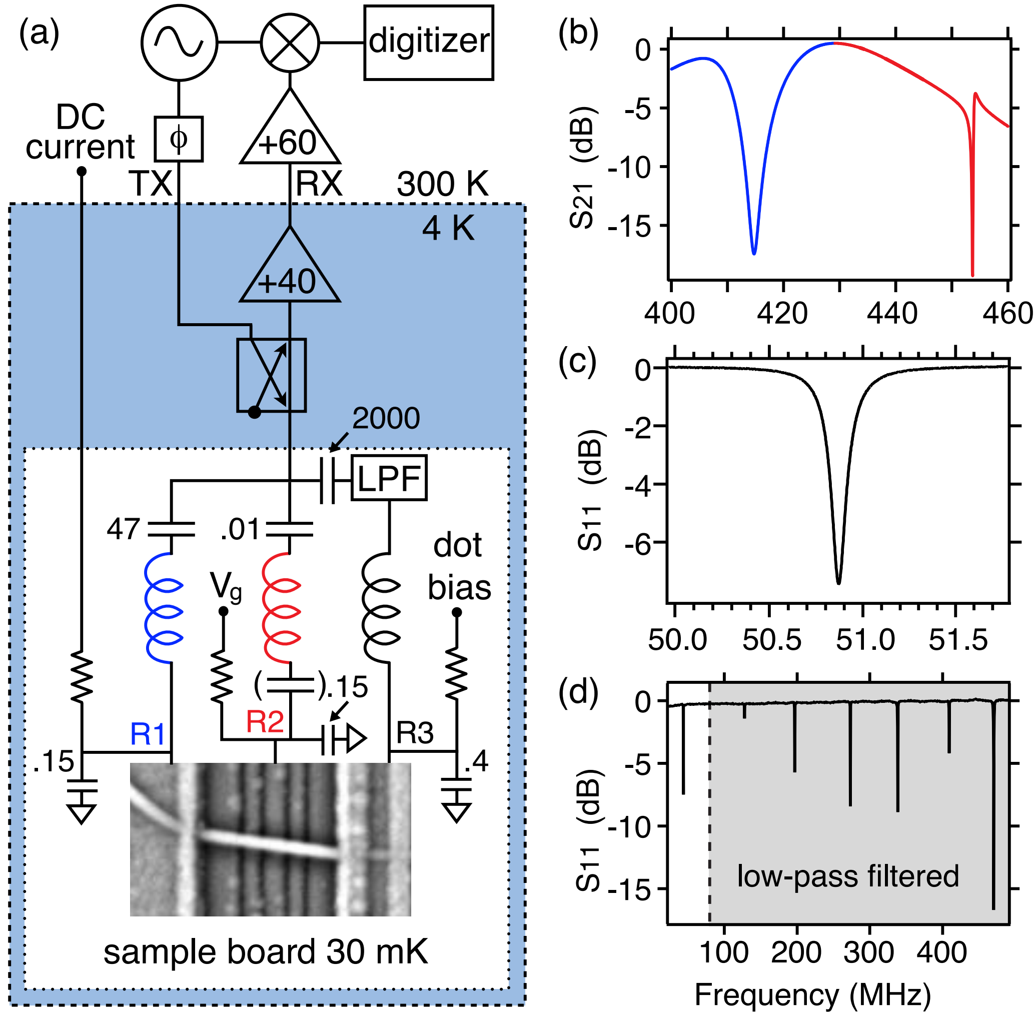

Figure D.2: (a) Schematic of measurement circuit for dispersive readout. A signal generator provided an excitation resonant with one of three spirals, that was phase-shifted, attenuated (not shown), and sent to the sample through a directional coupler. Three resonators were attached to the sample, one to each lead and one to a gate electrode. The reflected signal passed back through the coupler, was amplified at 4 K and room temperature, mixed with the original excitation, and the demodulated response, V_{RF}, was digitized. On-board bias tees allowed DC current measurements. Resistance values are 10 kΩ, and capacitances are noted in pF. Not shown: multiplexed readout was possible by adding additional copies of all room temperature components and combining and splitting, respectively, the input and output to the cryostat. (b) Transmitted power, S_{21}, measured with a network analyzer connected to the RF ports of the cryostat at 30 mK showing the response of the two smaller spiral resonators [blue and red inductors in (a), blue and red boxes in Fig. D.1(a)], see text. (c), (d) Reflected power, S_{11}, of the larger spiral measured with a network analyzer by dunking the sample board in liquid helium. Because of the many harmonics of this resonator near the frequencies of the other two, it was isolated from the others with a low-pass filter [see Fig. D.4(a)].

and black in Fig. D.2] had an outer diameter of 3.19 mm, 130 turns with 4 μm wide lines separated by 7 μm gaps with a total length of 72 cm, $f_0 = 50.9$ MHz, $Q = 300$, $L_G = 22$ μH, $L_K = 800$ nH, and $C = 0.4$ pF. The reason for the low frequency spiral is that, as pointed out in Ref. [169], this readout technique becomes insensitive to charge transitions when the tunnel rate onto the quantum dot becomes slower than the frequency of the resonator.[3]

The resonant frequencies of $R1$ and $R2$ [Fig. D.2(b) and (c)] were measured with a network analyzer connected to the TX and RX ports of the cryostat indicated in Fig. D.2(a) at base temperature, and the reflectance data shown for $R3$ in Fig. D.2(d) were measured at 4 K with a simpler circuit (only a coaxial cable and the sample board). The resonant frequencies of the spirals were approximately what would be expected for quarter-wave resonators on a semi-infinite silicon substrate with effective dielectric constant approximately 6.5 [181]. This approximation gives 590 MHz for $R1$ (f_0 = 415 MHz as measured), 220 MHz for $R2$ (f_0 = 225 MHz), and 40 MHz for $R3$ (f_0 = 50 MHz).[4] Because of the many harmonics of $R3$ near the resonant frequencies of $R1$ and $R2$, an 83 MHz low-pass filter (Mini-Circuits RLP-83) was added [shown in Fig. D.4(a)] to separate the lower and higher frequency resonators.

D.4 Dispersive shift due to quantum dot charging

To measure the response of the resonators to the quantum dot device, reflectometry measurements were made in a standard configuration [Fig. D.2(a)] in which a signal generator provides an excitation, resonant with one of the three spirals, that is phase-shifted,

[3] For the small bandgap nanotube device considered here, however, the tunnel rates were never slower than 50 MHz, so the low frequency was unnecessary and its larger capacitance reduced its sensitivity.

[4] Lower frequencies than expected could arise from a combination of stray capacitance and kinetic inductance; the higher frequency of $R3$ might have resulted from a short between turns that reduced the length of the spiral, but no such short was visible in an optical microscope.

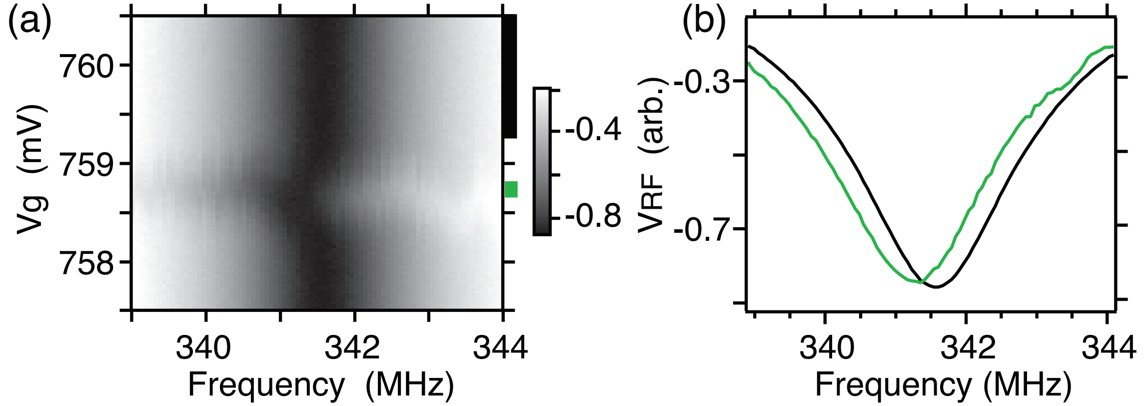

Figure D.3: (a) Demodulated response V_{RF} as a function of gate voltage V_g and RF excitation frequency. A shift in the frequency of the resonance dip is visible when the gate voltage causes a charge transition in the double dot. (b) The green (black) curves are averages of horizontal slices of (a) over the range indicated by the green (black) bar on the right vertical axis of (a). The ~ 0.5 MHz dispersive shift between the green and black curves is the basis for the measurements presented in this chapter. At fixed excitation frequency, the shift results in changes in V_{RF} in response to charge transitions of the double dot.

attenuated (not shown), and sent to the sample through a directional coupler [182]. The signal reflected back from the resonators, passed back through the coupler, was amplified at 4 K (CITLF1 from Weinreb group at Caltech, 40 dB gain, 3 K noise temperature) and room temperature, mixed with the original excitation, and the demodulated response, V_{RF}, was digitized (AlazarTech ATS9350). This technique is demonstrated for a fourth resonator, $R4$ (coupled to left lead in a separate cooldown, not shown in Fig. D.1), in Fig. D.3(a) which shows V_{RF} as a function of excitation frequency and gate voltage, V_g. The design of $R4$ is similar to $R1$ but with 30 turns instead of 40, a higher $Q = 150$, and a lower $f_0 = 341.5$ MHz. For $R4$ $L = 750$ nH, implying a larger capacitance of 0.3 pF.

A charge transition on the quantum dot occured at $V_g = 758.75$ mV, causing an increase in the total capacitance of the resonant circuit by an amount δC that created a dispersive shift of the resonant frequency from $f_0 = 341.75$ to $f_0' = 341.25$. Averaged slices of V_{RF} when the quantum dot was biased on and off of the charge transition point are shown

in green and black, respectively, in Fig. D.3(b). The capacitance associated with charging the quantum dot may be calculated from $f_0'/f_0 = \sqrt{C/(C + \delta C)}$, resulting in $\delta C = 0.9$ fF. When the charge transition is thermally broadened, as here, and the driving frequency is much smaller than the tunnel rate to the lead (not such a strong inequality in this case), Chorley *et al.* [179] found the effective capacitance to be $C_{\text{eff}} = e^2\alpha^2/4k_BT$, where α is the fraction of the total dot capacitance contributed by the lead. With a temperature of 0.1 K, this model matches our observed δC with $\alpha = 0.44$ which is reasonable based on DC transport measurements. It should noted that this quantum capacitance is (fortunately) two orders of magnitude larger than the geometrical capacitance of the dot calculated from the charging energy $E_C = e^2/C$, which gives 15 aF for a charging energy of 10 meV.

D.5 Effect of resonator capacitance on readout sensitivity

It is intuitive that a readout mechanism based on changing capacitance will be more sensitive if the total capacitance of the circuit is minimized. To illustrate this point, two resonators are compared in Fig. D.4, one a superconducting NbN spiral identical to $R1$ with $C = 0.15$ pF attached to the right lead, the other a normal Cu coil with $L = 18$ μH, $f_0 = 43$ MHz, $Q = 50$, and $C = 0.75$ pF attached to the left lead. With the nanotube device configured as a single quantum dot that was approximately equally coupled to both leads ($\alpha_R/\alpha_L \sim 1.5$), the larger capacitance resonator responded much less strongly to charge transitions in the quantum dot [Fig. D.4(c)] than did the smaller capacitance resonator [Fig. D.4(d)]. V_{RF} was scaled by the maximum peak height in both cases so that line cuts along the green lines in Fig. D.4(c) and (d) emphasize the large difference in signal-to-noise ratio in the two cases (SNR$\sim$ 5 for the Cu resonator and $\sim$ 70 for the NbN resonator). The ratio of SNRs for the two resonators is approximately equal to the ratio

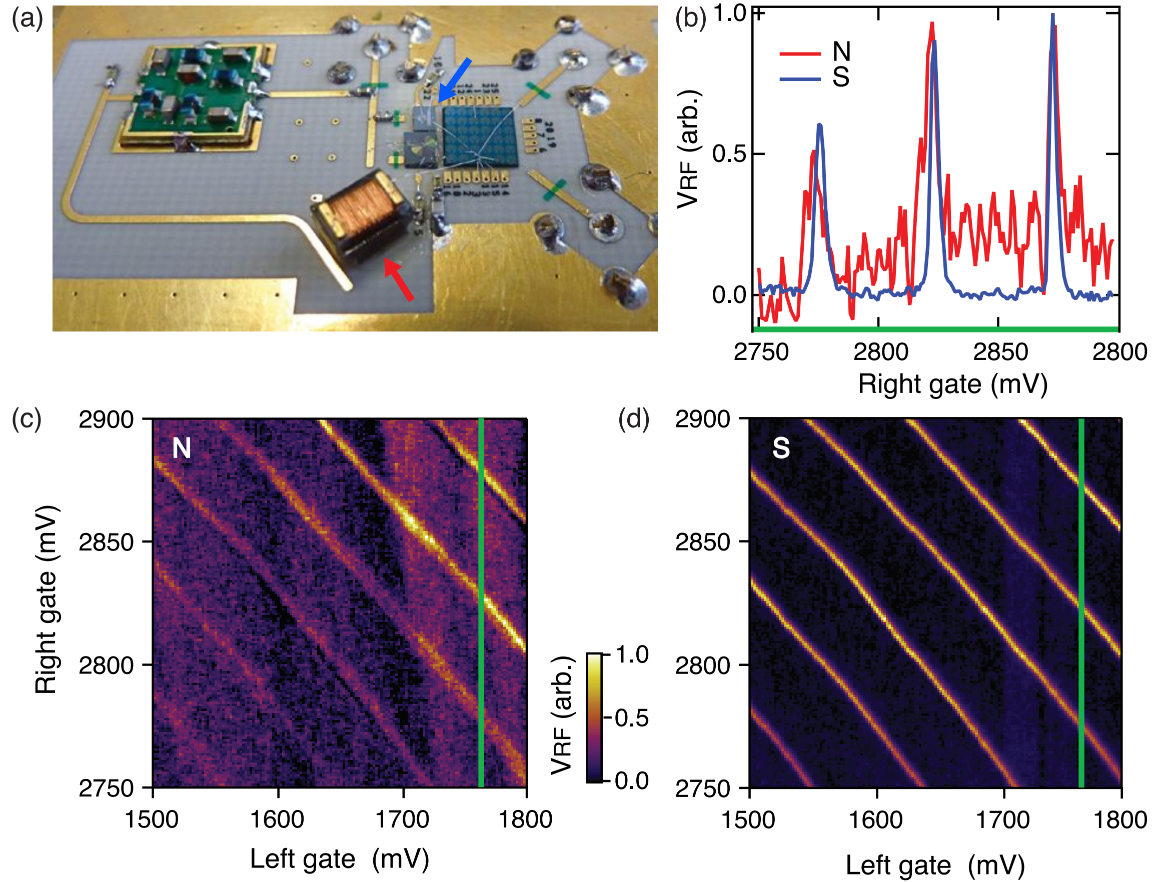

Figure D.4: (a) Board layout for comparison of a superconducting NbN resonator (indicated with a blue arrow) with a smaller capacitance, $C \sim 0.15$ pF, and a normal Cu resonator (red arrow) with a larger $C \sim 0.75$ pF. (b) Cuts showing V_{RF} as a single quantum dot is charged for a normal resonator [red trace is a cut along the green line in (c)] and a superconducting resonator [blue trace, cut from (d)]. The peaks heights have been normalized to the same value to emphasize the difference in SNR. (c) and (d) V_{RF} as a function of the left and right gate voltages [outermost gates in Fig. D.2(a)] showing diagonal lines characteristic of single dot charging.

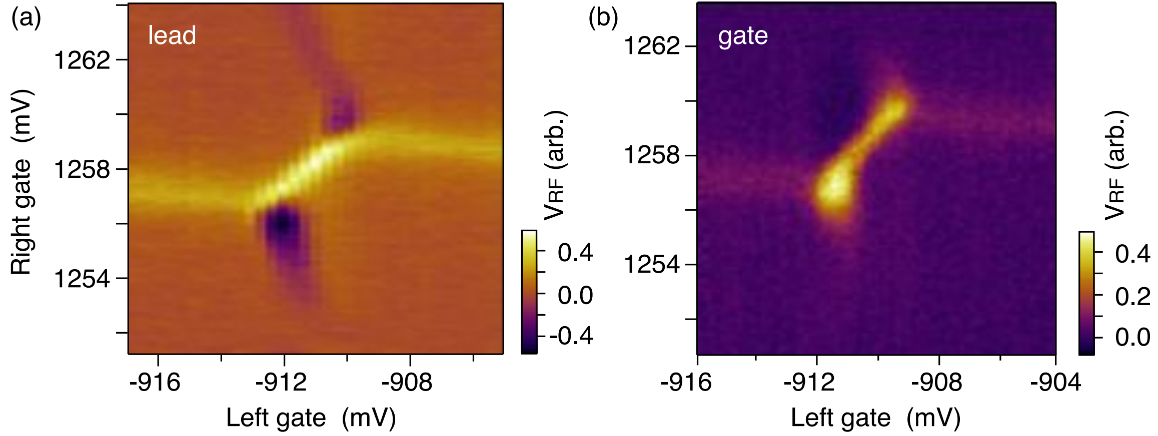

Figure D.5: Comparison of readout signal using a resonator attached to a lead (a) and to a gate (b). The resonators are $R4$ [Fig. D.3(a)] and $R2$ [Fig. D.2(b)].

of their capacitances, taking into account the $\sim 50\%$ stronger coupling to the right lead to which the NbN resonator was attached.

D.6 Effect of resonator–dot coupling on readout sensitivity

The sensitivity of this dispersive readout technique also depends strongly on the coupling of the resonator to the dot through the coupling factor α since $C_{\text{eff}} \propto \alpha^2$ [179]. To demonstrate this effect, readout using $R4$ (left lead) and $R2$ (center gate) is compared in Fig. D.5. In both cases, the honeycomb charging pattern characteristic of a double quantum dot is visible in V_{RF} [127]. The integration time per pixel for $R4$ [Fig. D.5(a)] was 30 ms yielding a SNR of 25 for the interdot charge transition, and the integration time for $R2$ [Fig. D.5(b)] was 50 ms for a SNR of 15. Adjusting for the different integration times, the SNR of $R4$ would be approximately twice that of $R2$. However, sensitivity is proportional to quality factor which was $\sim$ 7 times larger for $R2$ (1000) relative to $R4$ (150). If the resonators had the same Q, the SNR for $R4$ would be 14 times larger than for $R1$, which is approximately equal to $1/\alpha^2$, where $\alpha = 0.25$ is the coupling relative to the leads of the

center gate to the double dot detuning axis.

It should be noted that for the interdot charge transitions of interest for spin qubit applications, one might expect one of the gates to either side of the center gate to be more sensitive to charge transfer from one dot to the other. The wide outermost gates would be ideal for this purpose except that they were used for pulsed manipulation of the dots and were not available for resonator attachment (the pulses would excite the resonators), and the plunger gates were found to be too narrow to have strong coupling. In practice, the asymmetry between dots that is normally present in real devices is sufficient to provide dipole coupling for the center gate that exceeds that of the plunger gates. A better solution would be to have an additional wide gate on one side as in §C.4 and Ref. [177].

D.7 Measurement of phase and amplitude response

A significant improvement in signal quality is obtained by measuring both quadratures (phase and amplitude) of the resonator response. Following advice from Vlad Manucharyan, I implemented such a measurement by adding a second signal generator producing a LO signal shifted in frequency (typically 25 MHz) from the first. Both LO signals were split and mixed together to produce two IF signals, one for the circuit that went to the sample and one reference signal that did not include the sample. Taking advantage of Jim Medford's expert coding skills, both IF signals were compared with numerical oscillators in an AlazarTech ATS9350 digitizer card (2 channels, 500 MSa/s, 12-bit) to determine a stable phase and amplitude measurement.

A schematic including all components of the circuit used to measure a single resonator with this method is shown in Fig. D.6. The LO output power was attenuated sufficiently that the excitation did not broaden the Coulomb transitions. This power is res-

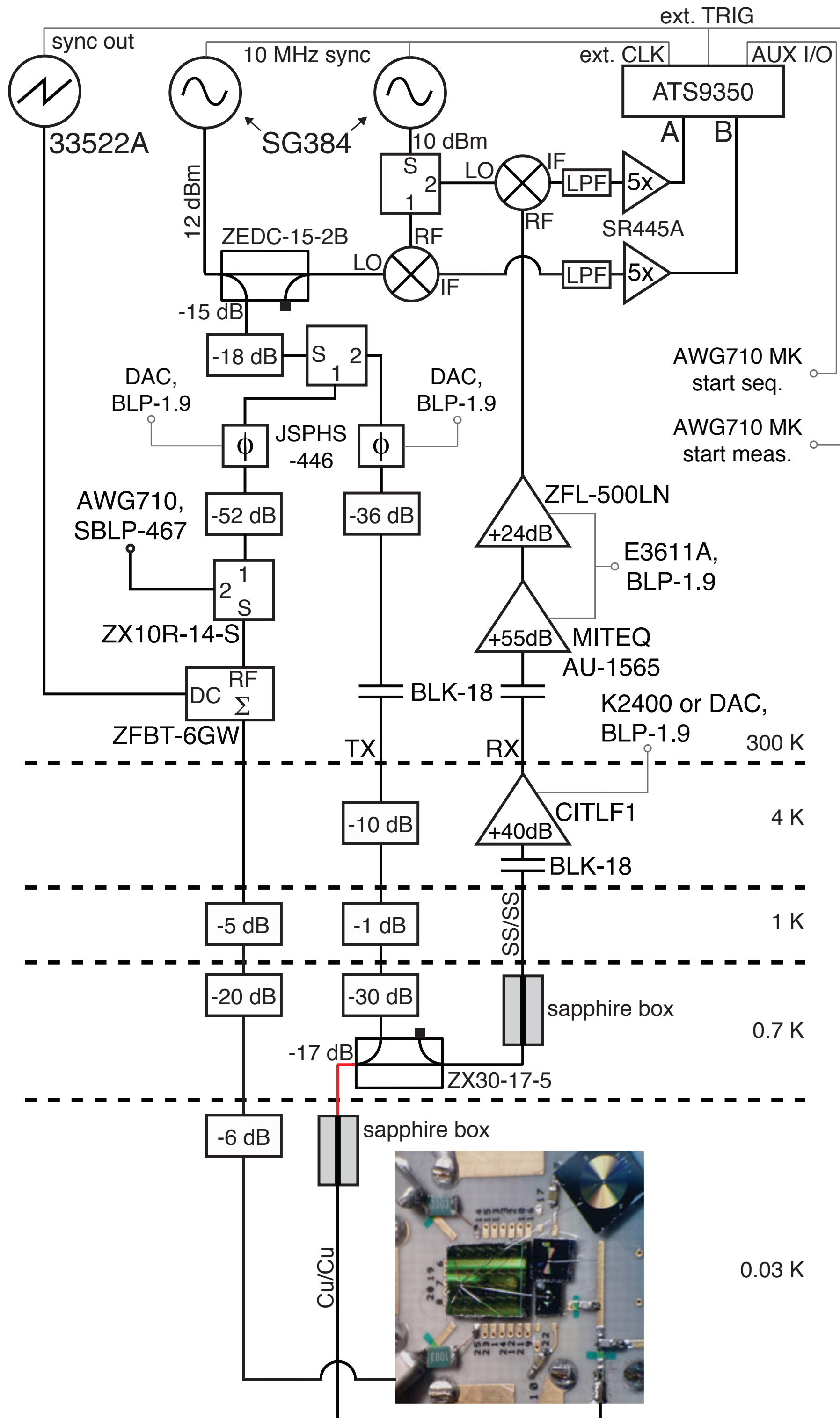

Figure D.6: Heterodyne detection circuit for phase and amplitude measurement. Most parts Mini-Circuits. Mixers are ZP-3MH, unmarked splitters are ZESC-2-11. Red coax segment is Coax Co. Ag-plated SS inner/SS outer. Attenuators are Midwest Microwave ATT-0298-XX-HEX-02 or XMA 2082-6418-XX (XX = dB). LPF before SR445A is BLP-X, depends on IF.

onator dependent because the voltage experienced by the sample is enhanced by the quality factor of the resonator. For $R4$ ($Q = 150$) the LO power was +12 dBm, which for the 130 dB of attenuation (including splitters and couplers but *not* accounting for losses in cables and components) shown in Fig. D.6 resulted in a power of -118 dBm at the resonator.

In addition to the two sources (SRS SG384) and digitizer, a gate voltage was ramped using an Agilent 33522A[5] to allow rapid charge scans. The frequency was limited either by room temperature bias tees, if present, or by the bandwidth of the resonator. No pulsed-gate experiments are described in this chapter but the ways an arbitrary waveform generator (Tektronix AWG710 in this case) was incorporated into the circuit—output to pulse gates and marker channels to trigger acquisition—are shown for their educational value. One novel aspect of this circuit was that the RF excitation sent to the sample is split with one path going to the resonators and the other path going to one of the gates controlling the quantum dot. It was found that a significant signal enhancement could be gained by shaking the gate with the strongest capacitive coupling to the dot at the frequency of the resonator but out of phase. The signal reaching the gate had a power of -110 dBm.

There were two sapphire boxes and a DC block (Mini-Circuits BLK-18) on the readout line between the cryoamp and the sample. With only one sapphire box anchored to the still, the electron temperature rose significantly (100 to 200 mK, probably) when the amp was turned on. Adding the second sapphire box at the mixing chamber and a DC block at 4 K (both at the same time, unfortunately), no effect of the amp was observed.

Example phase and amplitude signals for a double quantum dot at zero bias are shown in Fig. D.7. Both signals were largest along the lines corresponding to loading of the right dot from the right lead, as expected since the resonator being read out ($R4$) was attached to the right lead. The amplitude response was strongest near the triple points

[5] This two-channel box is convenient for creating diagonal ramps of two gates simultaneously.

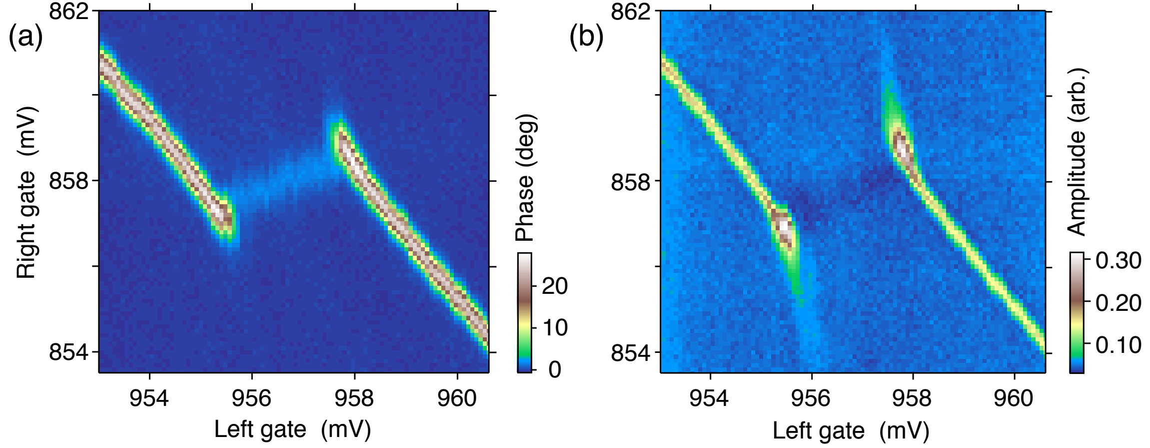

Figure D.7: (a) Phase and (b) amplitude readout of double dot charge states, using the 340 MHz resonance shown in Fig. D.3 and heterodyne detected with $IF = 25$ MHz,

where a non-zero conductance would be measured. The phase shift for lead transitions was about 25 degrees, and the weaker interdot signal was about 2 degrees. This interdot phase shift is comparable to that achieved by Frey *et al.* when the factor of 15 difference in Q is taken into account [177]; in other words, the ratio of dispersive shift to resonant frequency $\Delta f/f_0 = 0.1\%$ was the same as reported here. However, the resonator design of Ref. [177] has the benefit of a 20 times larger resonant frequency so that a correspondingly larger Q can be used without sacrificing bandwidth.

Figure D.7 was obtained with an integration time of 0.2 seconds/pixel to achieve a SNR of 250 for the lead transition and 20 for the interdot transition, corresponding to integration times for unity SNR of 3 μs for the lead transition and 0.5 ms for the interdot transition. It is therefore clear that adapting this technique for single-shot readout of spin qubits will require a design that responds more strongly to the interdot transition than to the lead transitions.

D.8 Dispersive readout of spin blockade

This technique could be used for readout of spin qubits by monitoring the interdot charge transition in a spin blockade configuration, as in Ref. [169]. A step in that direction is shown in Fig. D.8 where DC transport measurements of a spin-blockaded few-electron double quantum dot are compared with amplitude readout of the low-frequency resonator $R3$ (attached to the left lead in this case). The DC current measurements [Fig. D.8(a) and (b)] demonstrate the current rectification characteristic of spin blockade [135], as well as thermally assisted tunneling near the edges of the finite bias triangles in the blocked direction [139].

The amplitude response of the resonator shows the locations in gate voltage where electrons were transferred from the left dot to the left lead, with a much weaker signal for transitions to the right lead. In the unblocked bias direction [Fig. D.8(d)], the amplitude signal was strong within the finite bias triangle, and also revealed the presence of two levels within the bias window (separated by about 300 μeV) that are more difficult to discern in the DC current measurement. In the blocked direction, the amplitude signal is suppressed except near the tips of the triangles, consistent with the DC current data and the blocked flow of current in that direction. Pulsed gate measurements in this and other spin blockaded configurations showed no time-dependent signal due to spin relaxation, likely because of a prohibitively short lifetime near zero interdot detuning where this dispersive readout scheme is sensitive.

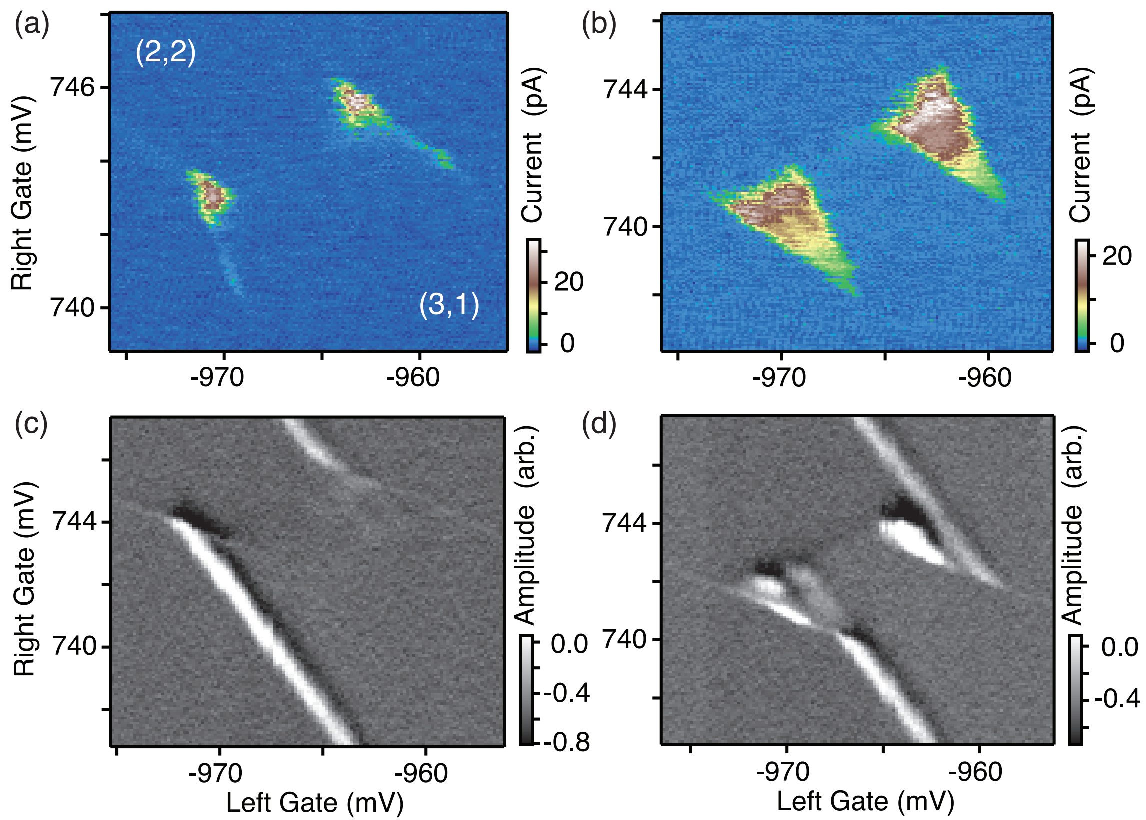

Figure D.8: (a) and (b) DC current measured with a source-drain bias of +1 and −1 mV, respectively, at the (3,1) to (2,2) charge transition. (c) and (d) Amplitude reflectometry measurements under the same conditions as (a) and (b).

Bibliography

[1] N. A. Gershenfeld and I. L. Chuang, *Bulk spin resonance quantum computing*, Science **275**, 350 (1997).

[2] D. G. Cory, A. F. Fahmy, and T. F. Havel, *Ensemble quantum computing by NMR spectroscopy*, Proc. Natl. Acad. Sci. USA **94**, 1634 (1997).

[3] D. Loss and D. P. DiVincenzon, *Quantum computation with quantum dots*, Phys. Rev. A **57**, 120 (1998).

[4] R. Hanson, L. P. Kouwenhoven, J. R. Petta, S. Tarucha, and L. M. K. Vandersypen, *Spins in few-electron quantum dots*, Rev. Mod. Phys. **79**, 1217 (2007).

[5] A. C. Johnson, J. R. Petta, J. M. Taylor, A. Yacoby, M. D. Lukin, C. M. Marcus, M. P. Hanson, and A. C. Gossard, *Triplet-singlet spin relaxation via nuclei in a double quantum dot*, Nature **435**, 925 (2005).

[6] J. R. Petta, A. C. Johnson, J. M. Taylor, E. A. Laird, A. Yacoby, C. M. Marcus, M. P. Hanson, and A. C. Gossard, *Coherent manipulation of coupled electron spins in semiconductor quantum dots*, Science **309**, 2180 (2005).

[7] David R. Lide, ed., *Handbook of Chemistry and Phyiscs*, 78th Ed. (CRC Press, 1997).

[8] J. P. Gordon and K. D. Bowers, *Microwave spin echoes from donor electrons in silicon*, Phys. Rev. Lett. **1**, 368 (1958).

[9] W. K. Liu, K. M. Whitaker, A. L. Smith, K. R. Kittilstved, B. H. Robinson, and D. R. Gamelin, *Room-temperature electron spin dynamics in free-standing ZnO quantum dots*, Phys. Rev. Lett. **98**, 186804 (2007).

[10] G. Balasubramanian, P. Neumann, D. Twitchen, M. Markham, R. Kolesov, N. Mizuochi, J. Isoya, J. Achard, J. Beck, J. Tissler, V. Jacques, P. R. Hemmer, F. Jelezko, and J. Wrachtrup, *Ultralong spin coherence time in isotopically engineered diamond*, Nature Materials **8**, 383 (2009).

[11] A. M. Tyryshkin, S. Tojo, J. J. L. Morton, H. Riemann, N. V. Abrosimov, P. Becker, H.-J. Pohl, T. Schenkel, M. L. W. Thewalt, K. M. Itoh, and S. A. Lyon, *Electron spin coherence exceeding seconds in high-purity silicon*, Nature Materials **11**, 143 (2012).

[12] *Few electron double quantum dot in an isotopically purified ^{28}Si quantum well*, Applied Physics Letters **100**, 143110 (2012).

[13] S. Nadj-Perge, S. Frolov, E. P. A. M. Bakkers, and L. P. Kouwenhoven, *Spin-orbit qubit in a semiconductor nanowire*, Nature **468**, 1084 (2010).

[14] C. Kloeffel, M. Trif, and D. Loss, *Strong spin-orbit interaction and helical hole states in Ge/Si nanowires*, Phys. Rev. B **84**, 195314 (2011).

[15] J. M. Taylor, C. M. Marcus, and M. D. Lukin, *Long-lived memory for mesoscopic quantum bits*, Phys. Rev. Lett. **90**, 206803 (2003).

[16] M. V. G. Dutt, C. M. Marcus, and M. D. Lukin, *Quantum register based on individual electronic and nuclear spin qubits in diamond*, Science **316**, 1312 (2007).

[17] J. J. L. Morton, A. M. Tyryshkin, R. M. Brown, S. Shankar, B. W. Lovett, A. Ardavan, T. Schenkel, E. E. Haller, J. W. Ager, and S. A. Lyon, *Solid-state quantum memory using the ^{31}P nuclear spin*, Nature **455**, 1085 (2008).

[18] D. R. McCamey, J. V. Tol, G. W. Morley, and C. Boehme, *Electronic spin storage in an electrically readable nuclear spin memory with a lifetime >100 seconds*, Science **330**, 1652 (2010).

[19] S. Foletti, H. Bluhm, D. Mahalu, V. Umansky, and A. Yacoby, *Universal quantum control of two-electron spin quantum bits using dynamic nuclear polarization*, Nature Physics **5**, 903 (2009).

[20] N. Mason, M. J. Biercuk, and C. M. Marcus, *Local gate control of a carbon nanotube double quantum dot*, Science **303**, 655 (2004).

[21] M. J. Biercuk, S. Garaj, N. Mason, J. M. Chow, and C. M. Marcus, *Gate-defined quantum dots on carbon nanotubes*, Nano Lett. **5**, 1267 (2005).

[22] S. Sapmaz, C. Meyer, P. Beliczynski, P. Jarillo-Herrero, and L. P. Kouwenhoven, *Excited state spectroscopy in carbon nanotube double quantum dots*, Nano Lett. **6**, 1350 (2006).

[23] M. R. Gräber, W. A. Coish, C. Hoffmann, M. Weiss, J. Furer, S. Oberholzer, D. Loss, and C. Schönenberger, *Molecular states in carbon nanotube double quantum dots*, Phys. Rev. B **74**, 075427 (2006).

[24] H. I. Jørgensen, K. Grove-Rasmussen, J. R. Hauptmann, and P. E. Lindelof, *Single wall carbon nanotube double quantum dot*, Applied Physics Letters **89**, 232113 (2006).

[25] H. I. Jørgensen, K. Grove-Rasmussen, K.-Y. Wang, A. M. Blackburn, K. Flensberg, P. E. Lindelof, and D. A. Williams, *Singlet-triplet physics and shelling filling in carbon nanotube double quantum dots*, Nature Phys. **4**, 536 (2008).

[26] M. R. Buitelaar, J. Fransson, A. L. Cantone, C. G. Smith, D. A. ad G. A. C. Jones, A. Ardavan, A. N. Khlobystov, A. A. R. Watt, K. Porfyrakis, and G. A. D. Briggs, *Pauli spin blockade in carbon nanotube double quantum dots*, Phys. Rev. B **77**, 245349 (2008).

[27] G. A. Steele, G. Gotz, and L. P. Kouwenhoven, *Tunable few-electron double quantum dots and klein tunnelling in ultraclean carbon nanotubes*, Nature Nanotechnology **4**, 363 (2009).

[28] F. Molitor, S. Droscher, J. Güttinger, A. Jacobson, C. Stampfer, T. Ihn, and K. Ensslin, *Transport through graphene double dots*, Applied Physics Letters **94**, 222107 (2009).

[29] X. L. Liu, D. Hug, and L. M. K. Vandersypen, *Gate-defined graphene double quantum dot and excited state spectroscopy*, Nano Letters **10**, 1623 (2010).

[30] L.-J. Wang, H.-O. Li, T. Tu, G. Cao, C. Zhou, X.-J. Hao, Z. Su, M. Xiao, G.-C. Guo, A. M. Chang, , and G.-P. Guo, *Controllable tunnel coupling and molecular states in a graphene double quantum dot*, Applied Physics Letters **100**, 022106 (2012).

[31] C. Volk, S. Fringes, B. Terres, J. Dauber, S. Engels, S. Trellenkamp, and C. Stampfer, *Electronic excited states in bilayer graphene double quantum dots*, Nano Letters **11**, 3581 (2011).

[32] J. J. L. Morton, A. M. Tyryshkin, A. Ardavan, S. C. Benjamin, K. Profyrakis, S. A. Lyon, and G. A. D. Briggs, *Bang-bang control of fullerene qubits using ultrafast phase gates*, Nature Physics **2**, 40 (2006).

[33] R. M. Brown, A. M. Tyryshkin, K. Porfyrakis, E. M. Gauger, B. W. Lovett, A. Ardavan, S. A. Lyon, G. A. D. Briggs, and J. J. L. Morton, *Coherent state transfer between an electron and nuclear spin in* $^{15}NC_{60}$, Phys. Rev. Lett. **106**, 110504 (2011).

[34] P. Neumann, R. Kolesov, B. Naydenov, J. Beck, F. Rempp, M. Steiner, V. Jacques, G. Balasubramanian, M. L. Markham, D. J. Twitchen, S. Pezzagna, J. Meijer, J. Twamley, F. Jelezko, and J. Wrachtrup, *Quantum register based on coupled electron spins in a room-temperature solid*, Science **6**, 249 (2010).

[35] T. van der Sar, Z. H. Wang, M. S. Blok, H. Bernien, T. H. Taminiau, D. Toyli, D. A. Lidar, D. D. Awschalom, R. Hanson, and V. V. Dobrovitski, *Decoherence-protected quantum gates for a hybrid solid-state spin register* .

[36] C. B. Simmons, J. R. Prance, B. J. V. Bael, T. S. Koh, Z. Shi, D. E. Savage, M. G. Lagally, R. Joynt, M. Friesen, S. N. Coppersmith, and M. A. Eriksson, *Tunable spin loading and* T_1 *of a silicon spin qubit measured by single-shot readout*, Phys. Rev. Lett. **106**, 156804 (2011).

[37] A. Morello, J. J. Pla, F. A. Zwanenburg, K. W. Chan, K. Y. Tan, H. Huebl, M. Mttnen, C. D. Nugroho, C. Yang, J. A. van Donkelaar, A. D. C. Alves, D. N. Jamieson,

C. C. Escott, L. C. L. Hollenberg, R. G. Clark, and A. S. Dzurak, *Single-shot readout of an electron spin in silicon*, Nature **467**, 687 (2010).

[38] H. W. Liu, T. Fujisawa, Y. Ono, H. Inokawa, A. Fujiwara, K. Takashina, and Y. Hirayama, *Pauli-spin-blockade transport through a silicon double quantum dot*, Phys. Rev. B **77**, 073310 (2008).

[39] G. P. Lansbergen, R. Rahman, J. Verduijn, G. C. Tettamanzi, N. Collaert, S. Biesemans, G. Klimeck, L. C. L. Hollenberg, and S. Rogge, *Lifetime-enhanced transport in silicon due to spin and valley blockade*, Phys. Rev. Lett. **107**, 136602 (2011).

[40] N. S. Lai, W. H. Lim, C. H. Yang, F. A. Zwanenburg, W. A. Coish, F. Qassemi, A. Morello, and A. S. Dzurak, *Pauli spin blockade in a highly tunable silicon double quantum dot*, Scientific Reports **1**, 110 (2011).

[41] G. Yamahata, T. Kodera, H. O. H. Churchill, K. Uchida, C. M. Marcus, and S. Oda, *Magnetic field dependence of Pauli spin blockade: a window into the sources of spin relaxation in silicon quantum dots* .

[42] Y. Hu, F. Kuemmeth, C. M. Lieber, and C. M. Marcus, *Hole spin relaxation in gesi coreshell nanowire qubits*, Nature Nanotechnology **7**, 47 (2012).

[43] B. M. Maune, M. G. Borselli, B. Huang, T. D. Ladd, P. W. Deelman, K. S. Holabird, A. A. Kiselev, I. Alvarado-Rodriguez, R. S. Ross, A. E. Schmitz, M. Sokolich, C. A. Watson, M. F. Gyure, and A. T. Hunter, *Coherent singlet-triplet oscillations in a silicon-based double quantum dot*, Nature **481**, 344 (2012).

[44] W. F. Koehl, B. B. Buckley, F. J. Heremans, G. Calusine, and D. D. Awschalom, *Room temperature coherent control of defect spin qubits in silicon carbide*, Nature **479**, 84 (2011).

[45] L. Trifunovic, O. Dial, M. Trif, J. R. Wootton, R. Abebe, A. Yacoby, and D. Loss, *Long-distance spin-spin coupling via floating gates*, Physical Review X **2**, 011006 (2012).

[46] Y. Kubo, F. R. Ong, P. Bertet, D. Vion, V. Jacques, D. Zheng, A. Dréau, J.-F. Roch, A. Auffeves, F. Jelezko, J. Wrachtrup, M. F. Barthe, P. Bergonzo, and D. Esteve, *Strong coupling of a spin ensemble to a superconducting resonator*, Phys. Rev. Lett. **105**, 140502 (2010).

[47] D. I. Schuster, A. P. Sears, E. Ginossar, L. DiCarlo, L. Frunzio, J. J. L. Morton, H. Wu, G. A. D. Briggs, B. B. Buckley, D. D. Awschalom, and R. J. Schoelkopf, *High-cooperativity coupling of electron-spin ensembles to superconducting cavities*, Phys. Rev. Lett. **105**, 140501 (2010).

[48] F. Kuemmeth, H. O. H. Churchill, P. K. Herring, and C. M. Marcus, *Carbon nanotubes for coherent spintronics*, Materials Today **13**, 18 (2010).

[49] Z. H. Zhong, N. M. Gabor, J. E. Sharping, A. L. Gaeta, and P. L. McEuen, *Terahertz time-domain measurement of ballistic electron resonance in a single-walled carbon nanotube*, Nature Nanotechnology **3**, 201 (2008).

[50] R. Saito, G. Dresselhaus, and M. S. Dresselhaus, *Physical properties of carbon nanotubes* (Imperial College Press, London, 1998).

[51] J. W. Mintmire, D. H. Robertson, and C. T. White, *Properties of fullerene nanotubules*, Journal of Physics and Chemistry of Solids **54**, 1835 (1993).

[52] B. Chandra, R. Caldwell, M. Huang, L. M. Huang, M. Y. Sfeir, S. P. O'Brien, T. F. Heinz, and J. Hone, *Electrical transport measurements of nanotubes with known (n, m) indices*, Physica Status Solidi B-Basic Solid State Physics **243**, 3359 (2006).

[53] C. W. Zhou, J. Kong, and H. J. Dai, *Intrinsic electrical properties of individual single-walled carbon nanotubes with small band gaps*, Physical Review Letters **84**, 5604 (2000).

[54] A. W. Bushmaker, V. V. Deshpande, S. Hsieh, M. W. Bockrath, and S. B. Cronin, *Large modulations in the intensity of raman-scattered light from pristine carbon nanotubes*, Physical Review Letters **103**, 067401 (2009).

[55] M. Ouyang, J. L. Huang, C. L. Cheung, and C. M. Lieber, *Energy gaps in "metallic" single-walled carbon nanotubes*, Science **292**, 702 (2001).

[56] C. L. Kane and E. J. Mele, *Size shape and low energy electronic structure of carbon nanotubes*, Phys. Rev. Lett. **78**, 1932 (1997).

[57] E. D. Minot, Y. Yaish, V. Sazonova, J. Y. Park, M. Brink, and P. L. McEuen, *Tuning carbon nanotube band gaps with strain*, Physical Review Letters **90**, 156401 (2003).

[58] P. K. Valavala, D. Banyai, M. Seel, and R. Pati, *Self-consistent calculations of strain-induced band gap changes in semiconducting (n,0) carbon nanotubes*, Physical Review B **78**, 235430 (2008).

[59] V. V. Deshpande, B. Chandra, R. Caldwell, D. S. Novikov, J. Hone, and M. Bockrath, *Mott insulating state in ultraclean carbon nanotubes*, Science **323**, 106 (2009).

[60] A. Javey, J. Guo, Q. Wang, M. Lundstrom, and H. Dai, *Ballistic carbon nanotube eld-effect transistors*, Nature **424**, 654 (2003).

[61] D. H. Cobden and J. Nygård, *Shell filling in closed single-wall carbon nanotube quantum dots*, Physical Review Letters **89**, 046803 (2002).

[62] W. J. Liang, M. Bockrath, and H. Park, *Shell filling and exchange coupling in metallic single-walled carbon nanotubes*, Physical Review Letters **88**, 126801 (2002).

[63] J. Cao, Q. Wang, and H. Dai, *Electron transport in very clean, as-grown suspended carbon nanotubes*, Nature Materials **4**, 745 (2005).

[64] A. Makarovski, L. An, J. Liu, and G. Finkelstein, *Persistent orbital degeneracy in carbon nanotubes*, Physical Review B **74**, 155431 (2006).

[65] M. Bockrath, D. H. Cobden, P. L. McEuen, N. G. Chopra, A. Zettl, A. Thess, and R. E. Smalley, *Single-electron transport in ropes of carbon nanotubes*, Science **275**, 1922 (1997).

[66] S. Sapmaz, P. Jarillo-Herrero, J. Kong, C. Dekker, L. P. Kouwenhoven, and H. S. J. van der Zant, *Electronic excitation spectrum of metallic carbon nanotubes*, Phys. Rev. B **71**, 153402 (2005).

[67] A. Pályi and G. Burkard, *Hyperfine-induced valley mixing and the spin-valley blockade in carbon-based quantum dots*, Phys. Rev. B **80**, 201404(R) (2009).

[68] T. S. Jespersen, K. Grove-Rasmussen, K. Flensberg, J. Paaske, K. Muraki, T. Fujisawa, and J. Nygård, *Gate-dependent orbital magnetic moments in carbon nanotubes*, Phys. Rev. Lett. **107**, 186802 (2011).

[69] E. D. Minot, Y. Yaish, V. Sazonova, and P. L. McEuen, *Determination of electron orbital magnetic moments in carbon nanotubes*, Nature **428**, 536 (2004).

[70] F. Kuemmeth, S. Ilani, D. C. Ralph, and P. L. McEuen, *Coupling of spin and orbital motion of electrons in carbon nanotubes*, Nature **452**, 448 (2008).

[71] Y. Oreg, K. Byczuk, and B. I. Halperin, *Spin configurations of a carbon nanotube in a nonuniform external potential*, Physical Review Letters **85**, 365 (2000).

[72] T. Ando, *Spin-orbit interaction in carbon nanotubes*, J. Phys. Soc. Japan **69**, 1757 (2000).

[73] L. Chico, M. P. Lopez-Sancho, and M. C. Munoz, *Spin splitting induced by spin-orbit interaction in chiral nanotubes*, Physical Review Letters **93**, 176402 (2004).

[74] D. Huertas-Hernando, F. Guinea, and A. Brataas, *Spin-orbit coupling in curved graphene, fullerenes, nanotubes, and nanotube caps*, Physical Review B **74**, 155426 (2006).

[75] T. F. Fang, W. Zuo, and H. G. Luo, *Kondo effect in carbon nanotube quantum dots with spin-orbit coupling*, Physical Review Letters **101**, 246805 (2008).

[76] B. Dora, M. Gulacsi, J. Koltai, V. Zolyomi, J. Kurti, and F. Simon, *Electron spin resonance signal of luttinger liquids and single-wall carbon nanotubes*, Physical Review Letters **101**, 106408 (2008).

[77] W. Izumida, K. Sato, and R. Saito, *Spin-orbit interaction in single wall carbon nanotubes: Symmetry adapted tight-binding calculation and effective model analysis*, Journal of the Physical Society of Japan **78**, 074707 (2009).

[78] B. Wunsch, *Few-electron physics in a nanotube quantum dot with spin-orbit coupling*, Physical Review B **79**, 235408 (2009).

[79] A. Secchi and M. Rontani, *Coulomb versus spin-orbit interaction in few-electron carbon-nanotube quantum dots*, Physical Review B **80**, 041404 (2009).

[80] D. E. Logan and M. R. Galpin, *Tunneling transport and spectroscopy in carbon nanotube quantum dots*, Journal of Chemical Physics **130**, 224503 (2009).

[81] J. Zhou, Q. Liang, and J. Dong, *Asymmetric spin-orbit coupling in single-walled carbon nanotubes*, Physical Review B **79**, 195427 (2009).

[82] J. S. Jeong and H. W. Lee, *Curvature-enhanced spin-orbit coupling in a carbon nanotube*, Physical Review B **80**, 075409 (2009).

[83] L. Chico, M. P. Lòpez-Sancho, and M. C. Muñoz, *Curvature-induced anisotropic spin-orbit splitting in carbon nanotubes*, Phys. Rev. B **79**, 235423 (2009).

[84] D. V. Bulaev, B. Trauzettel, and D. Loss, *Spin-orbit interaction and anomalous spin relaxation in carbon nanotube quantum dots*, Phys. Rev. B **77**, 235301 (2008).

[85] C. Galland and A. Imamoglu, *All-optical manipulation of electron spins in carbon-nanotube quantum dots*, Physical Review Letters **101**, 157404 (2008).

[86] Y. M. Hu, W. L. Yang, M. Feng, and J. F. Du, *Distributed quantum-information processing with fullerene-caged electron spins in distant nanotubes*, Physical Review A **80**, 022322 (2009).

[87] H. Sun, X. L. Feng, S. Q. Gong, and C. H. Oh, *Giant cross-Kerr nonlinearity in carbon nanotube quantum dots with spin-orbit coupling*, Physical Review B **79**, 193404 (2009).

[88] S. Weiss, E. I. Rashba, F. Kuemmeth, H. O. H. Churchill, and K. Flensberg, *Spin-orbit effects in carbon nanotube double quantum dots*, Phys. Rev. B **82**, 165427 (2010).

[89] T. S. Jespersen, K. Grove-Rasmussen, J. Paaske, K. Muraki, T. Fujisawa, J. Nygård, and K. Flensberg, *Gate-dependent spin-orbit coupling in multielectron carbon nanotube*, Nature Physics **7**, 348 (2011).

[90] T. Ando and T. Nakanishi, *Impurity scattering in carbon nanotubes-absence of back scattering*, Journal of the Physical Society of Japan **67**, 1704 (1998).

[91] A. Pályi and G. Burkard, *Spin-valley blockade in carbon nanotube double quantum dots*, Phys. Rev. B **84**, 155424 (2010).

[92] R. Saito, A. Grüneis, G. G. Samsonidze, V. W. Brar, G. Dresselhaus, M. S. Dresselhaus, A. Jorio, L. G. Cançado, C. Fantini, M. A. Pimenta, and A. G. S. Filho, *Double resonance raman spectroscopy of single-wall carbon nanotubes*, New Journal of Physics **5**, 157 (2003).

[93] K. Flensberg and C. M. Marcus, *Bends in nanotubes allow electric spin control and coupling*, Phys. Rev. B **81**, 195418 (2010).

[94] H. O. H. Churchill, F. Kuemmeth, J. W. Harlow, A. J. Bestwick, E. I. Rashba, K. Flensberg, C. H. Stwertka, T. Taychatanapat, S. K. Watson, and C. M. Marcus, *Relaxation and dephasing in a two-electron* $^{1}3C$ *nanotube double quantum dot*, Physical Review Letters **102**, 166802 (2009).

[95] M. S. Rudner and E. I. Rashba, *Spin relaxation due to deflection coupling in nanotube quantum dots*, Phys. Rev. B **81**, 125426 (2010).

[96] H. O. H. Churchill, A. J. Bestwick, J. W. Harlow, F. Kuemmeth, D. Marcos, C. H. Stwertka, S. K. Watson, and C. M. Marcus, *Electron-nuclear interaction in* ^{13}C *nanotube double quantum dots*, Nature Phys. **5**, 321 (2009).

[97] C. H. Pennington and V. A. Stenger, *Nuclear magnetic resonance of* c_{60} *and fulleride superconductors*, Rev. Mod. Phys. **68**, 855 (1996).

[98] O. V. Yazyev, *Hyperfine interactions in graphene and related carbon nanostructures*, Nano Lett. **8**, 1011 (2008).

[99] J. Fischer, B. Trauzettel, and D. Loss, *Hyperfine interaction and electron-spin decoherence in graphene and carbon nanotube quantum dots*, Physical Review B (Condensed Matter and Materials Physics) **80**, 155401 (2009).

[100] S. Latil, L. Henrard, C. Goze Bac, P. Bernier, and A. Rubio, ^{13}C *NMR chemical shift of single-wall carbon nanotubes*, Phys. Rev. Lett. **86**, 3160 (2001).

[101] B. Braunecker, P. Simon, and D. Loss, *Nuclear magnetism and electronic order in* ^{13}C *nanotubes*, Phys. Rev. Lett. **102**, 116403 (2009).

[102] B. Braunecker, P. Simon, and D. Loss, *Nuclear magnetism and electron order in interacting one-dimensional conductors*, Phys. Rev. B **80**, 165119 (2009).

[103] D. B. Farmer and R. G. Gordon, *Atomic layer deposition on suspended single-walled carbon nanotubes via gas-phase noncovalent functionalization*, Nano Lett. **6**, 699 (2006).

[104] J. von Stecher, B. Wunsch, M. Lukin, E. Demler, and A. M. Rey, *Double quantum dots in carbon nanotubes*, Phys. Rev. B **82**, 125437 (2010).

[105] D. C. Harris, *Symmetry and Spectroscopy: An Introduction to Vibrational and Electronic Spectroscopy* (Dover, 1989).

[106] A. A. Reynoso and K. Flensberg, *Dephasing and hyperfine interaction in carbon nanotubes double quantum dots: The disordered case* .

[107] A. A. Reynoso and K. Flensberg, *Dephasing and hyperfine interaction in carbon nanotube double quantum dots: The clean limit*, Phys. Rev. B **84**, 205449 (2011).

[108] Y. Hu, H. O. H. Churchill, D. J. Reilly, J. Xiang, C. M. Marcus, and C. M. Lieber, *A Ge/Si heterostructure nanowire-based double quantum dot with integrated charge sensor*, Nature Nanotechnology **2**, 622 (2007).

[109] R. Hanson, L. P. Kouwenhoven, J. R. Petta, S. Tarucha, and L. M. K. Vandersypen, *Spins in few-electron quantum dots*, Rev. Mod. Phys. **79**, 1217 (2007).

[110] F. H. L. Koppens, C. Buizert, K. J. Tielrooij, I. T. Vink, K. C. Nowack, T. Meunier, L. P. Kouwenhoven, and L. M. K. Vandersypen, *Driven coherent oscillations of a single electron spin in a quantum dot*, Nature **442**, 766 (2006).

[111] G. Burkard, D. Loss, and D. P. DiVincenzon, *Coupled quantum dots as quantum gates*, Phys. Rev. B **59**, 2070 (1999).

[112] A. V. Khaetskii, D. Loss, and L. Glazman, *Electron spin decoherence in quantum dots due to interaction with nuclei*, Phys. Rev. Lett. **88**, 186802 (2002).

[113] W. Lu, J. Xiang, B. P. Timko, Y. Wu, and C. M. Lieber, *One-dimensional hole gas in germanium/silicon nanowire heterostructures*, PNAS **102**, 10046 (2005).

[114] C. Fasth, A. Fuhrer, M. T. Björk, and L. Samuelson, *Tunable double quantum dot in inas nanowires defined by local gate electrodes*, Nano Lett. **5**, 1487 (2005).

[115] A. Pfund, I. Shorubalko, K. Ensslin, and R. Leturcq, *Suppression of spin relaxation in an inas nanowire double quantum dot*, Phys. Rev. Lett. **99**, 036801 (2007).

[116] C. Fasth, A. Fuhrer, V. N. Golovach, and D. Loss, *Direct measurement of the spin-orbit interaction in a two-electron inas nanowire quantum dot*, Phys. Rev. Lett. **98**, 266801 (2007).

[117] A. M. Tyrshkin, S. A. Lyon, T. Schenkel, J. Bokor, J. Chu, W. Jantsch, F. Schäffler, J. L. Truitt, S. N. Coppersmith, and M. A. Eriksson, *Electron spin coherence in Si*, Physica E **35**, 257 (2006).

[118] B. E. Kane, *A silicon-based nuclear spin quantum computer*, Nature **393**, 133 (1998).

[119] R. Vrijen, E. Yablonovitch, K. Wang, H. W. Jiang, A. Balandin, V. Roychowdhury, T. Mor, and D. DiVincenzo, *Electron-spin-resonance transistors for quantum computing in silicon-germanium heterostructures*, Phys. Rev. A **62**, 012306 (2000).

[120] M. Friesen, P. Rugheimer, D. E. Savage, M. G. Lagally, D. W. van der Weide, R. Joynt, and M. A. Eriksson, *Practical design and simulation of silicon-based quantum-dot qubits*, Phys. Rev. B **67**, 121301(R) (2003).

[121] B. Trauzettel, D. V. Bulaev, and D. Loss, *Spin qubits in graphene quantum dots*, Nature Phys. **192**, 192 (2007).

[122] V. C. Chan, T. M. Buehler, A. J. Ferguson, D. R. McCamey, D. J. Reilly, A. S. Dzurak, R. G. Clark, C. Yang, and D. N. Jamieson, *Ion implanted Si:P double dot with gate tunable interdot coupling*, Journal of Applied Physics **100**, 106104 (2006).

[123] Z. Zhong, Y. Fang, W. Lu, and C. M. Lieber, *Coherent single charge transport in molecular-scale silicon nanowires*, Nano Lett. **5**, 1143 (2005).

[124] L. J. Klein, D. E. Savage, and M. A. Eriksson, *Coulomb blockade and kondo effect in a few-electron silicon/silicon-germanium quantum dot*, Appl. Phys. Lett. **90**, 033103 (2007).

[125] T. Berer, D. Pachinger, G. Pillwein, M. Muhlberger, H. Lichtenberger, G. Brunthaler, and F. Schäfer, *Lateral quantum dots in Si/SiGe realized by a schottky split-gate technique*, Appl. Phys. Lett. **88**, 162112 (2006).

[126] M. R. Sakr, H. W. Jiang, E. Yablonovitch, and E. T. Croke, *Fabrication and characterization of electrostatic Si/SiGe quantum dots with an integrated read-out channel*, Appl. Phys. Lett. **87**, 223104 (2005).

[127] W. G. van der Wiel, S. D. Franceschi, J. M. Elzerman, T. Fujisawa, S. Tarucha, and L. P. Kouwenhoven, *Electron transport through double quantum dots*, Rev. Mod. Phys. **75**, 1 (2003).

[128] J. M. Elzerman, J. S. Greidanus, L. H. W. van Beveren, S. D. Franceschi, L. M. K. Vandersypen, S. Tarucha, and L. P. Kouwenhoven, *Few-electron quantum dot circuit with integrated charge read out*, Phys. Rev. B **67**, 16108(R) (2003).

[129] M. J. Biercuk, D. J. Reilly, T. M. Buehler, V. C. Chan, J. M. Chow, R. G. Clark, and C. M. Marcus, *Charge sensing in carbon-nanotube quantum dots on microsecond timescales*, Phys. Rev. B **73**, 201402(R) (2006).

[130] L. DiCarlo, H. J. Lynch, A. C. Johnson, L. I. Childress, K. Crockett, C. M. Marcus, M. P. Hanson, and A. C. Gossard, *Differential charge sensing and charge delocalization in a tunable double quantum dot*, Phys. Rev. Lett. **92**, 226801 (2004).

[131] D. V. Bulaev and D. Loss, *Spin relaxation and decoherence of holes in quantum dots*, Phys. Rev. Lett. **95**, 076805 (2005).

[132] D. Heiss, S. Schaeck, H. Huebl, M. Bichler, G. Abstreiter, J. J. Finley, D. V. Bulaev, and D. Loss, *Observation of extremely slow hole spin relaxation in self-assembled quantum dots*, Phys. Rev. B **76**, 241306(R) (2007).

[133] F. Schäffler, *High-mobility Si and Ge structures*, Semicond. Sci. Technol. **12**, 1515 (1997).

[134] R. Hanson, V. V. Dobrovitski, A. E. Feiguin, O. Gwyat, and D. D. Awschalom, *Coherent dynamics of a single spin interating with an adjustable spin bath*, Science **320**, 352 (2008).

[135] K. Ono, D. G. Austing, Y. Tokura, and S. Tarucha, *Current rectification by Pauli exclusion in a weakly coupled double quantum dot system*, Science **297**, 1313 (2002).

[136] I. A. Merkulov, A. L. Efros, and M. Rosen, *Electron spin relaxation by nuclei in semiconductor quantum dots*, Phys. Rev. B **65**, 205309 (2002).

[137] W. A. Coish, J. Fischer, and D. Loss, *Exponential decay in a spin bath*, Phys. Rev. B **77**, 125329 (2008).

[138] L. Liu and S. Fan, *Isotope labeling of carbon nanotubes and formation of ^{12}C and ^{13}C nanotube junctions*, J. Am. Chem. Soc. **123**, 11502 (2001).

[139] A. C. Johnson, J. R. Petta, C. M. Marcus, M. P. Hanson, and A. C. Gossard, *Singlet-triplet spin blockade and charge sensing in a few-electron double quantum dot*, Phys. Rev. B **72**, 165308 (2005).

[140] F. H. L. Koppens, J. A. Folk, J. M. Elzerman, R. Hanson, L. H. W. van Beveren, I. T. Vink, H. P. Tranitz, W. Wegscheider, L. P. Kouwenhoven, and L. M. K. Vandersypen, *Control and detection of singlet-triplet mixing in a random nuclear field*, Science **309**, 1346 (2005).

[141] O. N. Jouravlev and Y. V. Nazarov, *Electron transport in a double quantum dot governed by a nuclear magnetic field*, Phys. Rev. Lett. **96**, 176804 (2006).

[142] A. Pfund, I. Shorubalko, K. Ensslin, and R. Leturcq, *Suppression of spin relaxation in an InAs nanowire double quantum dot*, Phys. Rev. Lett. **99**, 036801 (2007).

[143] J. Baugh, Y. Kitamura, K. Ono, and S. Tarucha, *Large nuclear Overhauser fields detected in vertically coupled double quantum dots*, Phys. Rev. Lett. **99**, 096804 (2007).

[144] D. J. Reilly, J. M. Taylor, J. R. Petta, C. M. Marcus, M. P. Hanson, and A. C. Gossard, *Exchange control of nuclear spin diffusion in a double quantum dot*, Phys. Rev. Lett. **104**, 236802 (2010).

[145] M. S. Rudner and L. S. Levitov, *Self-polarization and dynamical cooling of nuclear spins in double quantum dots*, Phys. Rev. Lett. **99**, 036602 (2007).

[146] W. A. Coish and F. Qassemi, *Leakage-current line shapes from inelastic cotunneling in the pauli spin blockade regime*, Phys. Rev. B **84**, 245407 (2011).

[147] A. Kiss, A. Pályi, Y. Ihara, P. Wzietek, P. Simon, H. Alloul, V. Zólyomi, J. Koltai, J. Kürti, B. Dóra, and F. Simon, *Enhanced NMR relaxation of Tomonaga-Luttinger liquids and the magnitude of the carbon hyperfine coupling in single-wall carbon nanotubes*, Phys. Rev. Lett. **107**, 187204 (2011).

[148] F. H. L. Koppens, K. C. Nowack, and L. M. K. Vandersypen, *Spin echo of a single electron spin in a quantum dot*, Phys. Rev. Lett. **100**, 236802 (2008).

[149] D. J. Reilly, J. M. Taylor, J. R. Petta, C. M. Marcus, M. P. Hanson, and A. C. Gossard, *Suppressing spin qubit dephasing by nuclear state preparation*, Science **321**, 817 (2008).

[150] N. Shaji, C. B. Simmons, M. Thalakulam, L. J. Klein, H. Qin, H. Luo, D. E. Savage, M. G. Lagally, A. J. Rimberg, R. Joynt, M. Friesen, R. H. Blick, S. N. Coppersmith, and M. A. Eriksson, *Spin blockade and lifetime-enhanced transport in a few-electron Si/SiGe double quantum dot*, Nature Phys. **4**, 540 (2008).

[151] J. R. Williams, L. DiCarlo, and C. M. Marcus, *Quantum hall effect in a gate-controlled p-n junction of graphene*, Science **317**, 638 (2007).

[152] P. Jarillo-Herrero, J. Kong, H. S. J. van der Zant, C. Dekker, L. P. Kouwenhoven, and S. D. Franceschi, *Orbital Kondo effect in carbon nanotubes*, Nature **434**, 484 (2005).

[153] A. V. Khaetskii and Y. V. Nazarov, *Spin-flip transitions between Zeeman sublevels in semiconductor quantum dots*, Phys. Rev. B **64**, 125316 (2001).

[154] S. Amasha, K. MacLean, I. P. Radu, D. M. Zumbühl, M. A. Kastner, M. P. Hanson, and A. C. Gossard, *Electrical control of spin relaxation in a quantum dot*, Phys. Rev. Lett. **100**, 046803 (2008).

[155] J. M. Taylor, J. R. Petta, A. C. Johnson, A. Yacoby, , C. M. Marcus, and M. D. Lukin, *Relaxation, dephasing, and quantum control of electron spins in double quantum dots*, Phys. Rev. B **76**, 035315 (2007).

[156] D. J. Reilly, J. M. Taylor, E. A. Laird, J. R. Petta, C. M. Marcus, M. P. Hanson, and A. C. Gossard, *Measurement of temporal correlations of the overhauser field in a double quantum dot*, Phys. Rev. Lett. **101**, 236803 (2008).

[157] Y. Hu, F. Kuemmeth, C. M. Lieber, and C. M. Marcus, *Hole spin relaxation in Ge-Si core-shell nanowire qubits*, Nat Nano **7**, 47 (2012).

[158] J. Xiang, W. Lu, Y. Hu, Y. Wu, H. Yan, and C. M. Lieber, *Ge/Si nanowire heterostructures as high-performance field-effect transistors*, Nature **441**, 489 (2006).

[159] X.-J. Hao, T. Tu, G. Cao, C. Zhou, H.-O. Li, G.-C. Guo, W. Y. Fung, Z. Ji, G.-P. Guo, and W. Lu, *Strong and tunable spin-orbit coupling of one-dimensional holes in Ge/Si core/shell nanowires*, Nano Letters **10**, 2956 (2010).

[160] G. L. James C. Phillips, *Bonds and Bands in Semiconductors*, 2nd Ed. (Momentum Press, 2009).

[161] J. Kong, H. T. Soh, A. M. Cassell, C. F. Quate, and H. J. Dai, *Synthesis of individual single-walled carbon nanotubes on patterned silicon wafers*, Nature **395**, 878 (—1998—), 133XT Times Cited:772 Cited References Count:21.

[162] B. Cord, J. Lutkenhaus, and K. K. Berggren, *Optimal temperature for development of poly(methylmethacrylate)*, Journal of Vacuum Science and Technology B **25**, 2013 (2007).

[163] Y.-C. Yeo, P. Ranade, T.-J. King, and C. Hu, *Effects of high-κ gate dielectric materials on metal and silicon gate workfunctions*, Electron Device Letters, IEEE **23**, 342 (2002).

[164] D. K. Brown, *Deep ultraviolet photolithography capability of ZEP520A electron beam resist for mix and match lithography*, Journal of Vacuum Science and Technology B **25**, 2447 (2007).

[165] K. Williams, K. Gupta, and M. Wasilik, *Etch rates for micromachining processing–Part II*, Microelectromechanical Systems, Journal of **12**, 761 (2003).

[166] Z. Zhang, X. Liang, S. Wang, K. Yao, Y. Hu, Y. Zhu, Q. Chen, W. Zhou, Y. Li, Y. Yao, J. Zhang, and L.-M. Peng, *Doping-free fabrication of carbon nanotube based ballistic CMOS devices and circuits*, Nano Letters **7**, 3603 (2007).

[167] W.-S. Jeon, S. Yang, C. soo Lee, and S.-W. Kang, *Atomic layer deposition of Al_2O_3 thin films using trimethylaluminum and isopropyl alcohol*, Journal of the Electrochemical Society **149**, C306 (2002).

[168] N. P. Kobayashi and R. S. Williams, *Two-stage atomic layer deposition of aluminum oxide on alkanethiolate self-assembled monolayers using n-propanol and water as oxygen sources*, Chemistry of Materials **20**, 5356 (2008).

[169] K. D. Petersson, C. G. Smith, D. Anderson, P. Atkinson, G. A. C. Jones, and D. A. Ritchie, *Charge and spin state readout of a double quantum dot coupled to a resonator*, Nano Letters **10**, 2789 (2010).

[170] E. A. Laird, C. Barthel, E. I. Rashba, C. M. Marcus, M. P. Hanson, and A. C. Gossard, *Hyperfine-mediated gate-driven electron spin resonance*, Phys. Rev. Lett. **99**, 246601 (2007).

[171] J. Yang, E. Dauler, A. Ferri, A. Pearlman, A. Verevkin, G. Gol'tsman, B. Voronov, R. Sobolewski, W. Keicher, and K. Berggren, *Fabrication development for nanowire GHz-counting-rate single-photon detectors*, Applied Superconductivity, IEEE Transactions on **15**, 626 (2005).

[172] M. Hatzakis, B. J. Canavello, and J. M. Shaw, *Single-step optical lift-off process*, IBM J. Res. Develop. **24**, 452 (1980).

[173] A. J. Annunziata, D. F. Santavicca, L. Frunzio, G. Catelani, M. J. Rooks, A. Frydman, and D. E. Prober, *Tunable superconducting nanoinductors*, Nanotechnology **21**, 445202 (2010).

[174] S. Weinreb, J. Bardin, H. Mani, and G. Jones, *Matched wideband low-noise amplifiers for radio astronomy*, Review of Scientific Instruments **80**, 044702 (2009).

[175] D. M. Pozar, *Microwave Engineering*, 3rd Ed. (Wiley, 2005).

[176] A. Wallraff, D. I. Schuster, A. Blais, L. Frunzio, R. S. Huang, J. Majer, S. Kumar, S. M. Girvin, and R. J. Schoelkopf, *Strong coupling of a single photon to a superconducting qubit using circuit quantum electrodynamics*, Nature **431**, 162 (2004).

[177] T. Frey, P. J. Leek, M. Beck, A. Blais, T. Ihn, K. Ensslin, and A. Wallraff, *Dipole coupling of a double quantum dot to a microwave resonator*, Phys. Rev. Lett. **108**, 046807 (2012).

[178] M. R. Delbecq, V. Schmitt, F. D. Parmentier, N. Roch, J. J. Viennot, G. Fève, B. Huard, C. Mora, A. Cottet, and T. Kontos, *Coupling a quantum dot, fermionic leads, and a microwave cavity on a chip*, Phys. Rev. Lett. **107**, 256804 (2011).

[179] S. J. Chorley, J. Wabnig, Z. V. Penfold-Fitch, K. D. Petersson, J. Frake, C. G. Smith, and M. R. Buitelaar, *Measuring the complex admittance of a carbon nanotube double quantum dot*, Phys. Rev. Lett. **108**, 036802 (2012).

[180] S. Mohan, M. del Mar Hershenson, S. Boyd, and T. Lee, *Simple accurate expressions for planar spiral inductances*, Solid-State Circuits, IEEE Journal of **34**, 1419 (1999).

[181] H. A. Wheeler, *Transmission-line properties of parallel strips separated by a dielectric sheet*, IEEE Trans. Microwave Theory Tech. **MTT-13**, 172 (1965).

[182] D. J. Reilly, C. M. Marcus, M. P. Hanson, and A. C. Gossard, *Fast single-charge sensing with a RF quantum point contact*, Applied Physics Letters **91**, 162101 (2007).